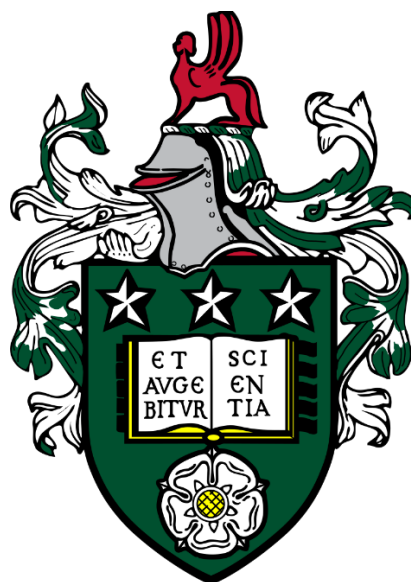


Dissolution and Pyrolysis Kinetics of Natural and Mercerized Cotton



Yunhao Liang

Submitted in accordance with the requirements for the degree of
Doctor of Philosophy

The University of Leeds
School of Physics and Astronomy

August, 2022

The candidate confirms that the work submitted is his own, except where work which has formed part of jointly-authored publications has been included. The contribution of the candidate and the other authors to this work has been explicitly indicated below. The candidate confirms that appropriate credit has been given within the thesis where reference has been made to the work of others.

This copy has been supplied on the understanding that it is copyright material and that no quotation from the thesis may be published without proper acknowledgement.

The right of Yunhao Liang to be identified as Author of this work has been asserted by him in accordance with the Copyright, Designs and Patents Act 1988.

© 2022 The University of Leeds and Yunhao Liang

Acknowledgements

All the work carried out in this thesis was undertaken at the University of Leeds and supervised by Prof. Michael Ries and Dr. Peter Hine. Therefore, I would like to thank them for their never-ending stream of ideas and persistent pursuit of science, and their generous and constant advice.

I would like to take this opportunity to also thank all the other wonderful people that made the completion of my PhD studies. This thesis would not have been finished without the help and support of:

All my lovely colleagues in the Soft Matter Physics Group.

Of them, I would like to take special thanks to Dr. James Hawkins for every moment that we were having discussions about our research projects, from which abundant interesting ideas and points are initiated like water trickling. Dr. Dan Baker, who has been providing endless support with my experimental work and always doing me a favour anytime I was in trouble with equipment. My other colleagues who used to be in office 9.64c and Aubergine room, EC Stoner, and those in 1.30, 1.12 and 1.35 of Bragg Building.

My friends and family in China and the UK, especially, Shunchao Su who provides chances for me to explore a new field, business; and Min Fu and Xin Zhang (Starry) who always support me in terms of life and research.

Prof. Antje Potthast, University of Natural Resources and Life Science for conducting decomposition measurement and Dr. Adrian Cunliffe and Karine Alves Thorne, CAPE Analytical Facilities Organisation, University of Leeds for providing the TGA measurements.

All the other people I have met in the past of my life, because of you, I have been 'I'.

Last but not least, I would like to thank my parents, Aijun Wang and Qiwei Liang, in particular, who provide both the funding and spiritual support for my PhD study in the UK.

Author's Publications

Paper I: Liang, Y., Hawkins, J.E., Ries, M.E. and Hine, P.J., 2021. Dissolution of cotton by 1-ethyl-3-methylimidazolium acetate studied with time-temperature superposition for three different fibre arrangements. *Cellulose*, 28(2), pp.715-727. <https://doi.org/10.1007/s10570-020-03576-x>

Author contributions: Yunhao Liang: Conceptualization, Methodology, Investigation, Writing - Original Draft, Visualization. James E. Hawkins: Conceptualization, Investigation, Writing - Review & Editing, data analysis and discussion. Michael E. Ries: Supervision, Conceptualization, Writing - Review & Editing, Project administration. Peter J. Hine: Supervision, Conceptualization, Writing - Review & Editing, Project administration.

Paper II: Hawkins, J.E., Liang, Y., Ries, M.E. and Hine, P.J., 2021. Time temperature superposition of the dissolution of cellulose fibres by the ionic liquid 1-ethyl-3-methylimidazolium acetate with cosolvent dimethyl sulfoxide. *Carbohydrate Polymer Technologies and Applications*, 2, p.100021. <https://doi.org/10.1016/j.carpta.2020.100021>

Author contributions: James E. Hawkins: Conceptualization, Methodology, Investigation, Writing - Original Draft, Visualization. Yunhao Liang: Conceptualization, Investigation, Writing - Review & Editing, Data Analysis and Discussion. Michael E. Ries: Supervision, Conceptualization, Writing - Review & Editing, Project administration. Peter J. Hine: Supervision, Conceptualization, Writing - Review & Editing, Project administration.

Paper III: Liang, Y., Ries, M. E., & Hine, P. J., 2022. Three methods to measure the dissolution activation energy of cellulosic fibres using time-

temperature superposition. *Carbohydrate Polymers*, 291, 119541.
<https://doi.org/10.1016/j.carbpol.2022.119541>

Author contributions: Yunhao Liang: Conceptualization, Methodology, Investigation, Writing - Original Draft, Visualization. Michael E. Ries: Supervision, Conceptualization, Writing - Review & Editing, Project administration. Peter J. Hine: Supervision, Conceptualization, Writing - Review & Editing, Project administration.

Paper IV: Liang, Y., Ries, M. E., & Hine, P. J., 2022. Pyrolysis Activation Energy of Cellulosic Fibres Investigated by a Method Derived from The First Order Global Model. submitted to *Carbohydrate Polymers*, under review.

Author contributions: Yunhao Liang: Conceptualization, Methodology, Investigation, Writing - Original Draft, Visualization. Michael E. Ries: Supervision, Conceptualization, Writing - Review & Editing, Project administration. Peter J. Hine: Supervision, Conceptualization, Writing - Review & Editing, Project administration

Abstract

The dissolution and pyrolysis behaviours of cellulose -based materials, cotton yarns, and how to utilize the findings to instruct the fabrication of all cellulose composites (ACCs) with cotton textiles has been explored. The dissolution kinetics of two cotton yarns, a natural cotton yarn and a mercerized cotton yarn, in the ionic liquid, 1-ethyl-3-methylimidazolium acetate ([C2mim][OAc]) is studied as a function of processing time and temperature, where water is chosen to coagulate the dissolved cellulose. Wide angle X-ray diffraction (WAXD) and optical microscopy (OM) are chosen to analyse the resultant samples in association with quantifying the coagulated cellulose. The results show a time-temperature equivalence, and that the dissolution behaviour follows an Arrhenius behaviour, resulting in the calculation of dissolution activation energies (E_a). For the natural cotton yarn, the dissolution activation energy is found to be independent of the fibre arrangement, giving an average dissolution E_a of 96 ± 3 kJ/mol, and for the mercerized cotton yarn, the dissolution was quantified with four methods, and an independence of quantifying methods is seen on the activation energy, giving an average value of 74 ± 2 kJ/mol. Thermogravimetric analysis (TGA) is implemented on the two cotton yarns under different heating speeds and a modified first order global model is found to adequately describe the pyrolysis behaviour, leading to the pyrolysis activation energy of 153 ± 2 kJ/mol and 188 ± 9 kJ/mol for the natural and mercerized cotton yarns, respectively. The reason for the difference in the dissolution behaviour is hypothesized to be the carbohydrate composition and/or the molecular weight, while for that in the pyrolysis behaviour, the carbohydrate composition and/or crystalline structure dominate. All cellulose composites are finally made out of a fabric woven from

the mercerized cotton yarn, possessing a relatively low dissolution E_a and high thermal stability, with [C2mim][OAc] as the solvent. A potentially continuous ACCs fabricating process is then proposed. The findings will be of interest to researchers fabricating ACCs and those studying the dissolution and pyrolysis kinetics of cellulose-based materials.

Table of Contents

Acknowledgements.....	iii
Author's Publications	v
Abstract.....	vii
List of Tables	xii
List of Figures	xv
List of Abbreviations and Symbols	xxvii
Chapter 1 Introduction and literature review	1
1.1 Introduction	1
1.1.1 Project aims and objectives.....	3
1.1.2 Thesis outline	4
1.2 Literature review.....	6
1.2.1 Cellulose	6
1.2.2 Ionic liquids	18
1.2.3 The development of ACCs processed by ionic liquids	25
1.2.4 Summary.....	31
Chapter 2 Experimental	33
2.1 Materials.....	33
2.2 Characterization	33
2.2.1 Optical microscopy.....	33
2.2.2 Wide-angle X-ray diffraction	34
Chapter 3 The dissolution of natural cotton cellulose in [C2mim][OAc].....	38
3.1 Introduction	38
3.2 Methods	39
3.2.1 The procedure of dissolving the natural cotton samples with [C2mim][OAc]	39
3.2.2 Optical microscopy.....	41
3.2.3 Wide-angle X-ray diffraction	42
3.3 Results and discussion.....	43
3.3.1 Micromorphology of cotton single yarns and cotton bundles	43
3.3.2 Analysis of dissolution of cotton single yarn in [C2mim][OAc] with TTS.....	45
3.3.3 Crystalline structure of cotton arrays and cotton bundles	49

3.3.4 Dissolution of cotton arrays and cotton bundles analysed with TTS	51
3.3.5 Analysis of the effect of sample arrangement on the dissolution behaviour	55
3.4 Conclusions.....	58
Chapter 4 Dissolution of mercerized cotton cellulose in [C2mim][OAc]	60
4.1 Introduction	60
4.2 Methods	63
4.2.1 The procedure of dissolving the mercerized cotton yarns with [C2mim][OAc]	63
4.2.2 Optical microscopy	65
4.2.3 Wide-angle X-ray diffraction	66
4.2.4 Quantification of dissolution	66
4.2.5 Water volume fraction and swelling ratio.....	69
4.3 Results and discussion.....	71
4.3.1 Micromorphology.....	73
4.3.2 Analysis of mercerized cotton array crystalline structure....	75
4.3.3 Understanding the dissolution of mercerized cotton in [C2mim][OAc] via TTS analysis.....	76
4.3.4 Regional water volume fraction and swelling ratio of mercerized cotton yarn hydrogels	85
4.4 Conclusions.....	90
Chapter 5 Comparative analysis of cellulose from the natural and mercerized cotton in chemical composition, molecular weight, thermal stability and dissolution kinetics	92
5.1 Introduction	92
5.2 Methods	96
5.2.1 Optical microscopy	96
5.2.2 Wide-angle X-ray Diffraction	97
5.2.3 Determination of weight-average molecular weight and molecular weight distribution	97
5.2.4 Determination of the content of lignin and hemicellulose ...	97
5.2.5 Thermogravimetric analysis	98
5.2.6 Theoretical considerations and calculation procedures for the pyrolysis analysis	98
5.3 Results and discussion.....	100
5.3.1 Morphology of the two cotton yarns	100

5.3.2 Comparison between the natural cotton yarn and the mercerized cotton yarn in terms of carbohydrate composition and molecular weight	102
5.3.3 Thermal stability comparison of the natural cotton yarns and the mercerized cotton yarns via TGA	106
5.3.4 Determination of the pyrolysis activation energy	109
5.4 Conclusions.....	122
Chapter 6 Fabrication of all cellulose composites from the mercerized cotton	124
6.1 Introduction	124
6.2 Methods	125
6.2.1 Preparation of all cellulose composites from fabrics woven from the mercerized cotton yarn	125
6.2.2 Optical microscopy.....	129
6.2.3 Tensile test and peel test	129
6.3 Results and discussion.....	131
6.3.1 Determination of the conditions for dissolving the MCYF samples.....	131
6.3.2 Microscopy results.....	134
6.3.3 Mechanical properties	137
6.3.4 Comparison between a patented batch method and a proposed continuous process	142
6.4 Conclusions.....	145
Chapter 7 Conclusion and prospective.....	147
7.1 Outcomes and conclusions	147
7.2 Prospective and future plans.....	151
References.....	152

List of Tables

Table 1.1 Carbohydrate composition of plant cellulose materials. Credit: Sundarraaj et al. [20]	7
Table 1.2 Elastic moduli of different cellulose allomorphs found from literature, where only those considering intramolecular hydrogen bonding are tabulated	11
Table 1.3 Summary of mechanical properties of ACCs made by one-step and two-step methods with ionic liquids.....	30
Table 3.1 Shift factors of different temperatures, obtained from the TTS analysis on cotton single yarns, used to plot Figure 3.5(e)	47
Table 3.2 Shift factors of different temperatures, obtained from the TTS analysis on cotton arrays and cotton bundles, used to plot Figure 3.7(d) and Figure 3.8(d) respectively	54
Table 4.1 Shift factors of different temperatures, obtained from the TTS analysis on dried mercerized cotton yarns, used to plot Figure 4.9(d)	78
Table 4.2 Shift factors of different temperatures, obtained from the TTS analysis on dried mercerized cotton arrays, used to plot Figure 4.10(d)	80
Table 4.3 Shift factors of different temperatures, obtained from the TTS analysis on mercerized cotton yarn hydrogels, used to plot Figure 4.11(d) and Figure 4.12(d).....	84

Table 4.4 Comparison among the four quantifying methods and the activation energies from them.....	85
Table 4.5 Comparative summary of different samples/regions in water volume fraction and shiring ratio	87
Table 4.6 Theoretical radii of MCYH-raw and DMCY-raw obtained from the extrapolating method and those in brackets measured directly from microscope pictures	90
Table 5.1 Comparison of the natural cotton yarn and the mercerized cotton yarn in carbohydrate composition, including lignin and hemicellulose	103
Table 5.2 Results of molecular weight analysis on the raw natural cotton yarn and the raw mercerized cotton yarn samples	103
Table 5.3 Statistical results of instantaneous heating rate for the NY-raw and the MCY-raw at different target heating rates set for TGA measurements	111
Table 5.4 Activation energy for the pyrolysis of NY-raw and MCY-raw calculated from the results in Figure 5.9	119
Table 6.1 Nomenclature of ACC and the corresponding processing conditions.....	129
Table 6.2 Comparison results of ACCs processing conditions between current research method and a batch method	143

Table 7.1 Summary of the dissolution and pyrolysis properties of the natural cotton and mercerized cotton in this thesis, with their carbohydrate composition and molecular weight..... 148

List of Figures

Figure 1.1 Molecular structures of (a) cellulose and (b) starch.....	9
Figure 1.2 Cellulose crystal allomorphs and conversions between each other. Image taken from the paper by Ottesen [34]	11
Figure 1.3 (a) XRD 2D patterns of different cellulose fibre polymorphs and (b) their equatorial XRD profiles. Cellulose I and cellulose II are discussed in this thesis. Credit: Nishino et al. [17].....	12
Figure 1.4 Industry process of dissolving cellulose with NMMO to generate Lyocell fibres. Image taken from the paper of Rosenau et al. [50].....	15
Figure 1.5 Comparison of the two important approaches, (a) viscose and (b) Lyocell process. Credit: Isik et al. [51]	15
Figure 1.6 Schematic mechanism of the dissolution of cellulose with the LiCl/DMAc mixture. Credit: Zhang et al. [53].....	16
Figure 1.7 Dissolving mechanism of cellulose in ionic liquids. Image adapted from the work of Zhang et al. [46]	24
Figure 1.8 Wood fibres in [C4mim]Cl/DMSO observed by optical microscopy and (A) unswollen fibre, (B) balloon, (C) membrane and (D) unswollen section between two balloons. Image taken from the paper of Cuissinat et al [131], without any scale bar originally provided.....	25

Figure 1.9 Schematic illustration of fabricating approaches for all-cellulose composites: one-step and two-step approaches.....	26
Figure 2.1 WAXD spectrum deconvolution curves of (a) the raw natural cotton sample and (b) the raw mercerized cotton sample with relevant peaks labelled, where the open dots are the raw data and the solid grey lines are summation of all deconvolution peaks, CI and CII represent cellulose I and cellulose II respectively.....	36
Figure 2.2 (a) Photograph of fibres from a linen sample and (b) its two-dimensional WAXD pattern, where cellulose I crystal peaks are labelled with Miller index. Taken from the paper by De et al. [165].....	36
Figure 3.1 Three cotton sample arrangements studied in this chapter.....	39
Figure 3.2 Process of dissolving cotton single yarns and arrays in [C2mim][OAc]	41
Figure 3.3 Polished epoxy resin, containing fibers ready to be photographed (Left) and a cross sectional image of a cotton single yarn (Right) with a scale bar indicating 200 microns. The fibre schematic highlights the areas of coagulated cellulose (Red) and the undissolved core (Blue)	42

Figure 3.4 Optical microscope pictures of cotton single yarns (CY) from (a) to (g) and cotton bundles (CB) from (h) to (o) processed at different temperatures for different times with scale bars indicating 200 microns. Image (o) is a magnification of the area enclosed within the red circle in (l), in which the arrows point to the coagulated area 44

Figure 3.5 Coagulation fraction dependence of time for cotton single fibres (CY) on (a) linear time scale and (b) natural-logarithmic time scale; the time-temperature superposition plot after being shifted to 40 °C on both (c) natural-logarithmic time scale and (d) linear time scale; (e) Arrhenius plot with $\chi^2 > 0.99$. Some of the error bars are smaller than the symbols, and the dash lines in (a)-(d) provide guide for eye, and that in (e) is a fitting line..... 46

Figure 3.6 XRD spectra of cotton arrays (CA) processed at (a) 30 °C, (b) 40 °C and (c) 50 °C, and (d) cotton bundles (CB) processed at 50 °C for different times. The peaks appearing at around 20.2° and 21.8° are attributed to the cellulose II crystalline structure..... 50

Figure 3.7 (a) Coagulation fraction as a function of dissolution time and temperature for cotton arrays (CA), the time-temperature superposition after being shifted to 40 °C on both natural-logarithmic time scale (b) and linear time scale (c); Arrhenius plot (d) with $\chi^2 > 0.99$. Some error bars are smaller than the symbols, and the dash lines in (a)-(c) provide guide for eye, and that in (d) is a fitting line..... 52

Figure 3.8 (a) Coagulation fraction as a function of dissolution time and temperature for cotton bundles (CB), the time-temperature superposition after being shifted to 40 °C on both natural-logarithmic time scale (b) and linear time scale (c); Arrhenius plot (d) with $\chi^2 > 0.97$. Some error bars are smaller than the symbols, and the dash lines in (a)-(c) provide guide for eye, and that in (d) is a fitting line..... 53

Figure 3.9 Comparison of activation energies for cotton single fibers, arrays and bundles. the dot-dashed line indicates position of the average value and the rectangular shape indicates the error margin. For the array, the error bar is smaller than the size of symbol used..... 56

Figure 3.10 Comparison of time-temperature superposition after being shifted to 40 °C among cotton single yarns (CY), cotton arrays (CA) and cotton bundles (CB). The dash lines provide guide for eye, and some error bars are smaller than the symbols 57

Figure 4.1 XRD spectra of natural cotton (C0) and mercerized cotton, where C10, C15 and C20 represent the concentrations, 10 wt%, 15 wt% and 20 wt%, of sodium hydroxide solution used for mercerization, respectively. Reported by Yue et al. [187].....	61
Figure 4.2 SEM images of (a) natural cotton fibres and mercerized cotton treated with 15 wt% sodium hydroxide solution at room temperature for (b) 10, (c) 40, (d) 60 min with a zoom-in picture showing the cross-section at the top-right corner at each picture. Credit: Yu et al. [190]	62
Figure 4.3 Apparatus for dissolving mercerized cotton yarns and arrays	64
Figure 4.4 Schematic graph of hydrogels/swollen samples soaking in a water bath for optical-microscopic observation of their transverse view	66
Figure 4.5 Optical microscopy images of (a) the transverse view of a mercerized cotton yarn hydrogel soaking in a water bath and (b) the cross section of the dried mercerized cotton yarn, in which the undissolved section, the total sample and the outer ring are indicated in orange (b_H and b_D), green (a_H and a_D) and red (T_H and T_D) double-arrow lines, respectively	68

Figure 4.6 Schematic graph explaining the measurements and qualification of the dissolution process, connecting parameters with techniques and samples, where for the mercerized cotton yarn hydrogel (MCYH) CF_{OM-H} and T_H mean its coagulation fraction and ring thickness from optical microscopy, respectively; and for the dried samples (dried mercerized cotton yarn (DMCY) and arrays) CF_{OM} and CF_{XRD} represent the coagulation fractions calculated from the results of optical microscopy and wide-angle X-ray diffraction, respectively 72

Figure 4.7 Optical-microscopic transverse-view images of (a) the raw mercerized cotton yarn after soaking in water for 24 hours and (b)-(f) the mercerized cotton yarn hydrogels (MCYH); cross-section images of (g) the raw mercerized cotton yarn and (h)-(l) the dried mercerized cotton yarn (DMCY), and look to section 4.2.1 for nomenclature in detail..... 73

Figure 4.8 WAXD spectra of dried mercerized cotton arrays (DMCA) processed at (a) 30 °C and (b) 50 °C for different times, which are shifted vertically for clarity, look to section 4.2.1 for nomenclature in detail..... 75

Figure 4.9 (a) Dependence of coagulation fraction, calculated from optical microscopy results of DMCY, on time; the time-temperature superposition plot after being shifted to 40 °C on both (b) natural-logarithmic time scale and (c) linear time scale; (d) Arrhenius plot with $\chi^2 > 0.99$. Some error bars are smaller than the symbols, and the dash lines in (a)-(c) provide guide for eye, and that in (d) is a fitting line 77

Figure 4.10 (a) Dependence of coagulation fraction (CF_{XRD}), calculated from WAXD results of DMCA, on time; the time-temperature superposition plot after being shifted to 40 °C on both (b) natural-logarithmic time scale and (c) linear time scale; (d) Arrhenius plot with $\chi^2 > 0.97$. Some error bars are smaller than the symbols, and the dash lines in (a)-(c) provide guide for eye, and that in (d) is a fitting line 79

Figure 4.11 (a) Dependence of coagulation fraction (CF_{OM-H}), calculated from WAXD results of MCYH, on time; the time-temperature superposition plot after being shifted to 40 °C on both (b) natural-logarithmic time scale and (c) linear time scale; (d) Arrhenius plot with $\chi^2 > 0.99$. Some error bars are smaller than the symbols, and the dash lines in (a)-(c) provide guide for eye, and that in (d) is a fitting line 81

Figure 4.12 (a) Dependence of ring thickness (T_H), calculated from WAXD results of MCYH, on time; the time-temperature superposition plot after being shifted to 40 °C on both (b) natural-logarithmic time scale and (c) linear time scale; (d) Arrhenius plot with $\chi^2 > 0.99$. Some error bars are smaller than the symbols, and the dash lines in (a)-(c) provide guide for eye, and that in (d) is a fitting line 82

Figure 4.13 Water volume fraction of (a) outer ring and (b) central core of MCYH, and swelling ratio of (c) outer ring and (d) central core in MCYH, where the dash lines measure their average values and some error bars are smaller than the symbols 86

Figure 4.14 Radius of central core dependence on the ring thickness in (a) dried mercerized cotton yarn (DMCY) samples and (b) mercerized cotton yarn hydrogel (MCYH) samples, where the dash lines are linear fitting lines and some error bars are smaller than the symbols 89

Figure 5.1 Cross-section images of the raw natural cotton yarn (NY-raw) in (a) low magnification and (b) high magnification; the raw mercerized cotton yarn (MCY-raw) in (c) low magnification and (d) high magnification 101

Figure 5.2 Molecular weight distribution of the mercerized cotton and the natural cotton 104

Figure 5.3 Plot of dependence of dissolution activation energy ($E_{a,s}$) of cellulose samples on viscosity-average molecular weight (M_η) reported by Qi et al. [222]	105
Figure 5.4 Thermogravimetric analysis curves at different heating speeds for (a) the raw natural cotton yarn (NY-raw) and the raw mercerized cotton yarn (MCY-raw); and derivative thermogravimetric (DTG) curves at different temperature ramping rates for (c) NY-raw and (d) MCY-raw	106
Figure 5.5 Dependence of the temperature at the maximum decomposition rate (T_m) on the heating rate of TGA on both raw natural cotton yarn (NY-raw) and raw mercerized cotton yarn (MCY-raw) where the datasets are fitted with an exponential approach equation (Equation 5.16) shown with the black solid lines with $\chi^2 > 0.99$	108
Figure 5.6 Dependence of the TGA instantaneous heating rate (β') on temperature for (a) the nature cotton yarn (CY) and (b) the mercerized cotton yarn (MCY), where the legends represent target heating rates set on the TGA machine	110
Figure 5.7 Discrepancy analysis of the approximations from the origin based on the first order global method (Equation 5.10, Equation 5.11 and Equation 5.12), with the computing parameters of E , T_m and R to be 200 kJ/mol, 619 K (346 °C) and 8.314 J/(K.mol), respectively.....	113

Figure 5.8 Plots of $\ln(\ln(1/y))$ as a function of $\ln(T)$ within the temperature ranges of (a) $\pm 10\%$, (b) $\pm 5\%$, (c) $\pm 3\%$ and (d) $\pm 1\%$ of the temperature of the maximum decomposition speed (T_m), based on Equation 5.13; $\ln(\ln(1/y))$ as a function of T within the temperature ranges of (e) $\pm 10\%$, (f) $\pm 5\%$, (g) $\pm 3\%$ and (h) $\pm 1\%$ of the T_m , based on Equation 5.14; $\ln(\ln(1/y))$ as a function of T within the temperature ranges of (i) $\pm 10\%$, (j) $\pm 5\%$, (k) $\pm 3\%$ and (l) $\pm 1\%$ of the T_m , based on Equation 5.15, and all the data are for the natural cotton yarn measured with the target heating rate of $50\text{ }^\circ\text{C/min}$ 115

Figure 5.9 Pyrolysis activation energy dependence on temperature range applied for the integration, where (a)-(d) are for the natural cotton yarn(NY-raw) measured at the target heating rate of 5, 10, 20 and $50\text{ }^\circ\text{C/min}$ respectively, and (e)-(h) are for the mercerized cotton yarn (MCY-raw) measured at different target heating rates of 5, 10, 20 and $50\text{ }^\circ\text{C/min}$, respectively. The dot lines are quadratic fitting results with $\chi^2 > 0.99$ 118

Figure 5.10 Plot of average intrinsic pyrolysis activation energy ($\overline{[E]_{\beta_t}}$) vs. target heating rate (β_t) for the natural cotton yarn (NY-raw) and the mercerized cotton yarn (MCY-raw), where the dash lines show the locations of the mean values ($\overline{[E]}_{NY-raw}$ and $\overline{[E]}_{MCY-raw}$), where some error bars are smaller than the symbols 120

Figure 6.1(a) Schematic graph of the basket weave with a coordinate shown at the right bottom and (b) photograph of the basket MCY-woven fabric applied for the fabrication of all cellulose composites in this chapter, where the warp and weft are in line with y axis and x axis, respectively 126

Figure 6.2 Fabrication procedure of two-layer all cellulose composites out of mercerized cotton yarn-woven fabrics (MCYF) 128

Figure 6.3 Schematic images illustrating the amount of cellulose needed to be dissolved to make enough matrix in ACCs, which is denoted by the shaded area in two ideal scenarios of alignment between two cotton fabrics: (a) the maximum and (b) the minimum, where the matrix volume fractions are represented by the shaded areas in the rectangular and triangular areas, and they are labelled to be r_{max}^{shaded} and r_{min}^{shaded} , respectively 132

Figure 6.4 Appearance of Uni-0.2(1)-2(1) (a) when it was soaking in the water bath upon coagulation and (b) it was dried, with the flash cellulose indicated by the blue arrows 134

Figure 6.5 Cross-section images of (a) (e) single layer of the raw MCYF, (b) and (f) show Uni-1(1), (c) and (g) Uni-0.2(1)-2(1) and (d) and (h) Uni-4(1), where in (a)-(d) the axis of wefts, denoted by x, is perpendicular to the plane of cross section, while in (e)-(h) the axis of warps, represented by y, is perpendicular to the plane of cross section; and visible defects/air gaps are shown with red ellipses in (b). Recall Table 6.1 for nomenclature 135

Figure 6.6 Mechanical properties of ACCs, including (a) tensile strength, (b) Young's modulus and (c) peel strength, see Table 6.1 for nomenclature	138
Figure 6.7 Peel test curves of load as a function of extension of ACCs, where the average load is denoted with the red dash line and recall Table 6.1 for nomenclature	139
Figure 6.8 Stress-strain curves of different ACCs from tensile test along the weft direction.....	139
Figure 6.9 Schematic flow chart of the proposed continuous manufacturing process, where the feeding section, dissolving section, pressing section, coagulating section and forming/drying section are in blue, yellow, red, green and orange, respectively; the circles, red-shaded area and blue-shaded area denote rollers, solvent, e.g. ionic liquids, and coagulant, e.g. water, respectively.....	144

List of Abbreviations and Symbols

ACCs: all cellulose composites

ACC: all cellulose composite

[C2mim][OAc]: 1-ethyl-3-methylimidazolium acetate

WAXD: wide angle X-ray diffraction

XRD: X-ray diffraction

OM: optical microscopy

TGA: thermogravimetric analysis

DP: degree of polymerization

DMSO: dimethyl sulfoxide

NMMO: N-methylmorpholine-N-oxide monohydrate

LiCl/DMAc: lithium chloride/N,N-Dimethylacetamide

NaOH: Sodium hydroxide

ILs: ionic liquids

DMF: N,N-dimethylformamide

[C4mim]Cl: 1-N-butyl-3-methylimidazolium chloride

Si-69: (3-triethoxysilylpropyl) tetrasulfide

MCC: microcrystalline cellulose

MFC: microfibrillated cellulose

CNF: cellulose nanofibers

[Hemim]Cl: 1-(2-hydroxyethyl)3-methyl imidazolium chloride

[C4mim][OAc]: 1-butyl-3-methylimidazolium acetate

TTS: time-temperature superposition

CF: coagulated fraction

CY-x-y, CB-x-y and CA-x-y: a single cotton yarn, a cotton bundle and a cotton array processed at temperature 'x' (°C) for 'y' (hours), respectively

CY: cotton single yarns

CB: cotton bundles

CF: cotton single fibres

MCY: mercerized cotton yarns

MCYH-x-y, DMCY-x-y and DMCA-x-y: a mercerized cotton yarn hydrogel, a dried mercerized cotton yarn and a dried mercerized cotton array respectively, dissolved at temperature 'x' (°C) for 'y' (hours)

MCYH: mercerized cotton yarn hydrogels

DMCY: dried mercerized cotton yarns

DMCA: dried mercerized cotton arrays

FOG: first order global model

NY-raw: raw natural cotton yarns

MCY-raw: raw mercerized cotton yarns

M_w : weight-average molecular weight

M_n : number-average molecular weight

MWD: molecular weight distribution

MALLS: multi-angle laser light scattering

RI: refractive index

M_η : viscosity-average molecular weight

$E_{a,s}$: dissolution activation energy

DTG: derivative thermogravimetric analysis

GSM: grams per square metre

Uni or 90/0 -a(b) or/and -c(d): Uni and 90/0 stand for the unidirectional alignment and 90/0 alignment respectively, and a(b) means the first processing step is @ 'a' MPa for time of 'b' min, and if available the second processing step is @ 'c' MPa for time of 'd' min

MCYF: mercerized cotton yarn-woven fabrics

E_a : activation energy

CF_{XRD} : coagulation fraction based on x-ray diffraction deconvolution

C_{I_0} : cellulose I fractions from an equatorial line scan of the raw sample

C'_I : cellulose I fractions from an equatorial line scan of the processed sample

CF_{OM} : coagulation fraction based on the measurement of optical microscopy

A_{red} : the area of the coagulated material

A_{blue} : the area of the central fibre

α_T : shift factor at temperature T

t : time

R : gas constant

A : pre-factor in the Arrhenius equation

χ^2 : coefficient of determination

T : dissolution temperature

CF_{OM-H} : coagulation fraction based on the mercerized cotton yarn hydrogel

T_H : ring thickness of the mercerized cotton yarn hydrogel

a_H : outer diameter of the hydrogel sample

b_H : diameter of the undissolved/central region of the hydrogel sample

ϕ_{water} : water volume fraction

V_{H_2O} : water volume

$V_{swollen}$: volume of the mercerized cotton yarn hydrogel

V_{dry} : volume of the dried mercerized cotton yarn

$L_{swollen}$: length of the mercerized cotton yarn hydrogel

L_{dry} : length of the dried mercerized cotton yarn

$A_{swollen}$: cross section area of the mercerized cotton yarn hydrogel (either the outer ring or the central core)

A_{dry} : cross section area of the dried mercerized cotton yarn (either the outer ring or the central core)

R_{ring} : swelling ratio of the outer ring

R_{core} : swelling ratio of the undissolved central core

\bar{R}_{core} : average swelling ratio of the undissolved central core

\bar{R}_{ring} : average swelling ratio of the outer ring

\bar{R}_{raw} : average swelling ratio of the raw sample

$\bar{\phi}_{water}^{raw}$: average water volume fraction of the raw sample

$\bar{\phi}_{water}^{core}$: average water volume fraction of the central core

$\bar{\phi}_{water}^{ring}$: average water volume fraction of the outer ring

a_D : diameter of the whole dried mercerized cotton yarn

b_D : diameter of the central region of the dried mercerized cotton yarn

r : radius of the dried raw sample

r' : radius of the wet raw sample

R_o : swelling ratio of the raw sample

γ : conversion factor of the reactant

$k(T)$: rate constant at temperature T

$f(\gamma)$: reaction model

w_t : sample weight at time t

w_{H_2O} : initial water weight in samples

w_o : initial sample weight

w_∞ : residual char weight

β : heating rate

β' : instantaneous heating rate

β_t : target heating rate

$\beta'(T_j)$: instantaneous heating rate at temperature T_j

$\overline{\beta}_i$: average heating rate

γ : conversion factor equal to $1 - \gamma$

T_m : temperature at the maximum pyrolysis speed

$[T_m]$: intrinsic temperature at the maximum decomposition rate

β_i^{max} : maximum instantaneous heating rate

β_i^{min} : minimum instantaneous heating rate

Δ : difference of two values

I_L : integration result of the left-hand side of the equation

I_R : integration result of the right-hand side of the equation

G : gradient

E_{lnT}^i : pyrolysis activation energy calculated via the lnT method with a temperature range of i

E_T^i : pyrolysis activation energy calculated via the T method with a temperature range of i

$E_{1/T}^i$: pyrolysis activation energy calculated via the 1/T method with a temperature range of i

$[E]$: intrinsic pyrolysis activation energy

$\overline{[E]_{\beta_t}}$: average intrinsic pyrolysis activation energy at a target heating rate of β_t

$\overline{[E]_{NY-raw}}$: average intrinsic pyrolysis activation energy of the raw natural cotton yarn

$\overline{[E]_{MCY-raw}}$: average intrinsic pyrolysis activation energy of the raw mercerized cotton yarn

$[E_{\beta_t}]$: intrinsic pyrolysis activation energy at a target heating rate of β_t

F : force

S : cross section area

σ : tensile stress

W : width

d : thickness

ε : strain

Δl : difference in length

l_o : original length

G' : Young's modulus

$\Delta\sigma_e$: changes in stress

$\Delta\varepsilon_e$: changes in strain

\bar{F} : average load

P : peel strength

r_{max}^{shaded} : maximum shaded area

r_{min}^{shaded} : minimum shaded area

Chapter 1 Introduction and literature review

1.1 Introduction

Polymer composites are usually composed of at least two distinct phases, reinforcement and matrix, of which the former is usually providing stiffness with higher Young's modulus and strength to the composites, while the latter is acting as a continuous constituent with flexible and soft mechanical properties that connects reinforcement such as particles and fibres together. Generally, a good combination of those two phases, the interaction between matrix and reinforcement, is always of concern when they are made of different materials. Weak interaction between them will lead to poor mechanical properties and will cause material failure in their applications, especially for those structural materials. Most of the polymer composites, such as plastics are petroleum-based and depend on the finite fossil-fuel resource estimated to be exhausted in 100 years, according to the currently discovered reserves. Besides, the plastic contamination in a region is barely reversible due to the natural mineralization process happening very slowly, which makes the plastic pollution entering speed higher than rate of clean-up in most cases. The plastic pollution results in potential impacts to the environment including, imbalance of carbon and nutrient cycles, habitat changes within ecosystems, ecotoxicity and some societal impacts. Although these problems have been known for decades and much research has been reported to recycle the plastics, most of the plastics are still not able to be recycled but landfilled or incinerated. Apart from that, lots of energy is usually needed for the separation of different phases in composites. Therefore, more and more attention has

been paid on not only the recycling of plastics but also the defossilization, by replacing those petroleum-based materials with renewable and biodegradable materials [1].

Consequently, the interest in biopolymer-based composites as a potential solution to the problems mentioned to replace those petroleum-based polymer materials and achieve carbon-neutral cycles is increasing. Cellulose is the most abundant biopolymer in nature, mostly existing in plants and working as the main structural component. Thus, it has huge potential to be used as a substitute of petroleum-based polymers. Although cellulose is so widely available and used in our daily life, products such as wood board, paper and cotton clothes are not efficiently recycled at the end of their life. Instead, most of them are either landfilled or incinerated, leading to the carbon stored in cellulose releasing into the atmosphere. Further, the processing of cellulose-based products consumes lots of energy and other resources, for instance the global average water footprint for 1 kg of cotton is around 10 tons. If their end-life waste such as clothes are not disposed of in a sustainable way, the 'green' effect of cellulose will be significantly restricted. Therefore, different ways were investigated to prolong those cellulose-based materials' life, including down-cycling and up-cycling [2]. For the former, cellulose-based wastes are processed to be lower value products than their original, such as the creation of newspaper out of writing paper. While, for upcycling, cellulose wastes are converted into greater-value products, such as ACCs made from waste clothes [3]. It is this aspect which is the scope of this thesis.

An all cellulose composite is also known as a single component composite or self-reinforced composite, where both the reinforcement and matrix are made

out of cellulose [4]. Therefore, the problem of weak interaction and compatibility between the matrix and reinforcement can be solved. Meanwhile, the cellulose-based waste can be upgraded to structural materials with greater values instead of landfill, incineration or being down-cycled. But unlike most of the petroleum-based polymers, cellulose is not meltable at elevated temperatures or dissolvable in most general solvents such as water, ethanol without chemical modification [5]. Until now, several direct (non-derivatizing) solvent systems have been reported to dissolve cellulose and fabricate all cellulose composites, such as a urea/NaOH/H₂O system, NMMO and LiCl/DMAc [6]. However, most of them are harmful to the environment and difficult to recycle. Recently, some ionic liquids have been found to be able to dissolve cellulose as direct solvents [7] and can be used to make all cellulose composites [8-12]. Due to their notable advantages, such as high thermal stability, chemical stability, numerous combinations of anions and cations and low vapour pressure, ionic liquids have huge potential to be 'green' solvents for dissolving cellulose and making all cellulose composites.

1.1.1 Project aims and objectives

In this project, the aim has been to investigate the dissolution behaviour of cotton materials in an ionic liquid, pyrolysis kinetics of cotton materials and the fabrication of cotton-based all cellulose composites with the ionic liquid. Attention has been put on the 1-ethyl-3-methylimidazolium acetate ([C₂mim][OAc]) as a promising cellulose solvent which has been widely investigated in our group [13-15]. Water is chosen to be the anti-solvent for coagulating cellulose. Two cellulose sources, from a native cotton thread and a mercerized cotton thread, are taken for the research of dissolution of

cellulose in [C2mim][OAc] and the research of pyrolysis kinetics. Different dissolving conditions are designed with two parameters, time and temperature, to explore the dissolution behaviour through working out dissolution master curves and dissolution activation energies. A modified pyrolysis model, based on non-isothermal TGA test, is applied to express the pyrolysis behaviour and attain the pyrolysis activation energy.

A mercerized cotton cellulose-based textile (a basket plain weave) and [C2mim][OAc], are used to fabricate all cellulose composites (ACCs) with the partial dissolving method, also known as the one-step method, where the cellulose samples are partially dissolved to form the matrix phases bonding different threads to form a composite. Different fabricating conditions by varying pressure, number of pressing stages, pressing time and alignment of two layers are implemented to make ACCs, where the outcomes from the research of dissolution of the mercerized cotton thread are used to tune the dissolving time and temperature.

1.1.2 Thesis outline

There are 7 chapters in this dissertation, and they are summarized as follows: Chapter 1 introduces the project and reviews the recent literature to give a broad understanding of the research field. The experimental section is introduced in Chapter 2. In Chapter 3, the details of how to investigate the dissolution of the native cotton threads with different arrangements (fibre, arrays and bundle) in [C2mim][Ac] are described, based on Paper I. Chapter 4 describes the results of dissolution of mercerized cotton threads which are mainly based on Paper III. In Chapter 5 the two cotton samples are compared

according to their dissolution behaviour and pyrolysis behaviour, which is the main content of Paper IV. Chapter 6 provides the outcomes of fabrication of ACCs, and eventually in Chapter 7, the conclusions and suggestions for future work are summarized.

1.2 Literature review

1.2.1 Cellulose

Cellulose is the most abundant biopolymer in nature with renewability, biodegradability and recyclability, of which the annual production is about 150 billion tons [16]. It exists in almost every plant on earth, acting as the structural material in plant cell walls, which makes the plants stiff and strong due to its high Young's modulus [17-19]. The most commonly used cellulose in industry is in the secondary cell wall where lignin acts as the matrix and hemicellulose acts the crosslink points between lignin and cellulose. The proportions of individual components vary by plant species. Cotton possesses the highest cellulose content, about 90 %, which is much higher than wood with about 40 %, see Table 1.1. Additionally, cellulose can be generated by some microbials, fungi, algae and bacteria [20, 21].

Table 1.1 Carbohydrate composition of plant cellulose materials. Credit: Sundarraj et al. [20]

Source	Cellulose (%)	Hemicellulose (%)	Lignin (%)	Extract (%)
Hardwood	43–47	25–35	16–24	2–8
Softwood	40–44	25–29	25–31	1–5
Bagasse	40	30	20	10
Coir	32–43	10–20	43–49	4
Com cobs	45	35	15	5
Com stalks	35	25	35	5
Cotton	95	2	1	0.4
Flax (retted)	71	21	2	6
Flax (unretted)	63	12	3	13
Hemp	70	22	6	2
Henequen	78	4–8	13	4
Istle	73	4–8	17	2
Jute	71	14	13	2
Kenaf	36	21	18	2
Ramie	76	17	1	6
Sisal	73	14	11	2
Sunn	80	10	6	3
Wheat straw	30	50	15	5

Cellulose was initially revealed by a French chemist, Anselme Payen, and extracted from plant substance in 1838. Celluloid derived from cellulose by mixing cellulose nitrate with camphor was the first thermoplastic polymer produced and industrialized in 1870. Its polymer chemical structure was determined by Hermann Staudinger in 1920 [20].

(1) Chemical and physical properties

A cellulose molecule can be formed by dehydration condensation of D-glucose units which are linked by beta-1,4-glycosidic bonds, and its degree of polymerization (DP) can vary from 300 to more than 10000, dependent on different cellulose sources. The DP values in wood pulp are usually ranging from 300 to 1700 and in the case of fibres from plants such as cotton are

typically between 800 and 10000. In microbial cellulose, DP values are found to be 2000-6000 [22].

Cellulose is a linear multi-dispersed homopolymer with units of beta-D-glucoses which are flipped over with respect to one another. There are three free hydroxyl groups at C-2, C-3 and C-6 atoms, see Figure 1.1(a). These hydroxyl groups and the oxygen atoms on the pyranose ring lead to abundant hydrogen bonds networks. The intramolecular hydrogen bonds are formed between two condensed monomers which enhance the stabilization of the network and result in a linear configuration of molecular chain. The intermolecular hydrogen bonds connecting two cellulose molecular chains make several molecular chains that stack up. The hydrogen bond plays important role in the cellulose crystalline structure and then the physical chemistry properties, such as solubility, chemical stability and mechanical properties [22].

Compared to starch molecules (Figure 1.1(b)), cellulose molecules have a higher chance of forming intramolecular and intermolecular hydrogen bonds. Furthermore, the cellulose molecules are in a stretched-out configuration and have higher DP than that of starch which makes cellulose fibres strong and difficult to be dissolved in general solvents. However, starch can dissolve in water and be digested by humans to provide energy to humans and plants, but not cellulose, because there are no cellulose enzymes in our bodies [22].

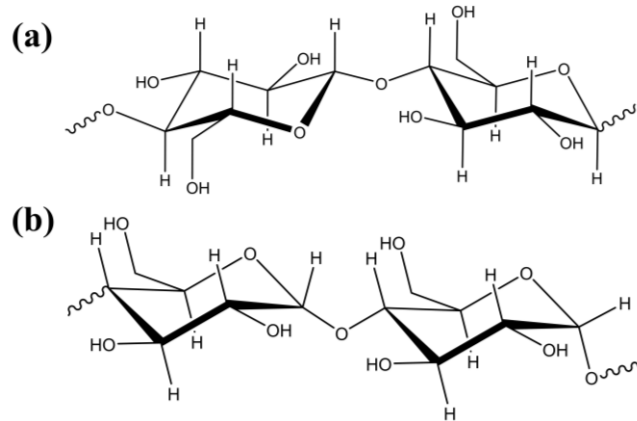


Figure 1.1 Molecular structures of (a) cellulose and (b) starch

During the production of cellulose in plants, disordered regions with randomly oriented molecular chains and ordered regions with aligned molecular chains are formed. The former is responsible for cellulose being flexible and extendable, but the latter makes cellulose stiff with high modulus. Cellulose is a semi-crystalline polymer, it is very important to study different crystalline structures (crystal allomorphs) and their conversions [22].

Figure 1.2 depicts the conversions of various forms of cellulose crystalline structures to one another, and Figure 1.3 shows the XRD results. The compounds cellulose I and cellulose II, which are identified in our cotton samples in this thesis, are discussed in depth here. Cellulose I (in Figure 1.3, the first from the top in (b) and the first from the bottom in (a)), commonly known as native cellulose, is a naturally existing cellulose formed by organisms. The quantities of two distinct polymorphs, cellulose I alpha and cellulose I beta, varies in different organisms. Cellulose I alpha is mostly found in bacteria and algae, whereas cellulose I beta is mostly found in plants such as cotton. Cellulose II, (in Figure 1.3, the fourth from the top in (b) and the second from the top in (a)), commonly known as man-made cellulose, is

produced via regeneration and mercerization of cellulose I. In the regeneration process, native cellulose is dissolved in a solvent and subsequently coagulated by an anti-solvent, such as ethanol and water, to produce cellulose II. To mercerize cellulose, an alkali aqueous solution, usually about 20 wt% caustic soda, is used to convert cellulose I to cellulose II [23]. Cellulose II has an anti-parallel molecular chain structure, making it more thermostable than cellulose I which has a parallel molecular chain arrangement. As a result, cellulose I to cellulose II conversion is irreversible [21]. Despite the fact that cellulose II is more thermodynamically stable, the Young's modulus of cellulose I along the direction of the chain axis is larger than that of cellulose II, as seen in Table 1.2. X-ray diffraction and Raman spectroscopy have been described as experimentally useful techniques to measure the mechanical properties of cellulose allomorphs [18, 24].

Table 1.2 Elastic moduli of different cellulose allomorphs found from literature, where only those considering intramolecular hydrogen bonding are tabulated

Cellulose allomorph	Elastic modulus (GPa)	Method	Reference
Cellulose I	120-143	Experimental	[17-19]
	145-180	Theoretical	[25-28]
Cellulose II	88, 106-112	Experimental	[17, 19]
	162.1, 98	Theoretical	[29, 30]
Amorphous region	9.35, 10-11, 12-14	Theoretical	[31-33]

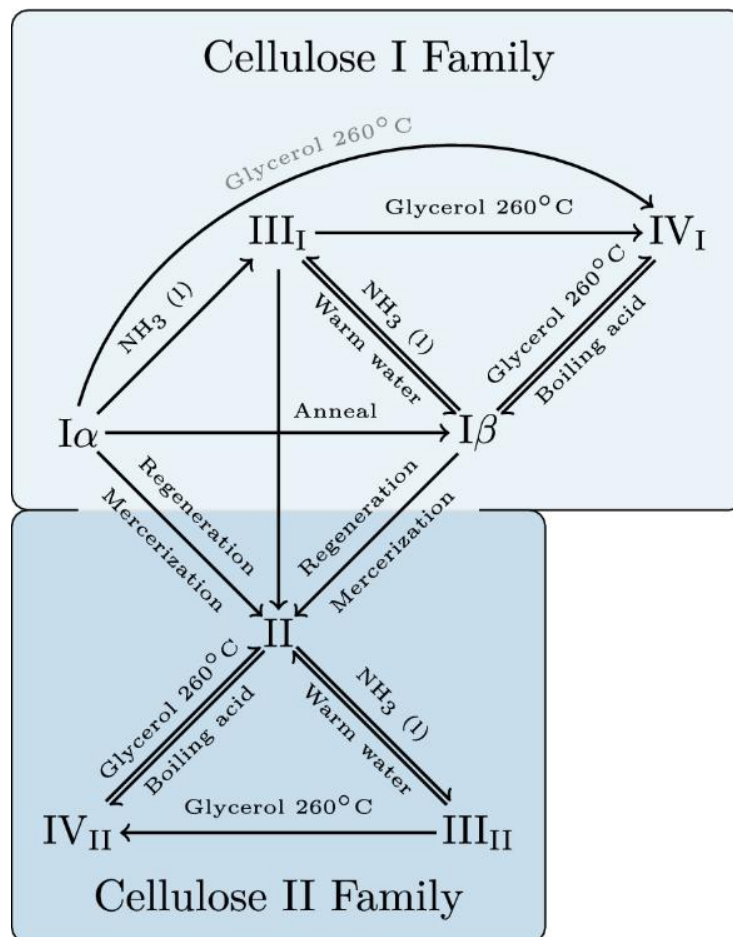


Figure 1.2 Cellulose crystal allomorphs and conversions between each other.

Image taken from the paper by Ottesen [34]

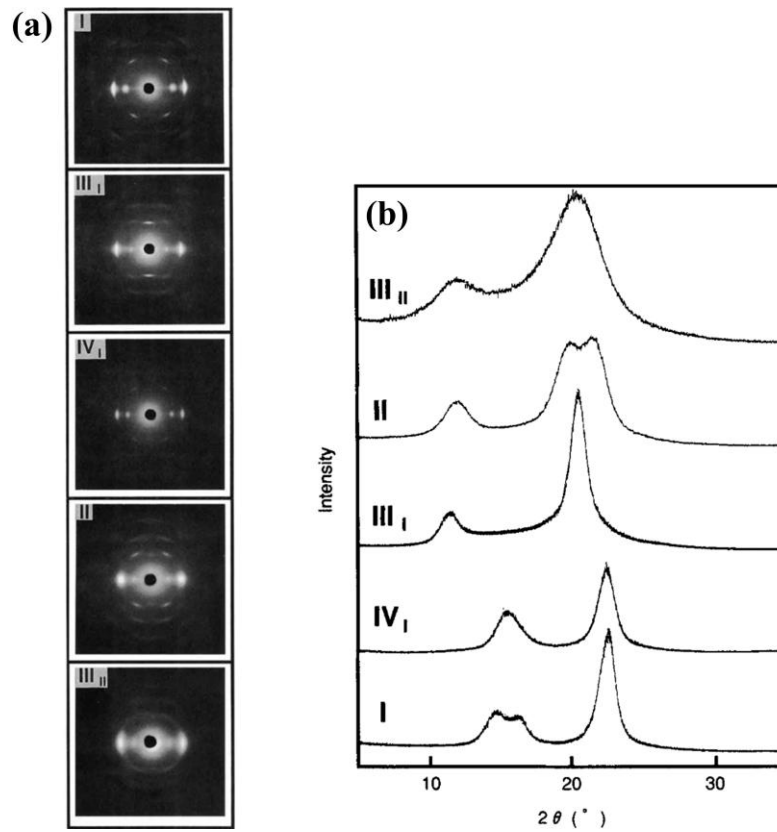


Figure 1.3 (a) XRD 2D patterns of different cellulose fibre polymorphs and (b) their equatorial XRD profiles. Cellulose I (the first from the top in (b) and the first from the bottom in (a)) and cellulose II (the fourth from the top in (b) and the second from the top in (a)) are discussed in this thesis. Credit:

Nishino et al. [17]

Due to the prevalent number of hydrogen bonds existing among intra and inter cellulose molecules, the melting point of cellulose is higher than its degradation temperature, which makes the melting process commonly applied to some general polymers such as polypropylene unfeasible. Likewise, most general solvents, e.g. water and ethanol, cannot dissolve cellulose, until in 1846 Christian Friedrich Schoenbein discovered the first process for the dissolution of cellulose [6]. In the following sections, the solvent systems of cellulose are detailed.

(2) Cellulose solvent systems

Cellulose is insoluble in water and most organic solvents because of its highly crystalline structure and extensive intra-molecular and inter-molecular hydrogen bonds. Only after the hydrogen bonds are broken can it be dissolved [35]. In 1980, Turbak [36, 37] classified cellulose solvents into several groups, in terms of the interactions between cellulose and solvents, as: cellulose is acting as a base while the solvent is an acid; cellulose is acting as an acid with the solvent to be a base; cellulose is treated as a ligand while the solvent is a complexing agent, such as Cuam; and cellulose is a reactive agent and converted to a soluble cellulose derivative, either by functionalizing the hydroxyl groups or not prior to the dissolution of cellulose. More recently, cellulose solvents are classified, according to the need of a chemical modification on cellulose prior to its dissolution, into derivatizing and non-derivatizing solvent systems [38].

Derivatizing solvents systems

Before cellulose is dissolved, several chemical modifications are used to functionalize the hydroxyl groups, such as nitration [39-42], esterification [43], etherification [44] and xanthation [45]. But the processes are usually complicated and environmentally-unfriendly. For example, the first industrialized process for fabricating Rayon fibre, known as the viscose process, in which the very toxic carbon disulphide and aqueous sodium hydroxide, harmful to the environment, are used to make sodium cellulose xanthate. Then cellulose can be generated from the solution of sodium cellulose xanthate dissolved in aqueous sodium hydroxide by the treatment with an acid such as sulphuric acid, which is another harmful reagent for

human beings and the environment. Toxic gases, such as H₂S and SO₂, are discharged during this process, leading to heavy pollution[46, 47]. After the chemical modification, cellulose derivatives could be mostly dissolved in common polar organic solvents such as dimethyl sulfoxide (DMSO) and acetone, while this process is out of the scope of the studies in this thesis, due to the complicity and/or toxicity to the environment.

Amine oxide procedure

N-methylmorpholine-N-oxide monohydrate (NMMO) is one of the most important amine oxides as cellulose solvents. Likewise, it is another commercialised cellulose solvent system, industrially producing Lyocell (also known as Tencel® fibres). There is no need of pre-treatment and derivatization to dissolve cellulose, and the process is shown in Figure 1.4, depicting that lyocell can be spun from an NMMO/cellulose solution by adding an anti-solvent such as water. Due to its environmentally friendly nature, the NMMO-based approach initially published by Johnson in 1969 [48, 49] is considered an alternative to the viscose process, and the comparison in chemical mechanisms between the two approaches is shown in Figure 1.5. Although it is by far the most industrialised alternative to the viscose process, there are still a number of issues, including the NMMO/water system's poor thermal stability, cellulose degradation caused by by-product formation, and the need for stabilisers, which makes the process more complicated and increases the cost [16, 50].

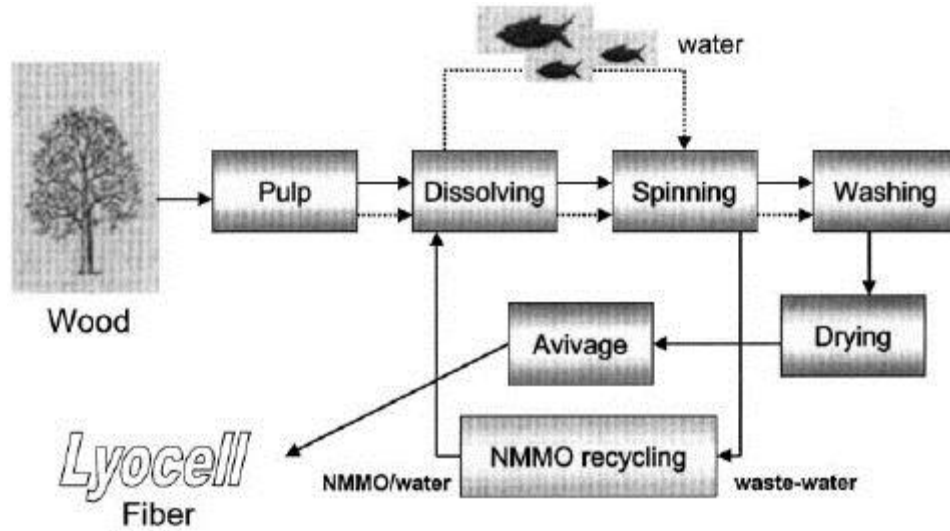


Figure 1.4 Industry process of dissolving cellulose with NMMO to generate Lyocell fibres. Image taken from the paper of Rosenau et al. [50]

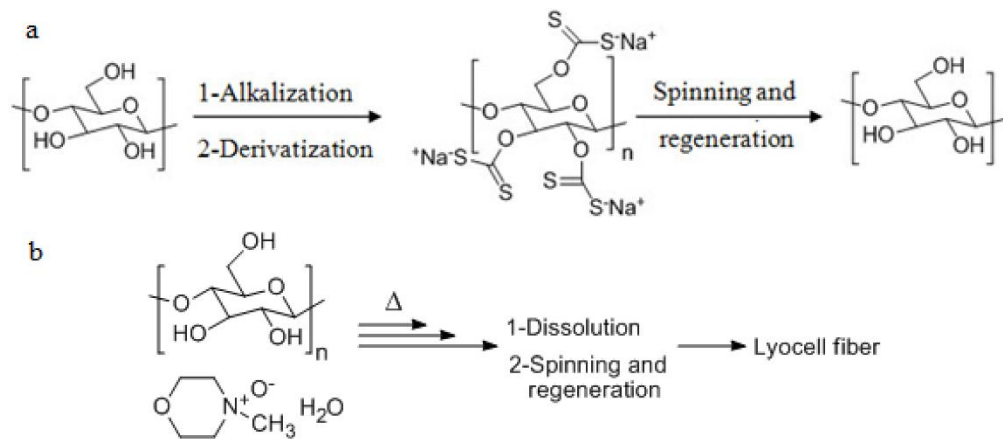


Figure 1.5 Comparison of the two important approaches, (a) viscose and (b) Lyocell process. Credit: Isik et al. [51]

Lithium chloride/N,N-Dimethylacetamide (LiCl/DMAc)

The history of dissolving polysaccharides by LiCl/DMAc system can be traced back to 1980s [52]. Its dissolving mechanism is depicted in Figure 1.6 and it is widely thought that the protons on cellulose hydroxyl groups connect with the Cl⁻ via strong hydrogen bonds; and the cellulose intermolecular hydrogen bonding network is broken in combination with the Li⁺ Cl⁻ ion pairs splitting;

further, complex cations of Li^+DMAc_x form, which accompany the hydrogen-bonded Cl^- to make the electric balance [53]. Prior to the dissolution by a LiCl/DMAc mixture cellulose has to be processed by an activation procedure in which the fibre is first rinsed with a polar medium [54]. Without the activation step, it could take thousands of hours to dissolve cellulose. Another drawback is the limited solubility of cellulose in LiCl/DMAc mixture, as the cellulose solubility increases with LiCl concentration while the solubility of LiCl has been reported up to 8.46 wt%, by Potthast et al. [55].

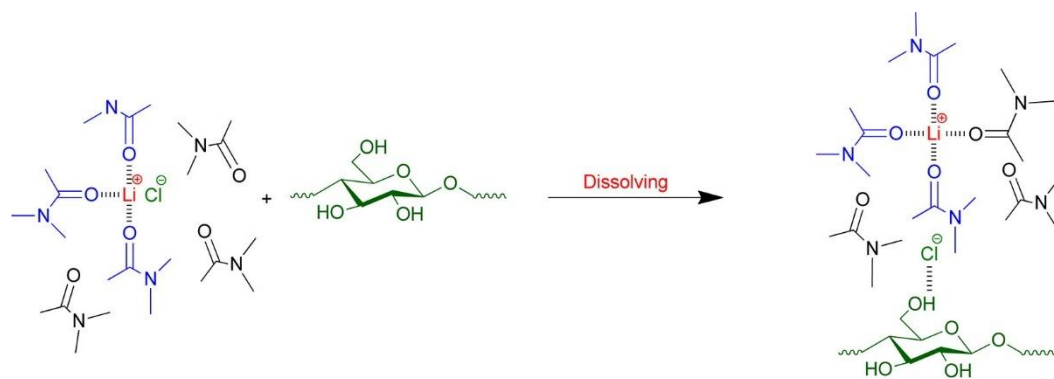


Figure 1.6 Schematic mechanism of the dissolution of cellulose with the LiCl/DMAc mixture. Credit: Zhang et al. [53]

Sodium hydroxide (NaOH) aqueous solution

Due to the simplicity of NaOH/water systems, they have attracted huge attention to the application of dissolving cellulose. The history of the dissolution of cellulose with NaOH/water systems dates back to the 1930s [56, 57] and this finding was barely used until the 1980s. The dissolution of cellulose by a $\text{NaOH}/\text{Urea}/\text{water}$ system was first reported in 1990 by Laszkiewicz and Wcislo [58, 59]. As a result of the non-dissolution of cellulose in the $\text{NaOH}/\text{Urea}/\text{water}$ system at ambient or high temperature, a relatively low temperature (below 0°C) is required in this method, which costs more

energy than those needing higher than ambient temperature [60]. Another disadvantage is the difficulty to recycle the solvent system.

Ionic liquids

The definition of ionic liquids (ILs) was provided by Walden as those bulky organic salts comprising of ions, cations and anions, with melting point below 100 °C [61]. The first report about dissolving cellulose by ILs can be traced back to the patent published by Graenacher [62]. ILs have been considered to be a green solvent with huge potential to dissolve cellulose because of its benefits, such as high stability, sustainability and non-toxicity [6, 7, 46]. More details will be introduced in section 1.2.2, as an ionic liquid, [C2mim][OAc], will be applied as the solvent in the research on the dissolution kinetics of cellulose in this thesis.

(3) Cellulose coagulation

The coagulation of cellulose is a solidification process, where the cellulose is coagulated from its solution to a solid state [63-65]. It usually consists of two processes of which the first is the removal of the cellulose solvent by a suitable anti-solvent, followed by a drying process to evaporate those coagulants. In the first process anti-solvents, such as water [66], ethanol [67] and acetone [68], can stop the dissolving process by breaking the hydrogen bonds between solvent molecules and cellulose molecules and forming new hydrogen bonds between solvent and anti-solvent molecules [11, 69]. For the example of ILs solvents, the adding of anti-solvents reduced the basicities of solvents, which could be confirmed by the decrease in Kamlet-Taft value of $\beta - \alpha$, also known as the net basicity [63, 70].

It has been found that coagulating conditions (including the coagulating temperature, the coagulant type and the ratio of coagulant to solvent), cellulose molecular weight/degree of polymerization, and cellulose concentrations in solutions influence the coagulating rate [63, 67, 70-75]. Further, the coagulating rate significantly affects the properties, such as transparency, mechanical properties, of the coagulated cellulose by changing its crystallinity and crystalline size [63]. For example, transparent films were generated in an ethanol coagulating bath compared with opaque films formed in a water coagulating bath, from cellulose/[C2mim][OAc] solutions [71]. The mobility of cellulose chains was concluded as the main parameter correlating to crystallinity and crystalline size [11, 63]. Additionally, the drying process can play a role in the final regenerated cellulose properties [71]. Therefore, it is feasible to vary the properties of the cellulose products by manipulating the coagulant concentration and the parameters such as the temperature in the subsequent drying process [11].

1.2.2 Ionic liquids

(1) Unique properties

Ionic liquids, consisting of cations and anions, are often described as a salt in a molten state below 100 °C [61]. This is quite different to a general salt such as NaCl, whose melting point is much higher, of the order of 800 °C, due to its regular lattice structure [76]. The reason for this special property of ILs is thought to be the decreased columbic interactions derived from the disassociated and asymmetrical charge tendency of its component ions. The lattice structure is disrupted into a disordered one leading to a decrease in the melting point [46, 77-79].

There are abundant combinations of cations and anions which lead to a huge number of ILs. Different cations and anions commonly used are listed in Figure 6. The special molecular structure of ILs results in a wide range of special and interesting properties [80].

Negligible vapour pressure

The volatility of ILs is very low and this is one of the main reasons for their increasing usage and being of so much interest [7, 80]. It is reported that ionic liquids possess negligible vapour pressure [79] compared to typical organic solvents such as ethanol, which are usually much easier to be evaporated even than water [78]. Therefore, it is usually easy to remove other products which are liquids with relative high vapour pressure from the ionic liquids. In addition, low vapour pressure makes it safer in terms of potential air pollution, and in this case it is not toxic for humans due to the reduced risk of breathing it into our body [80].

Thermal stability

Nonflammability is another advantage of ionic liquids, which makes them safe and green. ILs always stay thermally stable at relative high temperatures at which general organic solvents would be on fire or dramatically evaporating. So, the explosion hazard can be removed just by using ionic liquids as a chemical reaction medium/catalyst [80-83].

Broad liquid applied range

Ionic liquids can be used in a broad temperature range while still remaining in the liquid state. This temperature range is determined by the temperature span between the melting point and the boiling point or thermal degradation temperature. When ionic liquids are not evaporated and boiled by high temperature, the upper temperature is considered to be the degradation temperature. As a result, for experiments, ionic liquids can be used at a wide temperature range without worrying about their loss/evaporation [79, 84, 85].

Wide range of solubility and miscibility

Because of the abundance of combinations of cations and anions, which can be easily designed, the polarity and coordination between ions is easily modified [86]. Therefore, ionic liquids have more strongly solvating properties than most organic solvents. As reported in the literature, ionic liquids can be designed to dissolve many substances including both organic and inorganic items and gases, liquids and solids, such as CO₂ [87], benzene [88], carbohydrate [89], transition metals [90, 91], enzymes [92, 93], antibiotics [92], coal and rocks [94]. Furthermore, ILs can also dissolve both natural and synthetic polymers, for example cellulose and nylon [95, 96].

Applicable properties in chemical reactions

Ionic liquids can be used as a dual agent in a large variety of chemical reactions [97, 98]. For example, ILs can act as a medium and/or catalyst in a chemical reaction, as they can be treated as Lewis acid or base, which relies on the combination of the properties of the cations and the anions in the ionic liquid [98, 99].

Designable properties

As discussed above, the properties of ionic liquids can be tailored and designed, which makes them applicable to a wide range of research fields. In general, there are several uses that have been reported:

- (1) Functionalizing specific functional groups into the cations and/or anions [100].
- (2) Combining different cations and anions [100]
- (3) Making mixtures of different ionic liquids [101].

Sustainability

The recyclability of Ionic liquids applied in processing cellulose has been reported in the literature [102], and an excellent recovery of ionic liquids has been achieved by recycling it from the waste liquids and then reusing it as a solvent for cellulose [103]. The recycled ionic liquids can also be obtained from the chemical reaction in which it acts as a medium or a catalyst [104-106].

(2) Limitations of ionic liquids

Although there are significant advantages of applying ionic liquids, there are still some limitations, which have to date slowed down the speed of their industrialization, and these problems have not yet been solved.

Price

The high price of most of ionic liquids has been considered to be the most significant restriction to their applications in industry. Most of them are much

more expensive than conventional organic solvents. The high cost of raw materials, complexity of their fabricating processes and high purity requirement make ionic liquids expensive. But Helmut Kaiser Consultancy predicts that the demand for ionic liquids will increase dramatically during the upcoming fifteen years, which will lead to a significant decrease in their price [107]. Obviously, in some cases, the use of slightly expensive ionic liquids may be acceptable if the advantages related to their application are able to compensate for the additional costs of the solvent [108-110].

Low flowability

Most ionic liquids have comparable viscosities to oils, which are orders of magnitude greater than general organic solvents [111]. This issue results in high energy consumption and increased time required to mix them with other products in many industrial applications depending on the mass transfer. Due to the high viscosity of ILs, some co-solvents, such as DMSO and N,N-dimethylformamide (DMF), are often used to dilute it and then make it less viscous [78, 108, 112].

Nonbiodegradability

Most of the designed ILs are not biodegradable especially for the treatment on biomass such as cellulose, and this has been considered as an issue during the sustainability of a process involving ILs. Instead, the recyclability of ILs, attributing to its high stability and low vapour pressure [80], makes them recoverable from general solvents and reusable, which is an encouraging aspect for their applications, especially in the dissolution of biomass as solvents [7].

(3) The mechanism of ionic liquids dissolving cellulose

As discussed before, cellulose can only be dissolved in a restricted number of solvents (but not melted), by disrupting the hydrogen bond networks between intra and inter molecules [35]. Even though ionic liquids have been invented for over 100 years, and the first report of ionic liquids acting as the solvents of cellulose was in 1934 by Graenacher [62], research on dissolution of cellulose with ionic liquids was developed for just the most recent 20 years [61], especially since the research reported by Swatloski et al. in 2002 [7]. The mechanism of dissolving cellulose with ionic liquids is gaining growing attention, however it has not been completely understood. There are several hypotheses raised, and the most acceptable one is that the anions in the ionic liquids play a predominant role by competing with the oxygen atoms on the cellulose to form new hydrogen bonds. IIs containing low-basicity anions, such as $[\text{BF}_4]$, $[\text{PF}_6]$, $[\text{N}(\text{CN})_2]$, $[\text{MeSO}_4]$, $[\text{HSO}_4]$ and $[\text{Tf}_2\text{N}]$ are not suitable solvents for cellulose [46, 113]. On the other hand, those IIs with high Brønsted-basicity anions could efficiently dissolve cellulose, for example $[\text{HCOO}]$, $[\text{CH}_3(\text{CH}_2)_{0-3}\text{COO}]$, $[\text{PhCOO}]$, $[\text{HSCH}_2\text{COO}]$ and $[(\text{MeO})(\text{R})\text{PO}_2]$ [46, 113, 114]. Additionally, the cations play a minor role in the solvation of cellulose, and there are several studies that have tried to prove this by molecular simulation studies and NMR measurements [115-117].

In terms of the effect of cations in the dissolution of cellulose, Zhang's group presented a different view, see Figure 1.7. The mechanism proposed by them is that the anions and cations play a synergistic effect on the dissolving process and the role of cations was non-negligible. The relatively small anions prefer to form hydrogen bonds with hydrogen atoms of hydroxyls on the

cellulose molecules, and the protons on the imidazolium cation rings favoured to associate with the oxygen atoms of hydroxyl groups possessing a less steric barrier. And recently this hypothesis is confirmed by experimental and theoretical evidence [118-120]. Additionally, the cations in ILs could also decrease the cellulose solubility if they strongly interact with the associated anions or steric hindrance effect of large size group in their alkyl chains.

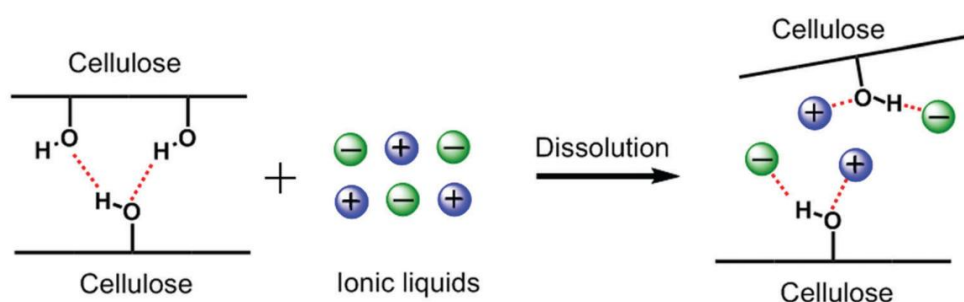


Figure 1.7 Dissolving mechanism of cellulose in ionic liquids. Image adapted from the work of Zhang et al. [46]

Some other fundamental research has been reported on the kinetics and rheology of the dissolution of cellulose in ILs [121-124]. From that research, rheological activation energies of cellulose/ILs solutions are reported to vary from 46 kJ/mol to 70 kJ/mol, which is dependent on the IL and cellulose concentration. Recently, several papers showed that the dissolution of cellulose in ILs followed Arrhenius behaviour [89, 122, 125, 126], and those published by our group indicated that the activation energy of dissolution of natural cotton, natural flax and mercerized cotton in [C2mim][OAc] were 96 ± 3 kJ/mol [89], 98 ± 2 kJ/mol [125] and 73 ± 2 kJ/mol [126], respectively.

Cuissinat et al. investigated the dissolution of cellulose from different sources and cellulose derivatives with different solvent systems, such as NMMO/water

[127-129], NaOH/water [128-130] and ionic liquids [131]. Among them, four phases (Figure 1.8) were reported during the dissolution of cotton and wood fibres in the ionic liquid solvent system, 1-N-butyl-3-methylimidazolium chloride ([C4mim]Cl)/DMSO: phase 1, cellulose balloon formation; phase 2, cellulose balloon breaking; phase 3, dissolving the unswollen regions; phase 4, dissolving the cellulose balloon residues [131]. This is widely accepted as the microscopic cellulose dissolving process with ionic liquids.

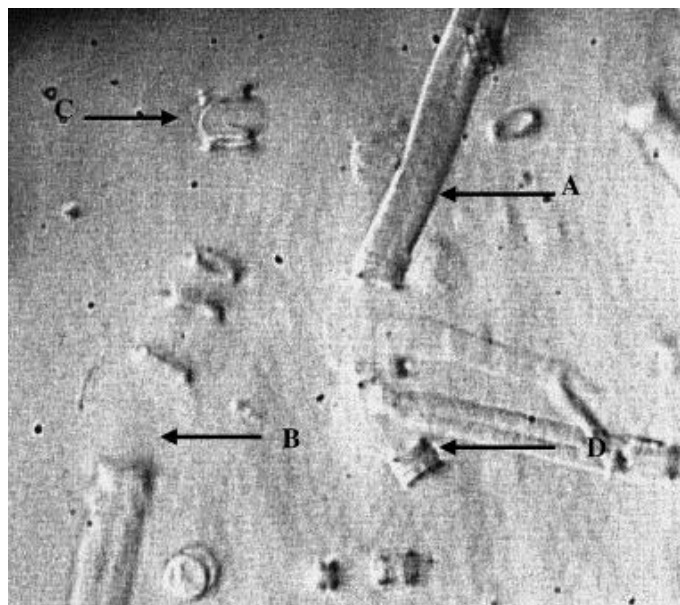


Figure 1.8 Wood fibres in [C4mim]Cl/DMSO observed by optical microscopy and (A) unswollen fibre, (B) balloon, (C) membrane and (D) unswollen section between two balloons. Image taken from the paper of Cuissinat et al. [131], without any scale bar originally provided

1.2.3 The development of ACCs processed by ionic liquids

All cellulose composites are single-component polymer composites, which were first reported by Nishino et al. who embedded ramie fibres in a regenerated cellulose of completely dissolved craft wood pulp with the 2-step method, shown in Figure 1.9 [4]. The issue of poor compatibility seen between

matrix and reinforcement phases in general composites, which are commonly made of different materials with different polarity, can be resolved. For instance a composite made from a high-polarity silica and a low-polarity natural rubber, which then needs an additive named bis(3-triethoxysilylpropyl) tetrasulfide (Si-69) to increase their interaction [132].

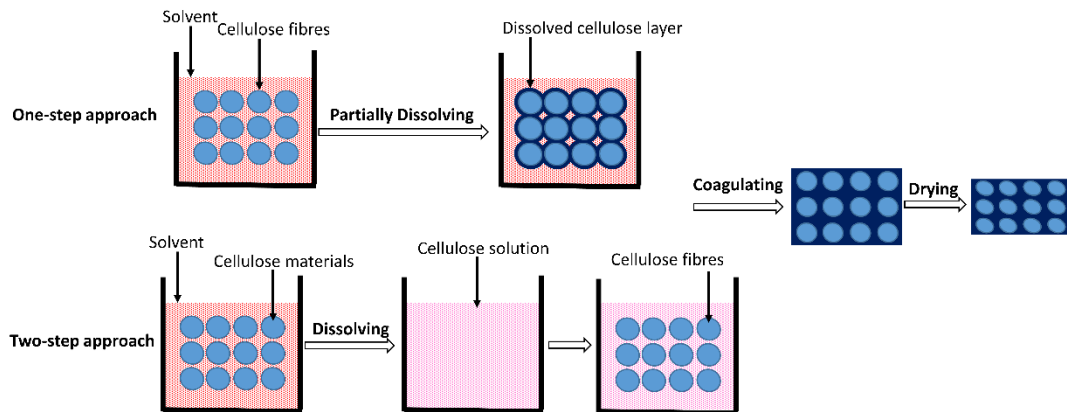


Figure 1.9 Schematic illustration of fabricating approaches for all-cellulose composites: one-step and two-step approaches

As introduced in section 1.2.2(3), some ionic liquids are 'green' and effective solvents for dissolving cellulose, because of high thermostability, chemical stability, negligible vapour pressure and tuneable properties. They have high potential to be applied as solvents in the fabrication of all cellulose composites. Different cellulose sources being applied for the preparation of all cellulose composites with ionic liquids have been reported, and they are reviewed below in terms of the reinforcement material, while those made with other cellulose solvents are out of the scope of this thesis [4, 12, 133, 134].

Microcrystalline cellulose or micro/nanofibrillated cellulose based ACCs

Microcrystalline cellulose (MCC), microfibrillated cellulose (MFC) and cellulose nanofibres (CNF) are in the size range from nano-meters to microns in diameter, made by chemical or mechanical processing of cellulose, such as acid hydrolysis and mechanical shearing/grind processes. MCC is mostly used as a precursor of the matrix, and as to MFC and CNF, they are good candidates to be reinforcement phases in ACCs because of their high aspect ratio. Several papers [135-138] have reported that ionic liquids, [C2mim][OAc], [C4mim]Cl and 1-(2-hydroxyethyl)3-methyl imidazolium chloride ([Hemim]Cl), could be used to process MCC/MFC/CNF to make ACCs via one-step and two-step methods. Among them some general solvents such as water, acetone and ethanol were applied as the coagulants to coagulate the dissolved cellulose to form the matrix phase in ACCs, of which the highest strength and modulus were 124.1 MPa [135] and 12 GPa [138], respectively. Due to the extra energy cost of making them from those natural plant cellulose materials, the application of MCC, MFC and CNF in fabrication of all cellulose composites is restricted.

Natural plant cellulose-based ACCs

Natural plant cellulose materials, including cotton [139], flax [140], jute [141], wood [142] and natural plant-based materials such as filter paper [143] have been reported to act as the cellulose source in the fabrication of ACCs with ionic liquids.

As introduced before, cotton with cellulose content to be 90%, the highest in plants, has been used as cellulose sources in ACCs. [C2mim][OAc] and

[C4mim]Cl were used to be the solvents in fabrication of cotton-based ACCs. As reported, the highest tensile strength was found to be 68 MPa [144] and modulus to be 134 MPa [139].

Flax fibre possesses cellulose I content of about 70 % and other substances such as hemicelluloses, pectin and lignin of about 30 %. The single flax fibre was reported to have tensile strength of 1.2 GPa, Young's modulus of 60 GPa [145], which indicates huge potential of being used in ACCs. Several flax materials have been reported to make ACCs, including flax nonwoven textile [140], linen textile [146], flax yarns [147], where [C4mim]Cl, 1-butyl-3-methylimidazolium acetate ([C4mim][OAc]) and [C2mim][OAc] were applied as solvents, respectively. The highest tensile strength and Young's modulus were reported to be 151.3 MPa and 10.1 GPa, respectively on the flax yarn-based ACCs made with one-step method [147].

Wood powder [142], sheets [148, 149] and blocks [139] were reported to fabricate ACCs with [C4mim]Cl and [C2mim][OAc]. The highest tensile strength and Young's modulus were found for the ACCs made by wood plies with [C2mim][OAc] to be 430 MPa and 39 GPa, separately [149]. Additionally, other cellulose-based materials, such as denim fabrics, filter paper and hemp fabrics, etc., are reported to make ACCs, and their mechanical properties are summarized and tabulated in Table 1.3.

Regenerated cellulose fibre-based ACCs

Rayon and Lyocell fibres, made from natural sources of regenerated cellulose, consists of only cellulose II and amorphous cellulose. Ionic liquids, [C2mim][OAc] [150], [C4mim][OAc] [146] and [C4mim]Cl [151] were reported to process Rayon and Lyocell fabrics to create ACCs. The ACCs made from rayon fabrics possessed tensile strength and Young's modulus to be up to 144 MPa [150] and 7.3 GPa [152], respectively. Those made from Lyocell textiles were reported to have up to 103 MPa [153] and 7.2 GPa [140] to be tensile strength and Young's modulus, respectively.

Table 1.3 Summary of mechanical properties of ACCs made by one-step and two-step methods with ionic liquids

Solvent/method/coagulant	Reinforcement	Processing temperature (°C) and time	Ultimate tensile strength (MPa)	Modulus (GPa)	Failure strain (%)	Ref.
[C2mim][OAc]/2-step/water	Rayon fabric	Room temperature-80 (0.5 h-24 h)	45-144	1.5-3.6	3.8-16.7	[150]
[C4mim]Cl/2step/water	Rice husk	100-130 (3 h-8 h)	55.8-126.4	13.2-29.2	2.24-26.7	[154]
[C4mim]Cl/1-step/methanol	Canola straw	85 (5 min-8 h)	28-208	5.9-20.0	1.8-9.8	[155]
[C4mim]Cl/1-step/acetonitrile	Cotton fabric	150 (0.5 h)	16-22	0.01-0.13	26-125	[139]
[C4mim]Cl/1-step/acetonitrile	Hinoki Lumber	210 (0.5 h)	12-51	3.3-6.3	11-15	[139]
[C4mim]Cl/1step/ethanol	Wood flour	100 (10 min),210 (13 min)	5.5	1.9	-	[142]
[C4mim][OAc]/1step/water	Rayon textile	110 (80 min)	70.16	2.45	-	[146]
[C4mim][OAc]/1step/water	Linen textile	110 (80 min)	46	0.86	-	[146]
[C4mim]Cl/1-step/water	Microfibrillated cellulose	100 (20 min-160 min)	82.3-124.1	6.9-10.8	1.5-1.9	[135]
[C4mim]Cl/1-step/water	Filter paper	100 (20 min-160 min)	58.6-91.8	4.5-5.8	2.7-3.8	[135]
[C2mim][OAc]/1-step/water	Soft wood kraft pulp-paper	95 (30 min-330 min)	80-192	7.8-17.5	2.0-9.7	[156]
[C4mim][OAc]/1-step/water	Rayon textile	95 (1 h)	65-91	1.08-4.1	-	[157]
[C4mim][OAc]/1-step/water	Rayon textile	95-115 (30 min-90 min)	71.2-77.7	5.4-7.3	-	[152]
[C4mim]Cl/1-step/water	Microfibrillated cellulose	100 (5 h)	-	0.7-1.1	-	[136]
[HeMIM]Cl/2-step/water	Microcrystalline cellulose	85 (2 h)	43.6-51.9	1.2-3.6	2.11-15.9	[137]
[C4mim]Cl/1-step/water	Flax nonwoven textile	103 (1 min)	34	4.6	0.8	[140]
[C4mim]Cl/1-step/water	Lyocell nonwoven textile	103 (1 min)	78	7.2	5.2	[140]
[C4mim]Cl/1-step/water	Lyocell fabric	110 (0.5-4)	35-48	0.25-1.75	17-26	[151]
[C4mim]Cl/1-step/water	Lyocell fabric	110 (3 h)	38-44	0.25-1.8	17-26	[158]
[C4mim]Cl/2-step/water	Lyocell fabric	110 (1 h,2 h)	31-103	0.2-4.2	7.4-28.6	[153]
[C4mim]Cl/1-step/water	Jute fabric	110 (2 h-8 h)	22-29	0.24-0.31	24-37	[141]
[C4mim]Cl/1-step/water	Filter paper	80 (0.5 h-4 h)	7.3-76.4	0.05-1.02	3.28-34.25	[143]
[C4mim]Cl/1-step/acetonitrile	Manchurian ash sheet	100 (1 h)	74.6-214.1	-	3.7-13.0	[148]
[C4mim]Cl/1-step/acetonitrile	Hemp fabric	100 (0.5 h)	47.4-81.1	0.22-1.50	5.5-11.1	[159]
[C2mim][OAc]/1-step/water	Birch wood plie	95 (0.5 h)	430	39	-	[149]
[C2mim][OAc]/1-step/water	Flax yarn	Room temperature (15-60 min)	117.9-151.3	8.4-10.1	2.2-3.0	[147]
[C4mim][OAc]/2-step/water	Denim fabric	95 (1.5 h)	25-29	2.5-4.3	-	[160]
[C2mim][OAc]/1-step/water	Filter paper	60 (5-60 min)	41.7-120.8	1.5-2.7	7.6-18.2	[161]
[C2mim][OAc]/2-step/acetone and ethanol	Cellulose nanofibre	90 (5-10 min)	57-110	5-12	1-8	[138]
[C4mim][OAc]/2-step/water	Denim nonwoven fabric	110 (1 h)	33.1	2.1	-	[3]
[C4mim][OAc]/1-step/water	Denim nonwoven fabric	110 (1 h)	42.7	6	-	[3]
[C2mim][OAc]/1-step/water	Cotton cloth	40, 60 and 80 (0.5 h, 2 h, 24 h)	30-68	-	-	[144]

Compared with the two-step method, the one-step method is relatively simple and could achieve high content fraction of the reinforcement phase in ACCs, where the orientation of the reinforcement phase is easier to be aligned. Additionally, the interfacial interaction between the matrix and the reinforcement phases is generally stronger in the ACCs made via one-step method than those via two-step method, as an identical chemical composition is involved in the one step process. But it is not as easy as the two-step method to control the size and the fraction of matrix content with the one-step method [162]. Among the plant fibre materials, cotton has the highest market occupation [20], however cotton-based ACCs made with ionic liquids possess relatively low mechanical properties, indicating a need to improve the fabrication process to make comparable ACCs from cotton materials.

1.2.4 Summary

All cellulose composites have been successfully prepared by one-step and two-step methods with certain ionic liquids for several years [4, 137, 150, 153, 163]. But there is significant space on the systematic research and preparing processes waiting to be filled. The problems in the application of ionic liquids for dissolving cellulose and making all cellulose composites are summarized as: (1) the mechanism of cellulose dissolution in ionic liquids is still not totally understood; (2) how to control the contents of reinforcement and matrix phases in the one-step ACC fabrication method is yet to solved; (3) the recycling of ionic liquids was rarely reported, which is considered to be the best way to decrease the high costs and protect the environment.

This project will focus on the research in the following aspects:

- (1) the dissolution behaviour of two cotton samples - dissolution master curves and determination of the dissolution activation energy;
- (2) the pyrolysis behaviour of the two samples, using a new pyrolysis activation energy calculation method;
- (3) how to choose a proper cotton yarn, i.e with a lower dissolution activation energy and higher thermostability, from the two samples to make ACCs with the one-step method, and how the results of the dissolution research could direct the matrix/reinforcement ratio.

The findings in this research can deliver informative knowledge and new methods for investigating other cellulose-based materials and in the fabrication of all cellulose composites.

Chapter 2 Experimental

2.1 Materials

Two cellulosic cottons are used as the source of cellulose, one is a natural cotton (obtained from Airedale Yarns, Keighley, UK), the other is a mercerized cotton (100m-nr50, No. 1716, Coats Group plc, UK). 1-ethyl-3-methylimidazolium acetate ([C2mim][OAc]) with purity $\geq 95\%$ was purchased from Sigma-Aldrich Corporation. The water content of [C2mim][OAc] was always below 0.5 wt. % in the experiments, as determined by a Karl Fischer titration machine (899 Coulometer, Metrohm U.K. Ltd., UK). A cold curing epoxy resin (Epoxicure, Cold Cure Mounting Resin from Buehler, UK) was used to embed samples for optical microscopy (OM) and Raman spectroscopy.

2.2 Characterization

2.2.1 Optical microscopy

An optical microscope (BH2-UMA, Olympus Corporation, Japan) with different magnifications (x 50, x 100 and x 200) was used for exploring the morphology of the raw materials and the processed samples in transmission and reflection mode. A camera (UI-3243CP-M-GL, IDS Imaging Development Systems GmbH, Germany) with a resolution of 1280 x 1024 was used to capture photos. Epoxy resin was used to embed dried samples for cross-section observation via the optical microscope, where the mass ratio of epoxy resin and hardener is about 4 to 1 and the mixture was stirred thoroughly before use. The samples were fixed perpendicularly to the polishing surface on the

bottom of a Teflon circular container to which the premixed resin was decanted. Then a curing process was followed: first left at room temperature for 24 hours with a further curing process followed at 50 °C for 5 hours. Finally, a grinding and polishing process was applied with a polishing machine (STRUERS ROTOPOL-11 / ROTOFORCE-1, Struers Ltd., UK) on the epoxy resin, with samples being embedded, to make it about 2 cm thick. All the dried samples were stored at room temperature with a relative humidity of ca. 50 % for over 48 hours before they were embedded in the resin with the above-mentioned method. The image processing software 'ImageJ 1.52d' was used for further size measurement and image processing. Further details can be found in the beginning of each relevant chapter.

2.2.2 Wide-angle X-ray diffraction

For characterizing the crystalline structure of the cotton samples, an X-Ray machine (DRONEK 4-AXES, Huber Diffractionstechnik GmbH & Co. KG, Germany) was used to conduct wide-angle X-ray diffraction (WAXD) under transmission mode on non-powder samples. Three 2θ line scans along the equatorial direction of the 2D X-ray diffraction pattern were carried out on each sample from 5° to 40° with the step of 0.2° per 50 seconds and the X-ray was generated by Cu-K α at 40 kV and 30 mA with a wavelength λ to be 0.154 nm. When samples were mounted on the machine, the axial direction of the samples is perpendicular to the equatorial scan direction (the plane of 2θ line scans). The intensity vs. 2θ curves were obtained by subtraction of a background scan carried out with no sample loaded. All the samples were stored at room temperature with a relative humidity of ca. 50 % for over 48 hours before they were tested under the same condition as mentioned above.

The measurement was repeated three times for each sample, and the width of the sample was larger than the diameter of the X-ray beam, 2 mm.

For analysing the composition of cellulose I and cellulose II in the samples, a deconvolution method was used where cellulose I and cellulose II peaks are deconstructed to subpeaks fitted with Gaussian functions, deconvolution results of the raw natural cotton and the raw mercerized cotton are shown in Figure 2.1(a) and (b) respectively. Diffraction peaks at 14.8° (110), 16.3° ($1\bar{1}0$) and 22.4° (200) are assigned to cellulose I and those at 12.4° ($1\bar{1}0$), 20.2° (110) and 21.8° (200) to the cellulose II crystal structure [164]. It is worth noting that the cellulose I peak at 20.6° (120), see Figure 2.2, cannot be observed on an equatorial scan of our non-powder samples which is therefore not further discussed in this thesis [165]. There is also a broad peak centred at 18.2° of 2θ which belongs to the amorphous fraction. After deconvolution, the summation of area under each peak for different crystal forms was obtained via integration, and the fraction of area summation of each crystalline structure to the total is used for quantifying dissolution; it should be noted that this is not a measure of the absolute cellulose I and cellulose II crystallinity, which would require a powder sample. The cellulose I and cellulose II area fractions are denoted as CI and CII, respectively.

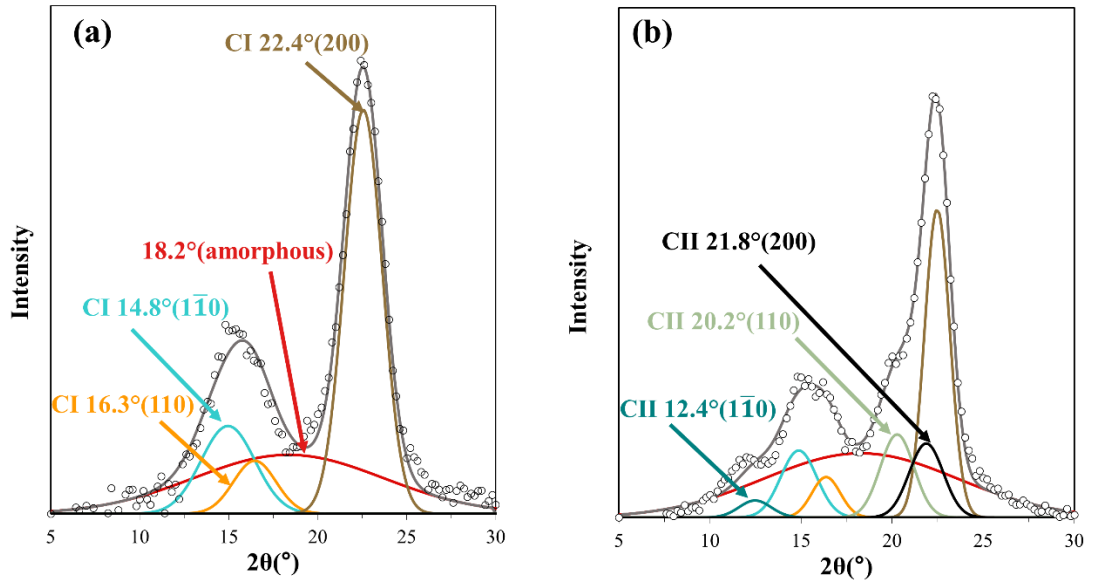


Figure 2.1 WAXD spectrum deconvolution curves of (a) the raw natural cotton sample and (b) the raw mercerized cotton sample with relevant peaks labelled, where the open dots are the raw data and the solid grey lines are summation of all deconvolution peaks, CI and CII represent cellulose I and cellulose II respectively

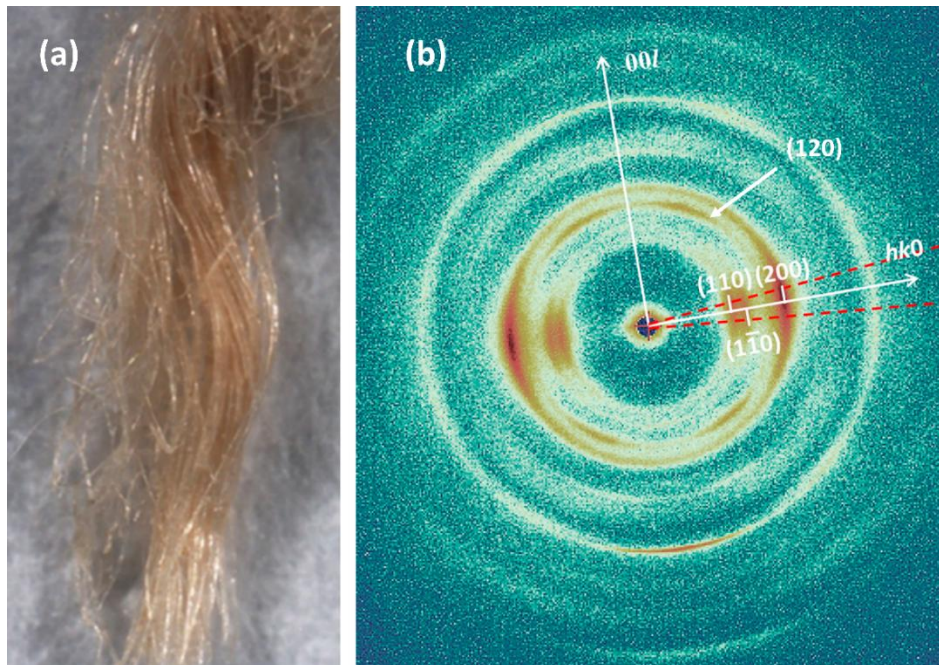


Figure 2.2 (a) Photograph of fibres from a linen sample and (b) its two-dimensional WAXD pattern, where cellulose I crystal peaks are labelled with Miller index. Taken

from the paper by De et al. [165]

Due to the irreversible conversion from cellulose I to cellulose II, the dissolution of cotton samples is marked by changes in the ratio of summation of the 200, 110 and $1\bar{1}0$ peak areas in a line scan to the total area, equivalent to coagulation fraction, CF_{XRD} which can be calculated by the following equation:

$$CF_{XRD} = (C_{I_0} - C'_I)/C_{I_0} \quad \text{Equation 2.1}$$

where C_{I_0} and C'_I represent the cellulose I fractions from an equatorial line scan of the raw sample and the processed sample, respectively. Our hypothesis, which we subsequently confirm, is that although we do not calculate the absolute cellulose I crystallinity, following the reduction in the equatorial cellulose I crystal peaks (200, 110, $1\bar{1}0$) with time and temperature allows the activation energy to be determined from our time-temperature superposition (TTS) analysis. Indeed, our hypothesis is that any parameter that can be quantitatively measured, and therefore tracked as a function of time and temperature, can be used to assess whether TTS holds and hence calculate an activation energy.

Chapter 3 The dissolution of natural cotton cellulose in [C2mim][OAc]

3.1 Introduction

Cotton is the purest form of cellulose among plants consisting of about 90% cellulose [20]. It needs about 1000 gallons of water to grow 1 pound of cotton and requires even more water usage during production of a garment product [166]. Hence many studies [139, 167-170] have been done on recycling cotton-based materials, such as polycotton (blend of cotton and polyester) and cotton fabrics via dissolution process with 'green' solvents, such as ionic liquids (ILs) to increase their sustainability. However, as discussed in the literature review chapter, the dissolution mechanism of cellulose in ILs has not been fully understood and the dissolution activation energy is an important fundamental parameter.

In the following chapter, a natural cotton is chosen as the cellulose source and its dissolution behaviour in an ionic liquid 1-Ethyl-3-methylimidazolium acetate ([C2mim][OAc]) is investigated. This ionic liquid has been widely investigated as a solvent for dissolving cellulose materials in our group [13-15, 125, 171] and indeed by other groups [123, 170, 172-178]. It is a room-temperature ionic liquid - being liquid at room temperature. It is a good cellulose solvent and the maximum cellulose concentration soluble in [C2mim][OAc] has been reported to be around 26 wt.%, but it is very difficult to reach this upper limit because of the extremely high viscosity of such solutions [179].

Here, both WAXD and optical microscopy are used to allow for the growth of the dissolved and coagulated fraction (CF) at different temperatures and times to be quantitatively measured. The effect of cotton sample arrangement including single yarns, arrays and bundles on dissolution in [C2mim][OAc] is studied with TTS. The cellulose dissolution behaviour is quantified by determining a dissolution activation energy for each sample arrangement. The effect of cotton sample arrangement on the dissolution speed is also explored. The content of this chapter is mainly from my publication I.

3.2 Methods

3.2.1 The procedure of dissolving the natural cotton samples with [C2mim][OAc]

The supplied raw natural cotton sample was in the form of a bundle of six yarns, as shown on the left in Figure 3.1. A single yarn was obtained by untwisting the bundle and an array was made by closely aligning 30 single yarns together.

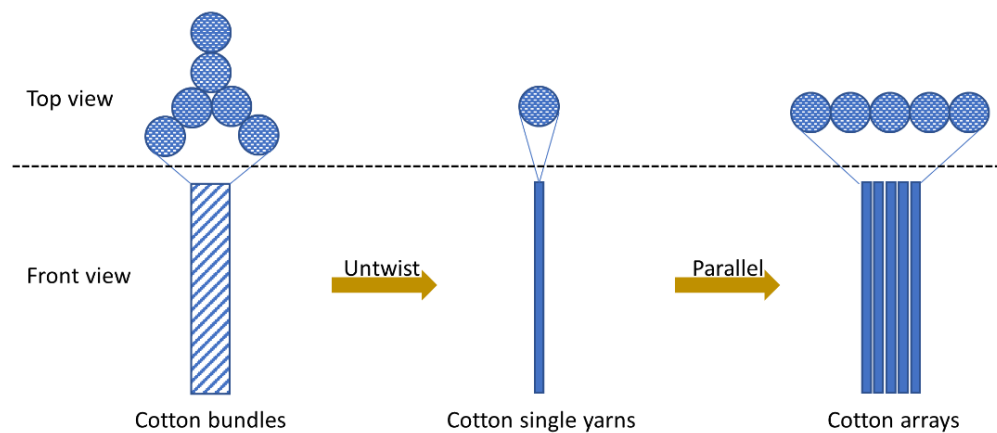


Figure 3.1 Three cotton sample arrangements studied in this chapter

For the dissolution process, see Figure 3.2, a Teflon picture frame was used on which the untwisted cotton yarns were wound by five separate loops, and the array was made by aligning 30 turns of single yarns next to each other on one side of the frame. After fixing all the yarns to the frame, the frame with samples was then submerged in a Teflon dish fully filled with about 50 mL of [C2mim][OAc]. The [C2mim][OAc] and the dish were preheated at the desired temperature in an oven for 50 min. The mass ratio of cotton sample to [C2mim][OAc] is about 1 to 40, where the [C2mim][OAc] was in excess[179]. The dissolution process was then implemented under different temperatures for different times in a vacuum oven (Shellab 17L Digital Vacuum Oven SQ-15VAC-16, Sheldon Manufacturing, Inc., USA) under vacuum. A coagulation process then followed with a water bath after the samples mounted on the frame were taken out from the [C2mim][OAc] bath. The coagulation process then further took place under a tap of running water for 24 hours to remove all the [C2mim][OAc], where very minor amount of solvent could run into the sink. After that, a drying process was applied to the samples at 120 °C for 1 hour under vacuum. For the bundles, the same dissolving procedure was applied as described above, but 5 turns of bundles were separately wound on a frame.

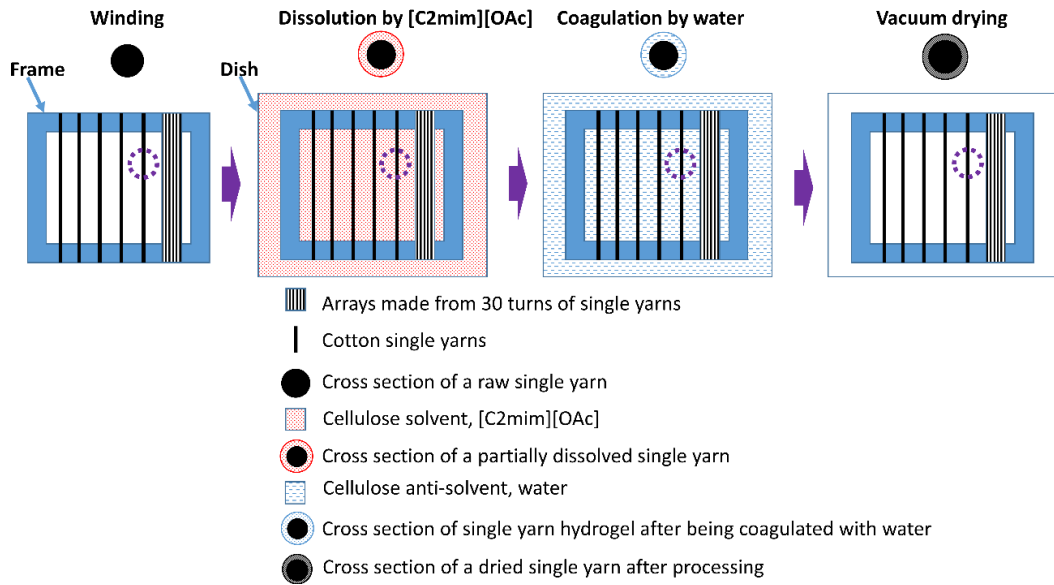


Figure 3.2 Process of dissolving cotton single yarns and arrays in [C2mim][OAc]

The samples are named as follows: processed samples were named CY-x-y, CB-x-y and CA-x-y, indicating a single cotton yarn, a cotton bundle and a cotton array processed at temperature 'x' (°C) for 'y' (hours) respectively.

3.2.2 Optical microscopy

Each set of three samples were embedded in the epoxy resin, using the method described in section 2.2.1, and observed under reflection mode in the optical microscope at room temperature. The areas of different sections of the processed samples were measured with the image processing software 'ImageJ 1.52d', including the total cross section area and the undissolved section in the core (blue portion), see Figure 3.3. For each sample, three different polishing surfaces were observed, which was used for the size measurement - calculate the average and standard error.

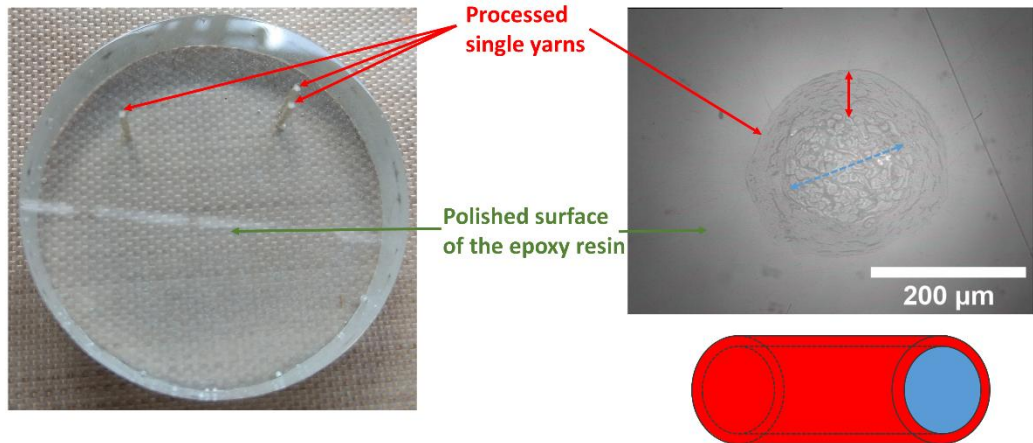


Figure 3.3 Polished epoxy resin, containing fibers ready to be photographed (Left) and a cross sectional image of a cotton single yarn (Right) with a scale bar indicating 200 microns. The fibre schematic highlights the areas of coagulated cellulose (Red) and the undissolved core (Blue)

An outer ring of dissolved and coagulated cellulose was clearly observed in all processed samples, which hereafter is named the coagulation fraction (CF). The CF obtained from the optical microscope images, CF_{OM} , is calculated by Equation 3.1:

$$CF_{OM} = A_{red} / (A_{red} + A_{blue}) \quad \text{Equation 3.1}$$

where A_{red} and A_{blue} represent the area of the coagulated material and the area of the central fibre as shown in Figure 3.3.

3.2.3 Wide-angle X-ray diffraction

The detail of the WAXD method can be found in section 2.2.2.

3.3 Results and discussion

3.3.1 Micromorphology of cotton single yarns and cotton bundles

The optical microscope images of cotton single yarns (CY) and cotton bundles (CB) processed under different temperatures and times are shown in Figure 3.4.

The original CY consists of a loose arrangement of many small filaments/microfibres, each with a diameter of ca. 13 μm , see Figure 3.4(a). As shown in Figure 3.4(b)-(g), after processing, CY became smaller in diameter. This could be because of the expansion of the fibre composed of non-bonded filaments in the original sample by the epoxy resin.

It is also depicted from the micrographs that the central fibre area was barely dissolved, suggesting that the processed CY can be treated as a composite which is comprised of a central core surrounded by a coagulated fraction.

Figure 3.4(h) shows that there are six single yarns in one cotton bundle and the dissolution happened not only at the perimeter of the samples, but also in the central area of the fibre bundles. This can be further confirmed by Figure 3.4(o), a magnified view of the circled area in Figure 3.4(l), where the arrows are pointing to the coagulated fraction in the interior between the individual fibres.

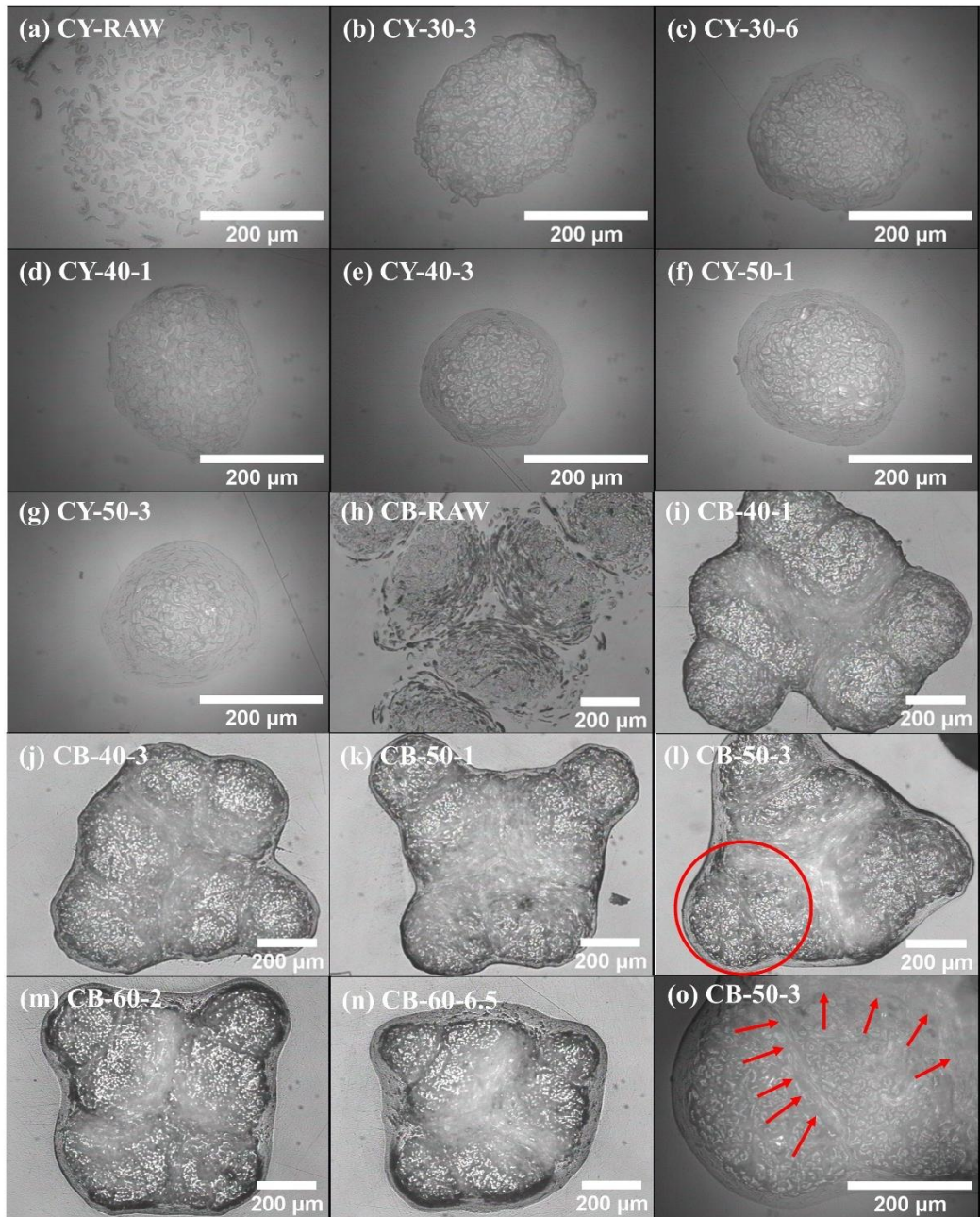


Figure 3.4 Optical microscope pictures of cotton single yarns (CY) from (a) to (g) and cotton bundles (CB) from (h) to (o) processed at different temperatures for different times with scale bars indicating 200 microns. Image (o) is a magnification of the area enclosed within the red circle in (l), in which the arrows point to the coagulated area

A ring-like coagulation fraction was observed in both CY and CB which was growing in size upon the increasing of temperature and/or time. But Equation 3.1 is only valid for CY samples to quantify the dissolution process via CFOM, but not for CB samples. This is because the interior of processed CY samples does not show any visibly dissolved cellulose, however the interior of the processed CB samples contains partially dissolved cellulose among different cotton yarns which form the bundles. For quantifying the dissolution of CB and CA samples, another method - WAXD - was used for determining the growth of the CF with temperature and time.

3.3.2 Analysis of dissolution of cotton single yarn in [C2mim][OAc] with TTS

Upon the dissolution of single yarns at different temperatures and times, CF was measured by OM (Figure 3.4) and calculated by Equation 3.1, of which the results are depicted in Figure 3.5(a).

With the increase of processing time and/or temperature, the CF increases, see Figure 3.5(a), which is consistent with the observation results from OM images in Figure 3.4. A time-temperature equivalence was suggested by the examination of the curves in Figure 3.5(a) that a master curve at each specific temperature could be created, as is routinely done in rheological analysis and was first proposed in our research group on the study of the dissolution of flax fibres in the same ionic liquid [125].

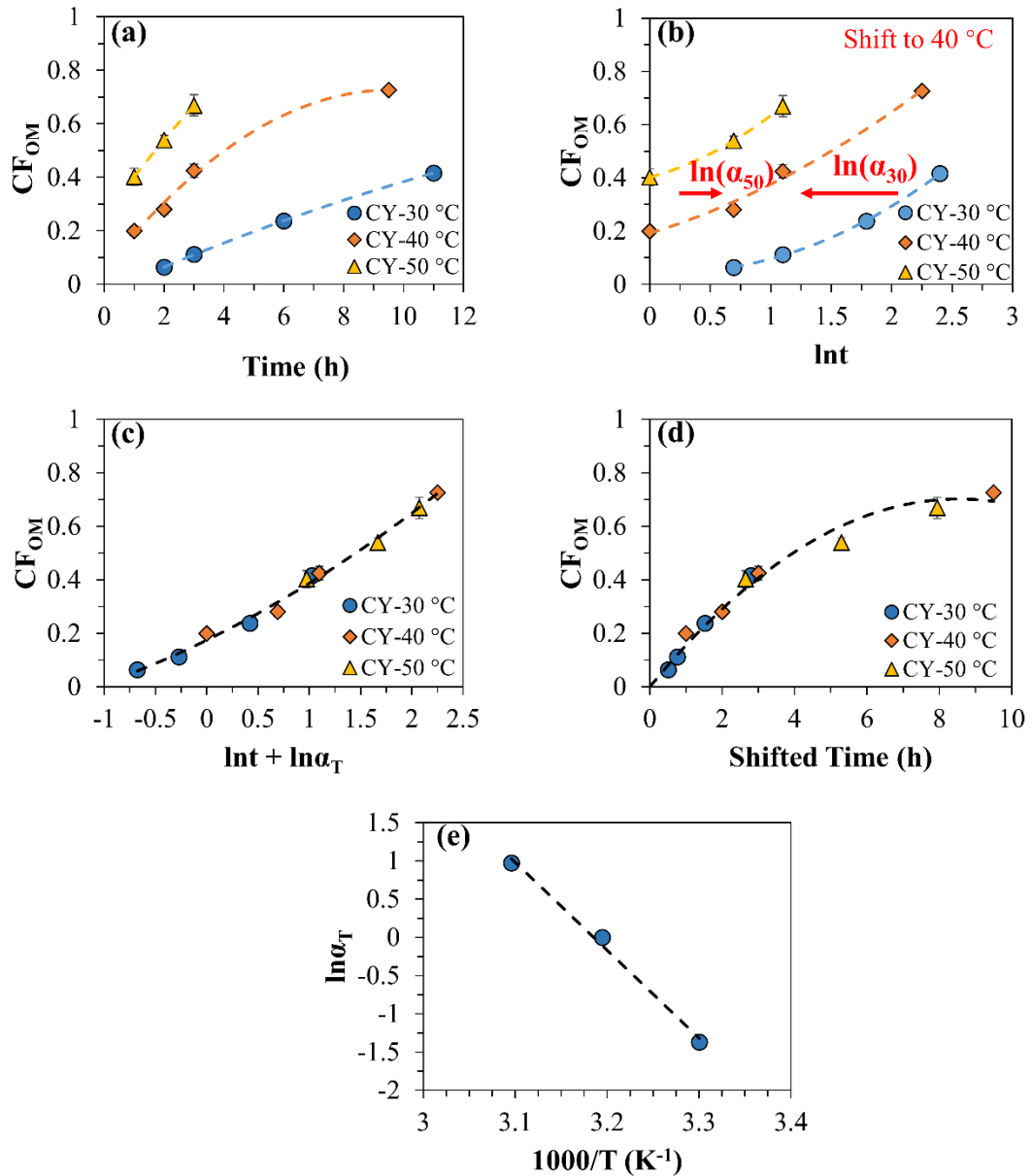


Figure 3.5 Coagulation fraction dependence of time for cotton single fibres (CY) on (a) linear time scale and (b) natural-logarithmic time scale; the time-temperature superposition plot after being shifted to 40 °C on both (c) natural-logarithmic time scale and (d) linear time scale; (e) Arrhenius plot with $\chi^2 > 0.99$. Some of the error bars are smaller than the symbols, and the dash lines in (a)-(d) provide guide for eye, and that in (e) is a fitting line

Here, a master curve at the specific reference temperature of 40 °C was obtained by the following steps: The data points attained at 40 °C were set to

be the reference dataset, where a shift factor equal to one was applied ($\alpha_{40} = 1$). In order to make the shifts of the other datasets of different temperatures easier to control, the x-axis is converted from normal time scale, t , to a natural logarithm time scale, $\ln t$, as it now consists of a horizontal shift only, see Figure 3.5(b). After that, the dataset of 40 °C was fitted with a preliminary polynomial function in order to provide a guide to the eye for further shifting. Then each other temperature dependant dataset was horizontally shifted, by a number equal to $\ln \alpha_T$, to the reference data/curve by eye after which all the data points were treated as an entirety and fitted with a final polynomial function. Finally, the χ^2 value, also known as the coefficient of determination ranging from 0 to 1, of the final fitting polynomial function was maximized by adjusting the shift factors α_T at 30 °C and 50 °C.

Table 3.1 Shift factors of different temperatures, obtained from the TTS analysis on cotton single yarns, used to plot Figure 3.5(e)

Temperature(°C)	α_T	$\ln \alpha_T$	Error in $\ln \alpha_T$
30	0.25	-1.37	0.01
40	1	0	-
50	2.65	0.97	0.01

The optimised master curve, in natural logarithmic time scale, fitted with a polynomial function (at 40 °C) is shown in Figure 3.5(c) and the one transformed back to linear time scale can be found in Figure 3.5(d). The formation of a convincing master curve from those isolated datasets proves the interchangeability/equivalence between time and temperature. The results

show that the dissolution speed is quite high in the beginning and then slows down as time progresses to a plateau.

Plotting the natural logarithmic shift factors versus the inverse temperature, results in a linear plot with a coefficient of determination χ^2 to be 0.99, see Figure 3.5(e) and Table 3.1, indicating that the dissolution dynamics follow an Arrhenius behaviour. This allows the activation energy for the process to be calculated using the natural logarithmic Arrhenius equation,

$$\ln \alpha_T = A + E_a/RT \quad \text{Equation 3.2}$$

Where E_a , A , R and T represent activation energy, Arrhenius pre-factor, gas constant and temperature, respectively. α_T represents the shift factor at temperature T .

The activation energy of the dissolution of the cotton single yarn in [C2mim][OAc] was calculated from the slope of Figure 3.5(e) to be 96 ± 8 kJ/mol, according to Equation 2.1. This value is very close to the flax dissolution activation energy of 98 ± 2 kJ/mol in [C2mim][OAc] reported by Hawkins et al[125]. It is worth noting that the dissolution activation energy is different from the reported rheological activation energies ranging from 46 kJ/mol to about 70 kJ/mol [121, 123, 180]. For the rheological activation energies, they were measured on the already-fully dissolved cellulose in its proper solvents, which does not include the decrystallization of cellulose. But the decrystallization process contributes to the dissolution activation energy. The speed of growth of the coagulation fraction was found to fall with the increase of time, see the master curve in Figure 3.5(d). This is hypothesized

as that the dissolution of cotton single yarn starts from its outer side, and the dissolved cellulose adheres to the undissolved core due to the locally high viscosity and the lack of mechanical turbulence such as stirring. With increasing time, the outer dissolved cellulose is thicker which results in a protective barrier between the undissolved core and the exterior solvent to slow down the dissolution speed.

3.3.3 Crystalline structure of cotton arrays and cotton bundles

As discussed in section 3.3.1, OM and Equation 3.1 are not suitable for quantifying the dissolution process of cotton arrays (CA) and cotton bundles (CB). Therefore, WAXD was used on both CA and CB to characterize their crystalline structure and the cellulose I fraction, with the method detailed in section 2.2.2. The raw cotton sample was found to be composed of only cellulose I and amorphous regions, with 65% and 35% area fraction ratio on the equatorial scan, respectively. The WAXD spectrum by equatorial scans were shown in Figure 3.6 which show that upon processing of both CA and CB, the height ratio of cellulose I peaks, especially the main reflection at 22.4° , to the amorphous peak at 18.2° was reduced and a conversion from cellulose I to cellulose II on crystalline structure is showed, seen most notably by the shifting of the main cellulose I peak of 22.4° to the dominant cellulose II peak of 20.2° [181, 182].

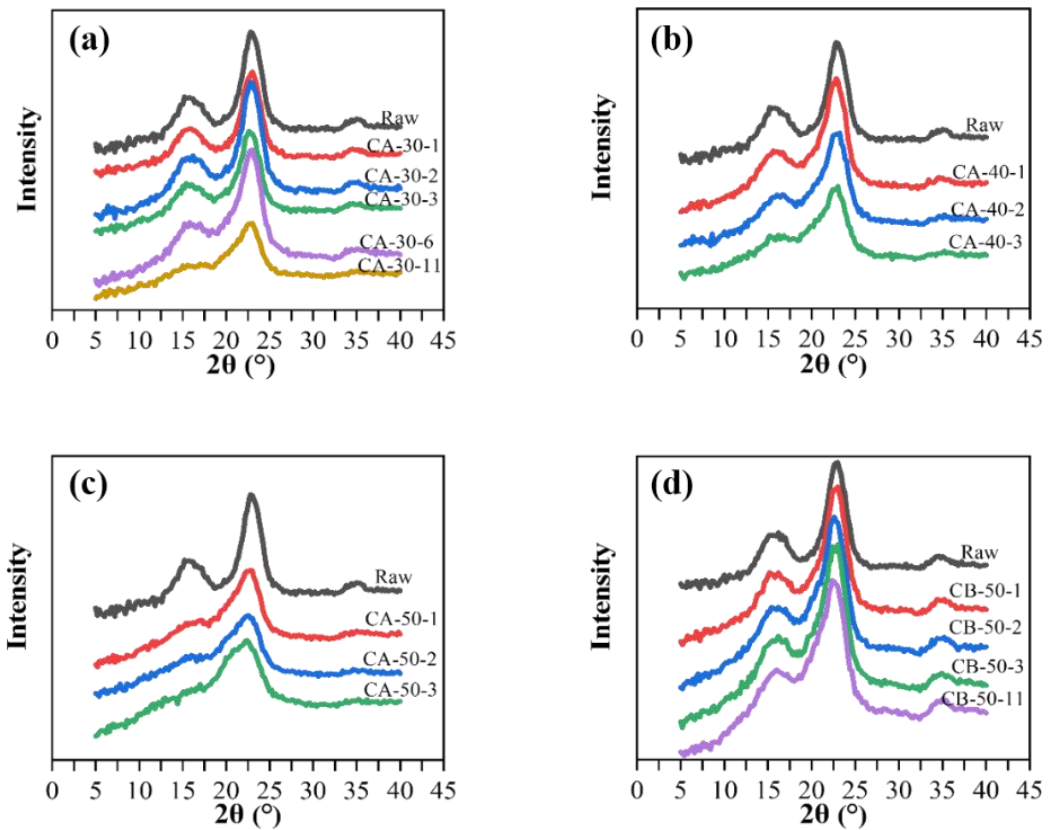


Figure 3.6 XRD spectra of cotton arrays (CA) processed at (a) 30 °C, (b) 40 °C and (c) 50 °C, and (d) cotton bundles (CB) processed at 50 °C for different times. The peaks appearing at around 20.2° and 21.8° are attributed to the cellulose II crystalline structure

By increasing both time and/or temperature a more significant crystalline structure conversion from cellulose I to cellulose II resulted. The WAXD spectrum of CA processed for various times at temperatures of 30 °C, 40 °C and 50 °C, are shown in Figure 3.6(a), (b) and (c), respectively. The relative size of the double peak at about 15° in 2θ , which is a convolution of the peaks at 14.8° and 16° belonging to cellulose I crystal without any notable cellulose II crystal peaks[181, 182], is used to indicate the amount of dissolution. At an elevated temperature, i.e. 50 °C, these two peaks were significantly lower,

suggesting that a dramatically increased speed of dissolution and a greater level of conversion from cellulose I to cellulose II.

By comparison between the graphs in Figure 3.6(c) and (d), the CB samples dissolve far more slowly - as is evident by the lack of change from a cellulose I to cellulose II signal. Even after 11 hours at 50 °C, the bundles still show a strong cellulose I peak at 22.4° and the two merged diffraction peaks at 14.8° (110) and 16.3° ($1\bar{1}0$)

3.3.4 Dissolution of cotton arrays and cotton bundles analysed with TTS

The coagulation fraction associated with the CA and CB was calculated using Equation 2.1 in conjunction with the cellulose I content from the deconvolution of WAXD data. Plots of the coagulation fraction for CA and CB against processing time at different temperature are shown in Figure 3.7 and Figure 3.8, respectively.

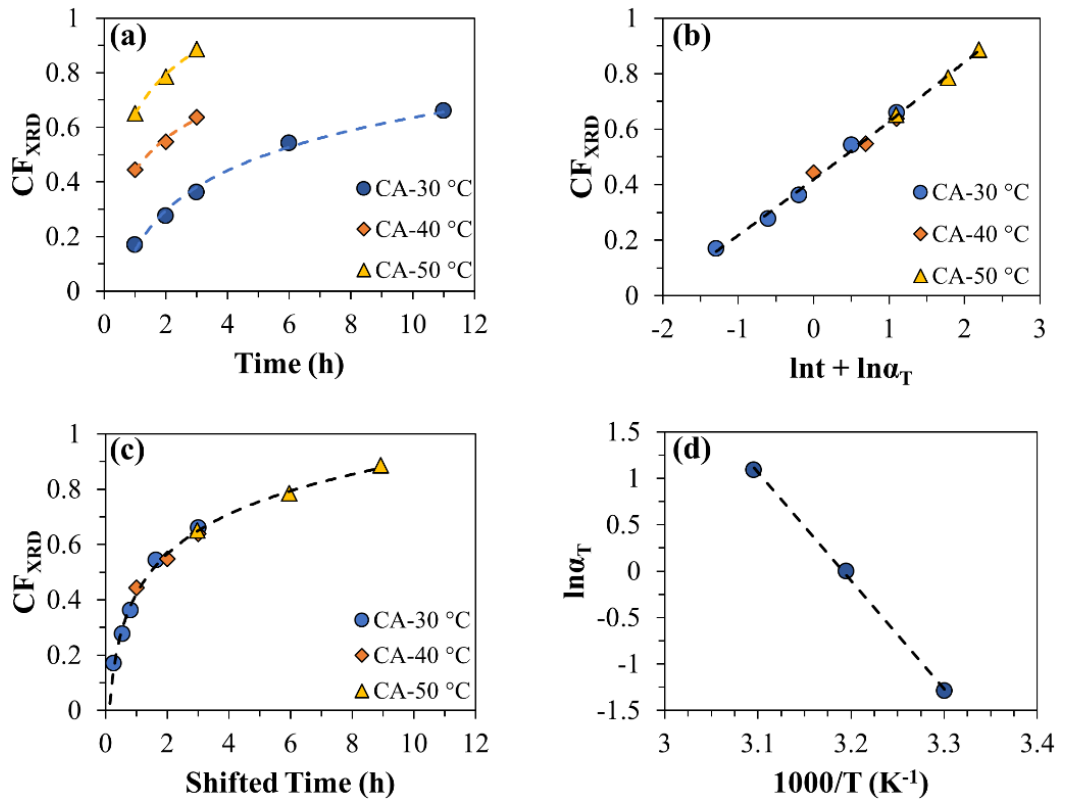


Figure 3.7 (a) Coagulation fraction as a function of dissolution time and temperature for cotton arrays (CA), the time-temperature superposition after being shifted to 40 °C on both natural-logarithmic time scale (b) and linear time scale (c); Arrhenius plot (d) with $\chi^2 > 0.99$. Some error bars are smaller than the symbols, and the dash lines in (a)-(c) provide guide for eye, and that in (d) is a fitting line

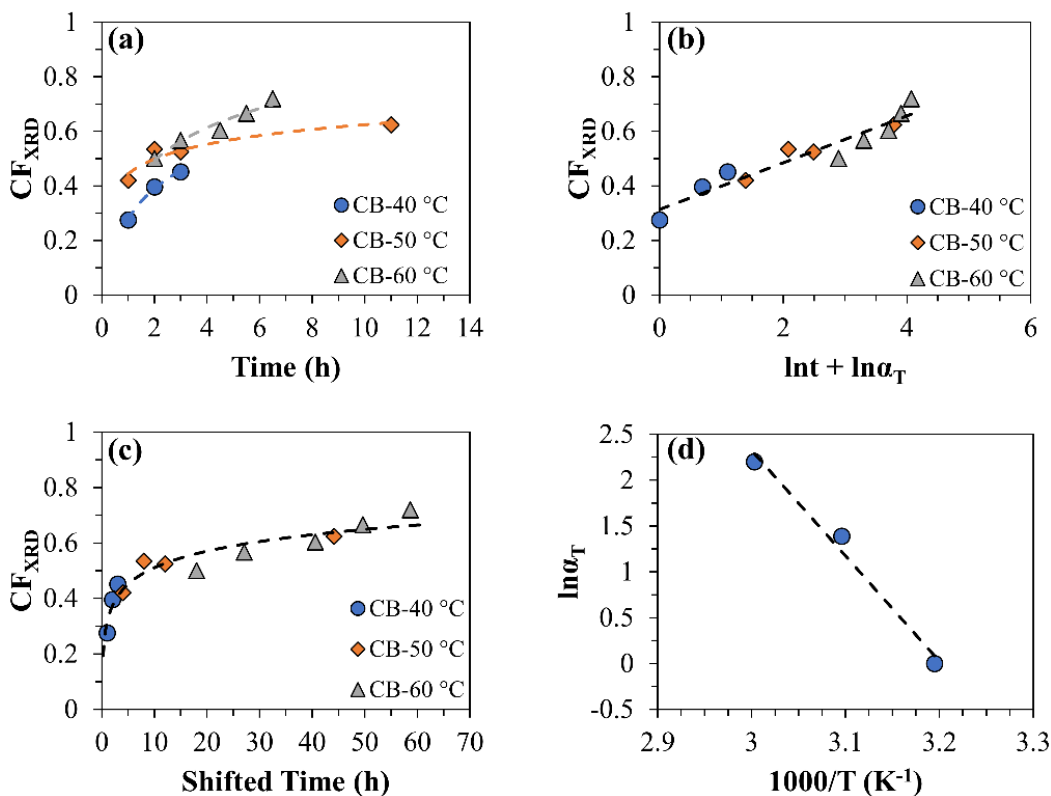


Figure 3.8 (a) Coagulation fraction as a function of dissolution time and temperature for cotton bundles (CB), the time-temperature superposition after being shifted to 40 °C on both natural-logrithmic time scale (b) and linear time scale (c); Arrhenius plot (d) with $\chi^2 > 0.97$. Some error bars are smaller than the symbols, and the dash lines in (a)-(c) provide guide for eye, and that in (d) is a fitting line

As shown in Figure 3.7(a) and Figure 3.8(a), the CF_{XRD} of both CA and CB became greater with processing time progressing and/or the temperature increased, and a similar time-temperature equivalence, as for the CY, is found. Compared with CB, CA dissolved faster with increasing temperature, as evident by a higher coagulation fraction while increasing by the same amount with temperature but with the same dissolution time. These results are consistent with the qualitative results from the WAXD spectrum in Figure 3.6 that increasing dissolution time and/or temperature more crystalline

transformation from cellulose I to cellulose II can be observed. This transformation of CA is more obvious and faster than that of CB samples.

In order to obtain a master curve for the CA and CB, the same TTS procedure as the one used for CY samples outlined in section 3.3.2 was also applied to the CF_{XRD} datasets and the shift factors are summarized in Table 3.2. The master curves at 40 °C for CA and CB were shown in Figure 3.7(c) and Figure 3.8(c), respectively. A similar phenomenon on CY was also observed on CA and CB that the CF_{XRD} increased dramatically in the beginning of dissolution and slowed down as the dissolution progresses then reached a plateau.

Table 3.2 Shift factors of different temperatures, obtained from the TTS analysis on cotton arrays and cotton bundles, used to plot Figure 3.7(d) and Figure 3.8(d) respectively

Sample	Temperature(°C)	α_T	$\ln \alpha_T$	Error in $\ln \alpha_T$
cotton arrays	30	0.28	-1.29	0.01
	40	1	0	-
	50	2.97	1.09	0.01
cotton bundles	40	1	0	-
	50	3.67	1.30	0.02
	60	8.17	2.11	0.02

Arrhenius plots were again applied to both CA and CB with χ^2 of larger than 0.99 and 0.97 respectively. According to Equation 3.2, the corresponding activation energies are calculated, from the slopes in Figure 3.7(d) and Figure 3.8(d), to be 97 ± 3 kJ/mol (CA) and 91 ± 11 kJ/mol (CB) respectively, which

are very similar to the value determined from the single cotton fibres of 96 ± 8 kJ/mol.

3.3.5 Analysis of the effect of sample arrangement on the dissolution behaviour

The activation energy as a function of sample arrangement (CY, CA and CB) and a time-temperature superposition plot containing data from all sample types were plotted in Figure 3.9 and Figure 3.10 respectively, so as to analyse the effect of sample arrangement on the dissolution behaviour.

Depicted in Figure 3.9, the activation energies of three cotton samples are very similar, giving an average value of 96 ± 3 kJ/mol. This result interestingly suggests that there is no influence of cotton sample arrangement on the dissolution activation energy when the errors are taken into consideration, even though the speed of dissolution depends on the fibre arrangement.

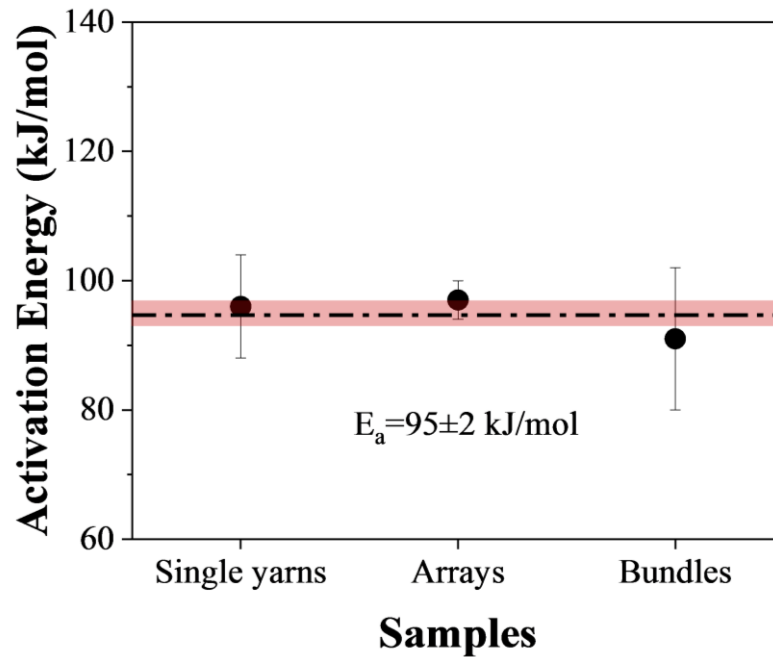


Figure 3.9 Comparison of activation energies for cotton single fibers, arrays and bundles. the dot-dashed line indicates position of the average value and the rectangular shape indicates the error margin. For the array, the error bar is smaller than the size of symbol used

In Figure 3.10, the effect of arrangement on the dissolving speed is compared and analysed, where the three master curves at 40 °C of different cotton samples were combined into one plot. To recap, two techniques, optical microscopy for CY and wide-angle X-ray diffraction for the CA and CB, were used to determine the growth of coagulation fraction with time and temperature via Equation 3.1 and Equation 2.1, respectively. The dissolving speed of CY is quite similar to that of CA, even though different experimental methods were used to obtain the datasets.

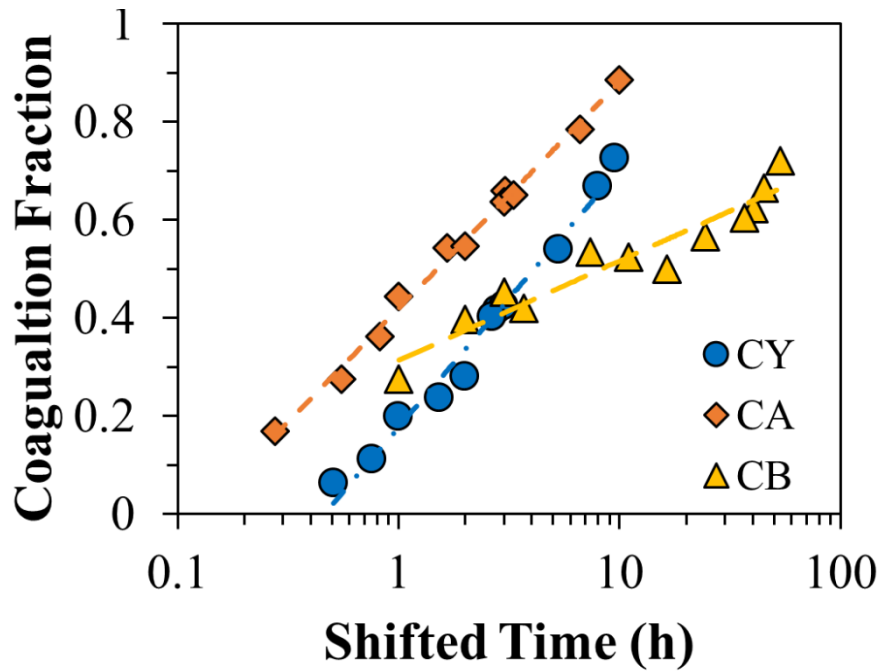


Figure 3.10 Comparison of time-temperature superposition after being shifted to 40 °C among cotton single yarns (CY), cotton arrays (CA) and cotton bundles (CB). The dash lines provide guide for eye, and some error bars are smaller than the symbols

It is shown, in Figure 3.10, that the CB dissolved more slowly than the other two cotton samples, CY and CA. It can be proposed that the cotton yarns composing the CB are loosely twisted giving more space for [C2mim][OAc]. While the interior of the CB is full of dissolved cellulose, [C2mim][OAc] can barely get access to the inner surface of the bundles but only the outer surface, bringing a slower increase in CF. The dissolution speed among three arrangements is ranked as: $CY \approx CA > CB$, indicating that cotton samples arrangement dominates the dissolution rate of cotton samples with excess [C2mim][OAc]. These findings could be used for future studies on the other cellulose fibres and cellulose fibre based all cellulose composites.

3.4 Conclusions

In this chapter, the dissolution of natural cotton in [C2mim][OAc] and the effect of sample arrangement (CY, CA and CB) on the dissolution are studied with time-temperature superposition. Two experimental techniques-optical microscopy and wide-angle X-ray diffraction - are used to characterize the dissolution progress of the cotton samples upon processing at different temperatures and times. The amount of dissolution was quantified by calculating the coagulation fraction from either optical microscope images of processed CY cross section, or WAXD deconvolution by which the cellulose I area fraction was obtained. The growth of coagulation fraction was found to follow time-temperature superposition, giving master curves at 40 °C and an Arrhenius behaviour was found for the shift factors, α_T . The changes on morphology of CY and CB are observed via an optical microscope, where the dissolution starts from exterior, resulting in a layer of coagulated cellulose surrounding the undissolved fraction on CY samples and the thickness of coagulated layer increased with either processing time or temperature increased. While, for the CB the dissolution happens not only from the exterior of the samples, but also from the interior, due to the loose twisting of the six cotton yarns, leading to the quantifying method expressed with Equation 3.1 not applicable for CA and CB. As a result, the nature that the crystalline transformation from cellulose I to cellulose II is irreversible and so is used to quantify the dissolution of CA and CB via Equation 2.1. WAXD results show that there are only cellulose I and amorphous regions in the raw sample, and upon dissolution, cellulose I is transformed to cellulose II and amorphous indicating that the coagulated layer on CY is composed of cellulose II and

amorphous. This transformation is seen to be more significant on CA than CB with the same amount of processing time increased and at the same dissolving temperature. In other words, CA dissolves with a higher speed than CB.

The kinetics of cellulose dissolution is quantified by an activation energy calculated from the slope of Arrhenius plot via Equation 3.2. Activation energies of CY, CA and CB are found to be 96 ± 8 kJ/mol, 97 ± 3 kJ/mol and 91 ± 11 kJ/mol, respectively, giving an average value of 95 ± 2 kJ/mol. This result implies the independence of cotton sample arrangement on the dissolution activation energy. By contrary, the arrangement dominates the dissolving rate dramatically with a ranking of $CY \approx CA > CB$.

Chapter 4 Dissolution of mercerized cotton cellulose in [C2mim][OAc]

4.1 Introduction

The dissolution behaviour of cellulose of natural cotton, containing only cellulose I and amorphous cellulose and a collection of smaller molecules, in [C2mim][OAc] has been successfully analysed with TTS in Chapter 3. This chapter investigates the dissolution behaviour of mercerized cotton in [C2mim][OAc], with a different composition of allomorphs, which to the best of our knowledge, has not been previously studied with TTS. The work in this chapter is an expanded version of that already published in paper III.

Mercerization is an industrial process often used for cotton fibres and named after John Mercer, in the 1850's, who was granted with a patent in which a concentrated sodium hydroxide solution was used to treat the natural cotton textiles [23, 183]. The best advantage of his invention is to increase the adhesion of dyestuffs on cotton textiles, while the disadvantage is a shrinkage of up to 18%, leading to a thickening in fibre diameter. Lowe, in 1889, discovered a method to overcome the shrinkage by carrying out the mercerization process under tension, which finally made it a commercial success as seen today [23, 184, 185].

The modification degree can be effected by the concentration of alkali, length of treatment and processing temperature [186]. In the aspect of the changes in chemical properties upon the process, the cellulose crystallinity of a cotton sample was decreased from 81.2% to 66.5%, reported by Yue et al [187]. The

cellulose molecules rearranged to a more compact pattern – cellulose II which is more thermally stable than cellulose I existing in natural cotton [188], see Figure 4.1. It can often lead to a decrease in molecular weight [184] and extensive fibrillation, which is breaking down the fibre bundles into shorter and smaller fibres by releasing lignin and hemicellulose [186].

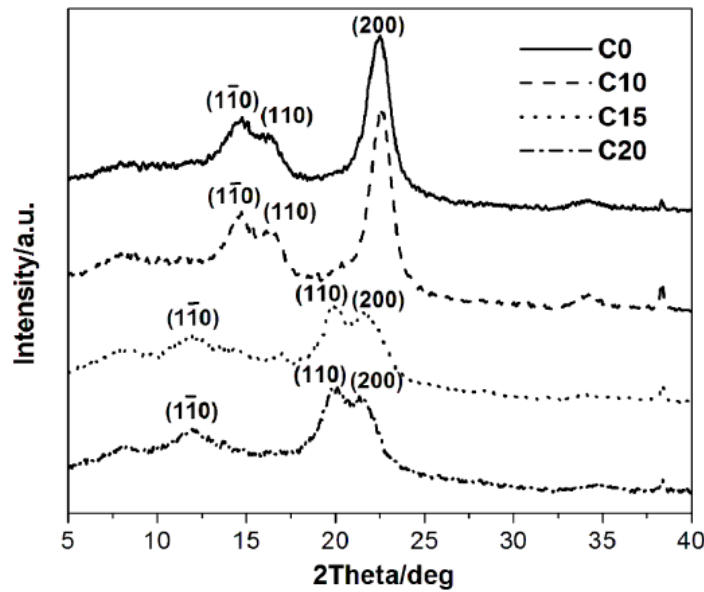


Figure 4.1 XRD spectra of natural cotton (C0) and mercerized cotton, where C10, C15 and C20 represent the concentrations, 10 wt%, 15 wt% and 20 wt%, of sodium hydroxide solution used for mercerization, respectively. Reported by Yue et al. [187]

In terms of physical changes, the process results in a greater strength and lustre of the mercerized cellulose samples and also a greater capacity to absorb dye [187, 189, 190], shown in Figure 4.2. The shape of natural cotton fibres is ribbon-like, exhibiting flat and twisted structure with a distorted cross section of crushed lumens, see Figure 4.2(a). But as the mercerization process progresses, the twisted structure gradually disappears and the cross section becomes rounder with the hollow structure shrinking and disappearing, shown in Figure 4.2(b)-(d) [190].

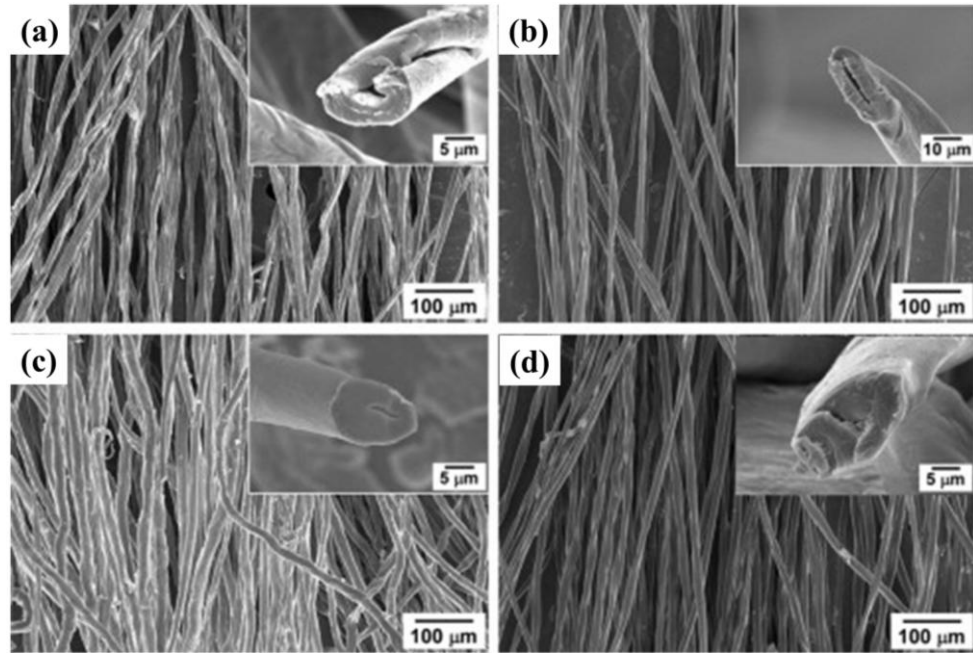


Figure 4.2 SEM images of (a) natural cotton fibres and mercerized cotton treated with 15 wt% sodium hydroxide solution at room temperature for (b) 10, (c) 40, (d) 60 min with a zoom-in picture showing the cross-section at the top-right corner at each picture. Credit: Yu et al. [190]

Due to the huge benefits brought by mercerization, mercerized cotton is a very important cellulose material widely used in garment industry and has huge potential as a cellulose source in the fabrication of all cellulose composites from its virgin and potentially recycled textiles. The work presented in this chapter follows on from the content in Chapter 3, but focuses on the mercerized cotton and the effect of different dissolution, quantifying methods on the dissolution activation energy. The dissolution behaviour of a mercerized cotton yarn in the ionic liquid, [C2mim][OAc], is investigated, upon processing with different combinations of temperature and time. The partially dissolved cellulose is coagulated with the anti-solvent - water, forming a cellulose network filled and swollen by water in the pores, for the sake of simplicity, called hydrogels, then followed by a drying process. Optical

microscopy (OM) and wide-angle X-ray diffraction (WAXD) are used to characterize the changes in morphology and crystalline structure caused by different processing temperatures and/or times. The dissolution progress is quantified on both hydrogels and their dried samples with different quantifying methods based on the results from OM and WAXD. It is hypothesized that the activation energy is independent of the quantifying method. Meanwhile, a novel and straightforward technique to measure the water content (volume fraction) in hydrogels is also proposed and compared to the weighing-mass method already widely reported by others [191, 192]. The main findings in this chapter, i.e. the dissolution master curve and dissolution activation energy, will provide important information for fabricating all cellulose composites in a later chapter.

4.2 Methods

4.2.1 The procedure of dissolving the mercerized cotton yarns with [C2mim][OAc]

Notably, the mercerized cotton yarns (MCY) mentioned in this chapter are used as received, instead of being mercerized by ourselves. In order to investigate its dissolution behaviour, a method similar to the one for natural cotton yarns detailed in section 3.2.1 is used. To begin, the yarn was wound on one side of a Teflon frame into five separate loops; and then an array consisting of 30 loops aligning closely to each other was wound on the other side, see Figure 4.3. After that the samples and the frame were soaked in ca. 50 mL of [C2mim][OAc] contained in a Teflon dish, with a mass ratio of cotton sample to [C2mim][OAc] to be 1 to 40 where the [C2mim][OAc] is in an excess

amount [179]. The [C2mim][OAc] bath had been preheated at the designated temperature for 50 min before the samples were put into it. The dissolution was conducted at different temperatures for a period of time, after which the samples were taken out from the [C2mim][OAc] bath to a coagulation process – a water bath. To get rid of any residual [C2mim][OAc] in the samples, the coagulation process continued under a tap of running water for 24 hours. After that, hydrogels/swollen samples were attained and kept in a water bath for further examination. A drying process then followed, with a vacuum oven at 120 °C for 1 hour, to get dried samples. It is noteworthy that all the samples were kept on the frame all the time until the final drying process finished, resulting in a constant sample length upon the drying process.

The processed samples are nomenclated as follows: MCYH-x-y, DMCY-x-y and DMCA-x-y indicating a mercerized cotton yarn hydrogel, a dried mercerized cotton yarn and a dried mercerized cotton array respectively, dissolved at temperature 'x' (°C) for 'y' (hours).

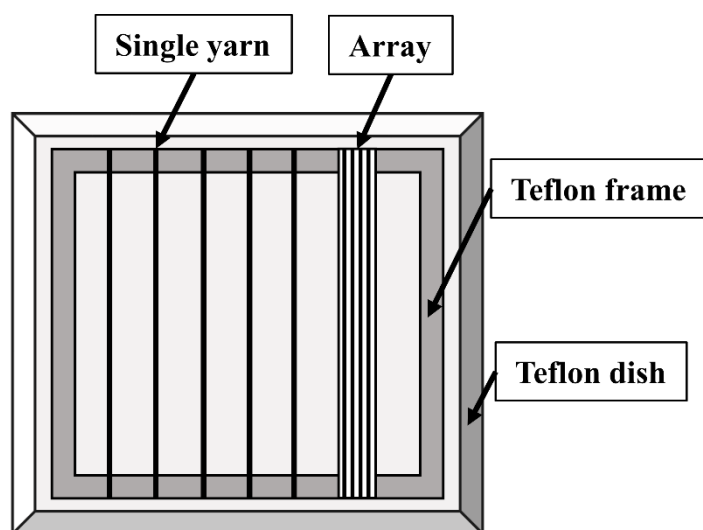


Figure 4.3 Apparatus for dissolving mercerized cotton yarns and arrays

4.2.2 Optical microscopy

The morphology of processed samples, transverse view for MCYH and cross section for DMCY, is investigated with the optical microscope. For the DMCY, each set of three samples were embedded in the epoxy resin, using the method detailed in section 2.2.1, and their cross sections were examined under reflection mode with the optical microscope. As to the MCYH, it is difficult to observe its cross section, instead the transverse view is observed under light transmission mode. The MCYH mounted on the Teflon frame was submerged in a water bath during observation, to stop water evaporating from the hydrogel samples, see Figure 4.4. All the microscopic observations were conducted at room temperature with a relative humidity of ca. 50 %. For each DMCY sample, three different polishing surfaces were observed to calculate the average value and standard error. As to the MCYH, 15 different places were measured on each sample, and the average value and standard error were then calculated. The size measurement was conducted with the image processing software 'ImageJ 1.52d'.

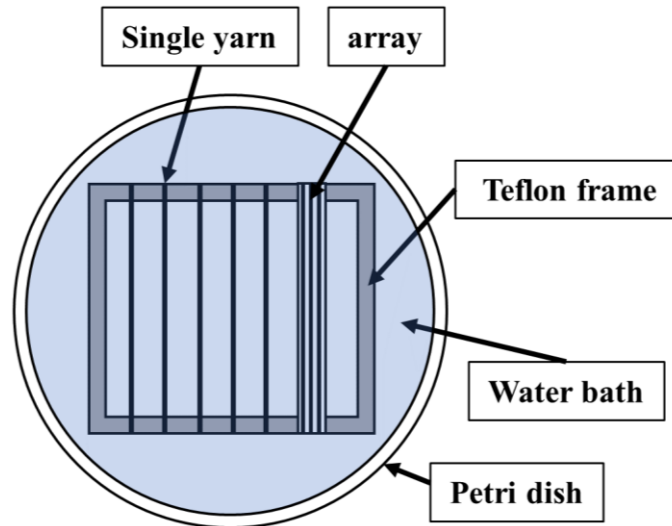


Figure 4.4 Schematic graph of hydrogels/swollen samples soaking in a water bath for optical-microscopic observation of their transverse view

4.2.3 Wide-angle X-ray diffraction

In order to investigate the effect of dissolution condition on the crystalline structure, WAXD is implemented to the DMCA samples. The detail of WAXD method can be found in section 2.2.2.

4.2.4 Quantification of dissolution

In this chapter the dissolution progress of the mercerized cotton is quantified with two indexes, the coagulation fraction (CF) and the radial length of the outer coagulated cellulose ring, and for simplicity the latter is hereafter called ring thickness. The qualification is applied on both dried and swollen/hydrogel samples according to the results from either OM or WAXD.

For dried samples, CF obtained from both OM and WAXD, CF_{OM} and CF_{XRD} , were measured according to the methods detailed in section 3.2.2 and section 2.2.1, respectively. They are used to verify the universality of our TTS analysis

method - not only suitable for the natural cotton samples, but also feasible on the mercerized cotton samples – and their TTS analysis results work as references when analysing the dissolution progress associated with MCYH samples.

As mentioned in section 4.2.2, it is difficult to observe the cross section of MCYH via OM, therefore the sizes of MCYH are measured from its transverse view image, see Figure 4.5(a). Two other quantifying methods – measuring the coagulation fraction (CF_{OM-H}) and ring thickness of MCYH (T_H) - are introduced, using the size measurement results of MCYH. The CF_{OM-H} is calculated with Equation 4.1:

$$CF_{OM-H} = \frac{\pi(0.5a_H)^2 - \pi(0.5b_H)^2}{\pi(0.5a_H)^2} \quad \text{Equation 4.1}$$

Where a_H and b_H represent the outer diameter of the hydrogel sample and the diameter of the undissolved/central region in the hydrogel sample, respectively. They are indicated with the green double-arrow line for (a_H) and orange double arrow line for (b_H) in Figure 4.5(a).

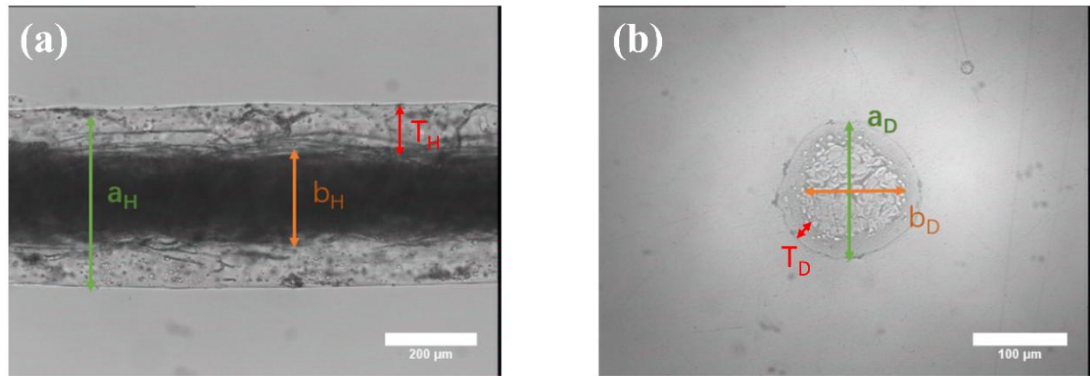


Figure 4.5 Optical microscopy images of (a) the transverse view of a mercerized cotton yarn hydrogel soaking in a water bath and (b) the cross section of the dried mercerized cotton yarn, in which the undissolved section, the total sample and the outer ring are indicated in orange (b_H and b_D), green (a_H and a_D) and red (T_H and T_D) double-arrow lines, respectively

The ring thickness of MCYH, T_H , shown with the red double-arrow line in Figure 4.5(a), is calculated via Equation 4.2:

$$T_H = \frac{a_H - b_H}{2} \quad \text{Equation 4.2}$$

The growth of the amount of coagulated cellulose is quantified with different parameters, CF_{OM} and CF_{XRD} for DMCY samples, CF_{OM-H} and T_H for MCYH samples, allowing the dissolution activation energies to be determined from the time-temperature analysis. The results from comparing these activation energies can be used to verify the fact that any parameter, which can be tracked as a function of time and temperature, can be used to examine whether TTS holds and calculate an activation energy. It is proposed that the

methods applied on mercerized cotton hydrogel are faster than those on dried samples, because the time spent on the drying process is saved.

4.2.5 Water volume fraction and swelling ratio

For cellulose hydrogels/swollen cellulose samples, the most commonly used method of measuring their water contents is the weight loss technique [191, 192]. It directly measures the change in sample mass during immersion followed by a drying process, whereby the water left on the surface of the sample needs to be removed by being patted with an absorbent material such as tissue paper. However, there is not a criterion to quantify the dryness – how many times the samples should be patted with tissue paper – which reduces the measurement accuracy. Further, the diameter of our cotton yarn is very small, around 160 μm , resulting a high difficulty to control the dryness.

Hence, we introduce water volume fraction, ϕ_{water} , to quantify the amount of water in MCYH samples, using the changes in water volume, V_{H_2O} . The water volume fraction is expressed by Equation 4.3:

$$\phi_{water} = \frac{V_{H_2O}}{V_{swollen}} = \frac{V_{swollen} - V_{dry}}{V_{swollen}} \quad \text{Equation 4.3}$$

$$V_{swollen} = A_{swollen} \times L_{swollen} \quad \text{Equation 4.4}$$

$$V_{dry} = A_{dry} \times L_{dry} \quad \text{Equation 4.5}$$

where $V_{swollen}$ and V_{dry} represent the volumes of MCYH sample and DMCY sample, respectively. In Equation 4.4 and Equation 4.5, $L_{swollen}$ and L_{dry}

mean the lengths of MCYH sample and DMCY sample respectively, and $A_{swollen}$ and A_{dry} are the relevant cross areas, either the coagulated/outer ring or the undissolved/central core, of MCYH and DMCY, respectively. Because the sample length was constant during the drying process, therefore Equation 4.3 can be rearranged to be:

$$\phi_{water} = \frac{A_{swollen} - A_{dry}}{A_{swollen}} \quad \text{Equation 4.6}$$

It should be noted that, $A_{swollen}$ is calculated from the diameter, either a_H or b_H , with the formula for area of circle, while A_{dry} can be measured from OM images.

The changes in radial length of the outer ring and central core, labelled with red double-arrow lines and orange double-arrow lines respectively in Figure 4.5, are used to calculate their swelling ratios. For the outer ring, its swelling ratio, R_{ring} , is expressed with Equation 4.7:

$$R_{ring} = \frac{a_H - b_H}{a_D - b_D} \quad \text{Equation 4.7}$$

where a_D and b_D measure the diameter of the whole sample and that of the undissolved/central region of DMCY, see Figure 4.5(b).

So as to determine the swelling extent in the radial direction of the undissolved central core, its swelling ratio, R_{core} , is calculated by

$$R_{core} = \frac{b_H}{b_D} \quad \text{Equation 4.8}$$

Because the samples were being kept on frames during the drying process, it is assumed that there was no shrinking in the axial direction, which is quite similar to the industrial measures to eliminate sample axial shrinking during the mercerization process, where a tension is usually applied to constraint sample length [185, 193]. According to the definition of swelling ratio in this thesis, the higher the value is, the less the sample is retained/the more the swelling is.

4.3 Results and discussion

The dissolution of the mercerized cotton samples in [C2mim][OAc] is explored with OM and WAXD of which the results will be presented and discussed in this section. Before starting the analysis, for the purpose of convenience, the dissolution process introduced in this chapter and how the qualification parameters are measured are schematically shown in Figure 4.6.

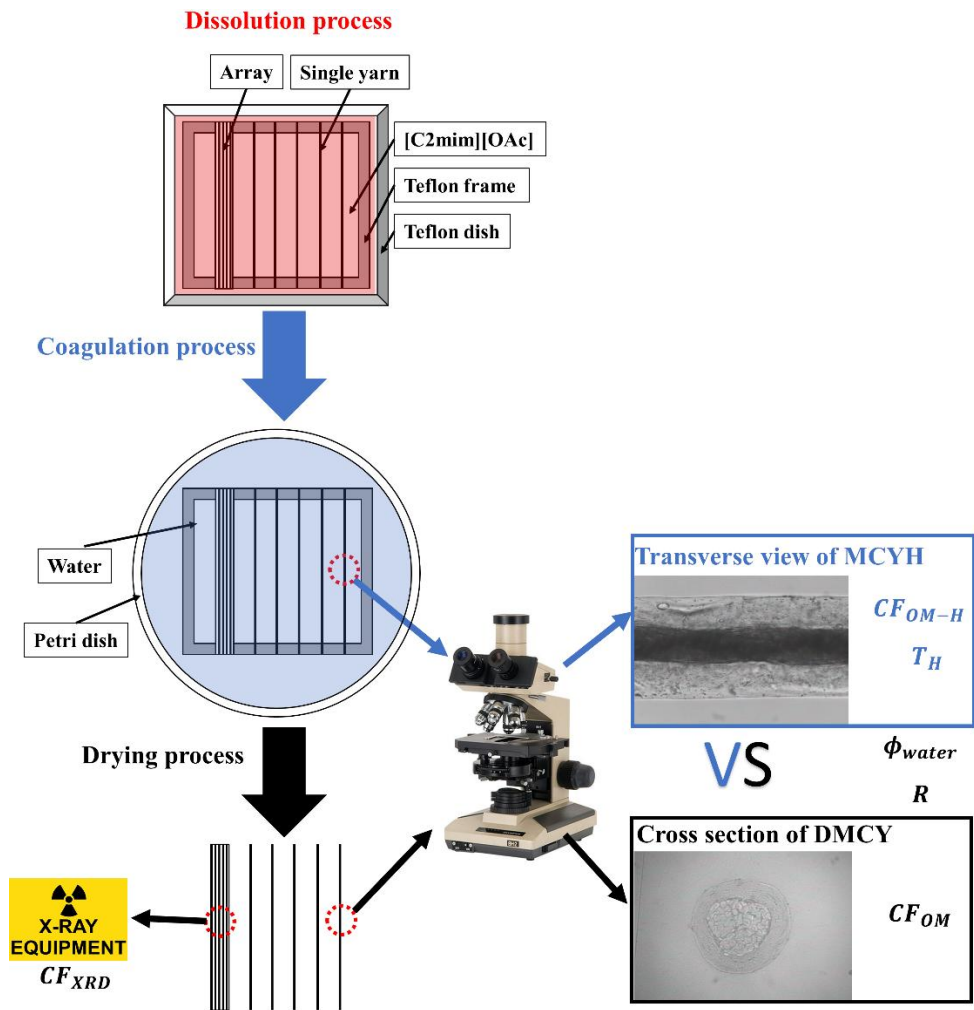


Figure 4.6 Schematic graph explaining the measurements and qualification of the dissolution process, connecting parameters with techniques and samples, where for the mercerized cotton yarn hydrogel (MCYH) CF_{OM-H} and T_H mean its coagulation fraction and ring thickness from optical microscopy, respectively; and for the dried samples (dried mercerized cotton yarn (DMCY) and arrays) CF_{OM} and CF_{XRD} represent the coagulation fractions calculated from the results of optical microscopy and wide-angle X-ray diffraction, respectively

4.3.1 Micromorphology

The processed MCYH and DMCY were observed with an optical microscope, and the transverse view images of MCYH and the cross-section images of DMCY are shown in Figure 4.7.

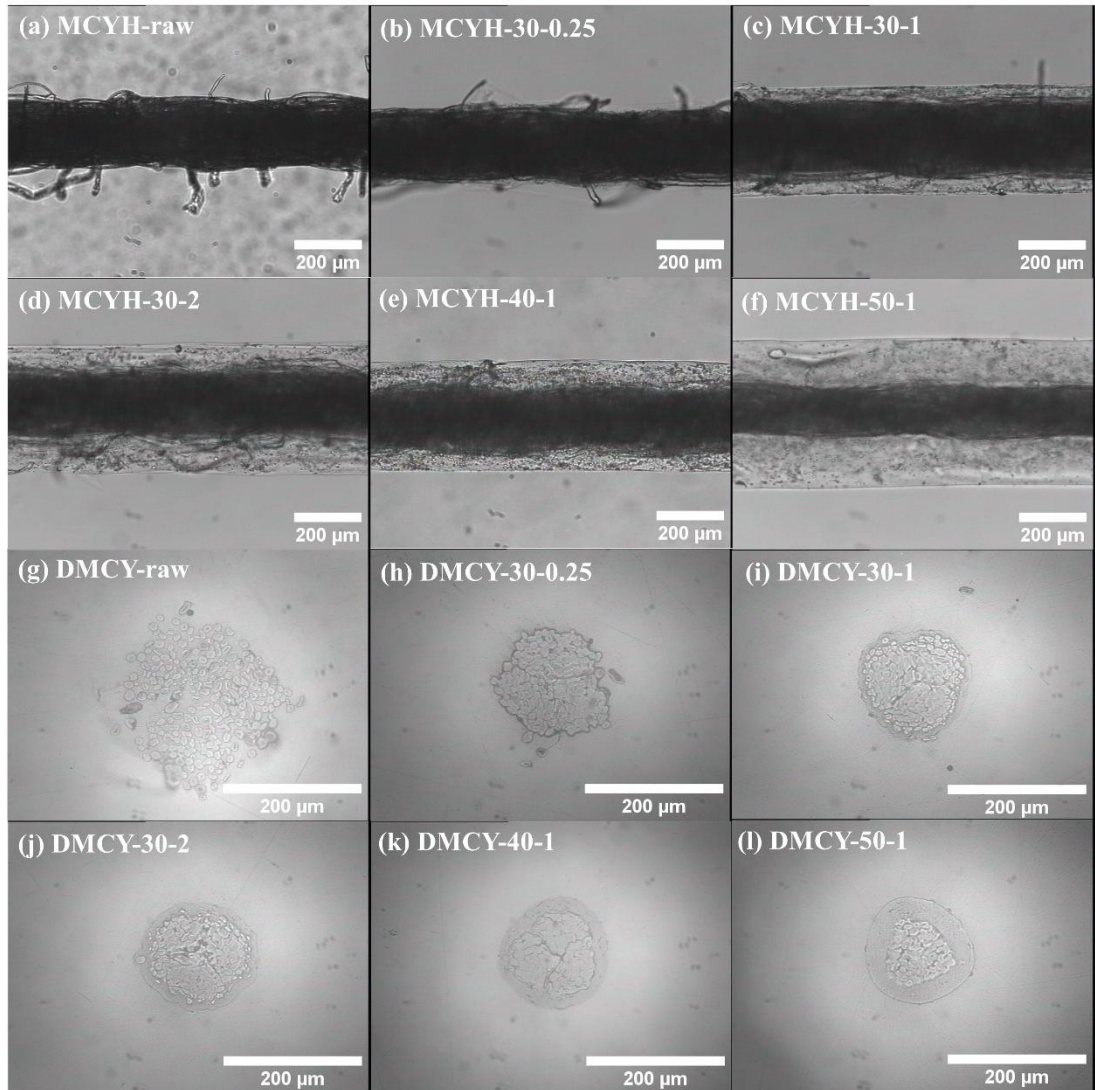


Figure 4.7 Optical-microscopic transverse-view images of (a) the raw mercerized cotton yarn after soaking in water for 24 hours and (b)-(f) the mercerized cotton yarn hydrogels (MCYH); cross-section images of (g) the raw mercerized cotton yarn and (h)-(l) the dried mercerized cotton yarn (DMCY), and look to section 4.2.1 for nomenclature in detail

As shown in Figure 4.7(b)-(f), there are ring-like coagulated regions in the MCYH samples, presenting a lighter colour and covering the black central/undissolved regions. The size of outer ring increased upon the processing temperature and/or time increasing, and no visible dissolved cellulose was found in the central region, indicating that the dissolution starts from the exterior of the mercerized cotton yarn and moves into the central yarn. As mentioned for the natural cotton yarns in section 3.3.2, our hypothesis is recalled: once the dissolution starts, the dissolved cellulose acts as a protective layer to the central region. The outer ring was found thicker in the MCYH sample processed at higher temperature than that processed at lower temperature, when both were processed for the same amount of time, e.g. MCYH-30-1 and MCYH-50-1 shown in Figure 4.7(c) and (f) respectively. This suggests that the higher the temperature is, the faster the mercerized cotton sample dissolves.

Compared with MCYH samples, the DMCY samples showed a similar dissolution behaviour that the coagulated region grew as either the processing temperature or time increased, see Figure 4.7(h)-(i). Due to the swelling effect of water, the outer ring in MCYH is thicker than that in its DMCY sample, upon the same processing condition, allowing the growth of the outer ring to be followed more easily with the increase of temperature and time. Additionally, shown in Figure 4.7(g), the raw mercerized cotton yarn consists of a bunch of micro-filaments with an average diameter of about 8.3 μm and they were swollen by the epoxy resin. Notably, the OM result of DMCY is very similar to that of natural cotton yarns.

4.3.2 Analysis of mercerized cotton array crystalline structure

To follow the change in crystalline structure during the dissolution process, and to again determine the coagulation fraction, WAXD was used on the DMCA (dried mercerized cotton array) samples. The WAXD spectra from equatorial line scans are shown in Figure 4.8.

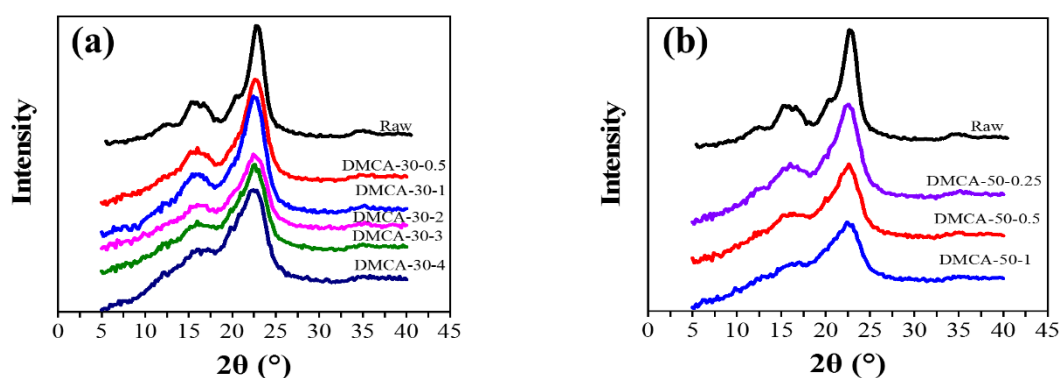


Figure 4.8 WAXD spectra of dried mercerized cotton arrays (DMCA) processed at (a) 30 °C and (b) 50 °C for different times, which are shifted vertically for clarity, look to section 4.2.1 for nomenclature in detail

The cellulose I, cellulose II and amorphous area fractions from equatorial line scans of the raw sample were found to be 40.7 %, 19.7 % and 39.6%, respectively. It is noteworthy that they are not the absolute contents of crystallinity, and more detail with explanations has been given in section 2.2.1. A similar phenomenon to the natural cotton was also found on the DMCA samples, upon their dissolution: the height ratio of cellulose I peaks, especially the one at 22.4°, to the broad amorphous peak centred at 18.2° declined, and a crystalline transformation was also indicated by the shifting of the peak at 22.4° (cellulose I) to that at 20.2° (cellulose II), see Figure 4.8.

The change in crystalline structure was more significant for the samples when processing at high temperature, i.e. 50 °C shown in Figure 4.8(b), compared with low temperature such as 30 °C shown in Figure 4.8(a). The double peak at around 15° which is assigned to cellulose I crystal without any notable cellulose II peaks can be used as a guide, allowing the amount of dissolution to be indicated. As the time and/or temperature increased, the double peak became lower, and it changed faster at elevated temperature, suggesting a higher rate of dissolution.

4.3.3 Understanding the dissolution of mercerized cotton in [C2mim][OAc] via TTS analysis

Four parameters, CF_{OM} for DMCY, CF_{XRD} for DMCA, and CF_{OM} and T_H for MCYH, are used to quantify the dissolution process, using the time-temperature superposition analysis.

Upon the dissolution of mercerized cotton single yarns with different combinations of temperature and time, CF_{OM} was measured by OM (Figure 4.5) and calculated with Equation 3.2, of which the results are shown in Figure 4.9.

It is depicted in Figure 4.9(a) that CF_{OM} grows with the increase of processing time and/or temperature, suggesting an agreement with the observation results from the cross-section images in Figure 4.5. A similar time-temperature equivalence on the natural cotton yarns was also found on the dried mercerized cotton yarns, hence a master curve at 40 °C was created by TTS analysis, shown in Figure 4.9(c), which is briefly introduced below.

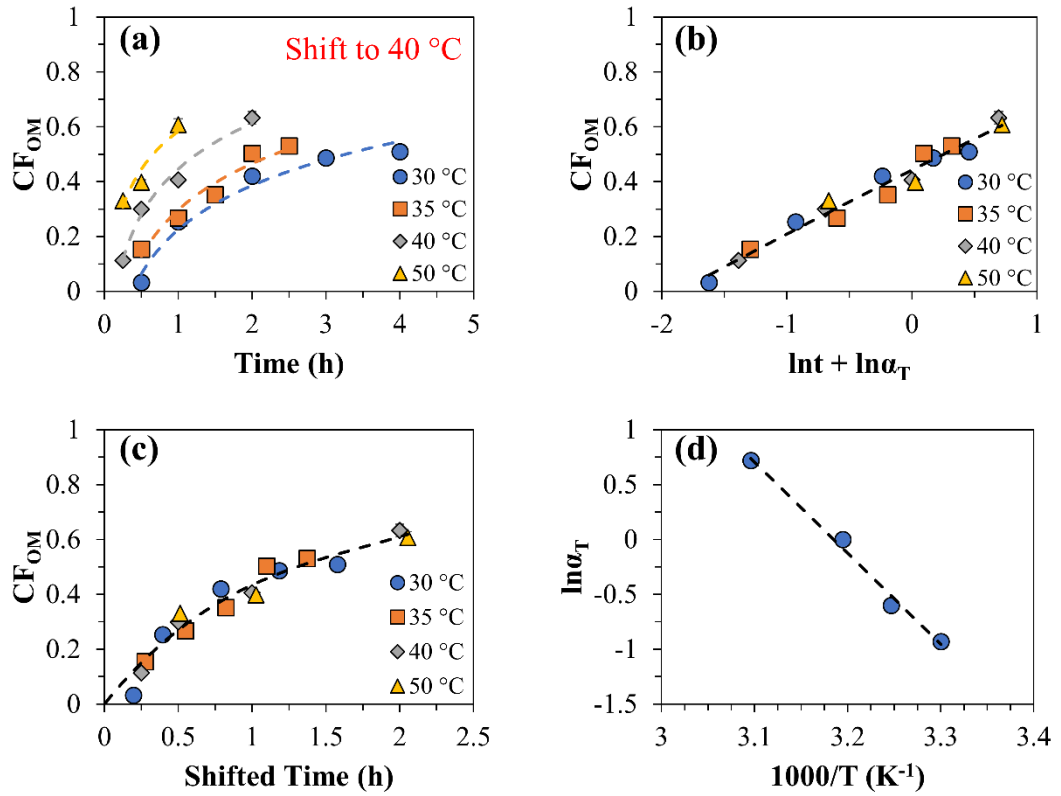


Figure 4.9 (a) Dependence of coagulation fraction, calculated from optical microscopy results of DMCY, on time; the time-temperature superposition plot after being shifted to 40 °C on both (b) natural-logarithmic time scale and (c) linear time scale; (d) Arrhenius plot with $\chi^2 > 0.99$. Some error bars are smaller than the symbols, and the dash lines in (a)-(c) provide guide for eye, and that in (d) is a fitting line

Initially, the dataset at 40 °C was chosen to be the reference, with a shift factor to be one ($\alpha_{40} = 1$), shown in Figure 4.9(a). Then the x-axis was converted to a natural logarithm time scale shown in Figure 4.9(b), and a preliminary polynomial function was applied on the data points of 40 °C. After that, the other datasets were shifted horizontally, by a number equal to $\ln \alpha_T$, to the reference dataset by eye. Finally, all the data points were fitted with a final

polynomial function whose coefficient of determination, χ^2 , was maximized by changing the shift factors, α_{30} , α_{35} and α_{50} .

The finalized master curves at 40 °C on natural logarithmic time scale and linear time scale are formed and shown in Figure 4.9(b) and (c), respectively, proving the equivalence between time and temperature. The dependence of $\ln \alpha_T$, summarized in Table 4.1, on inverse temperature was described with a linear relationship, shown in Figure 4.9(d), which presents an Arrhenius behaviour, allowing an activation energy of 69 ± 5 kJ/mol to be calculated by Equation 3.2. The value compares with the one of 96 ± 8 kJ/mol for natural cotton yarns, about 31% lower. See Figure 4.9(c), the growth speed of CF_{OM} was also found to fall as the processing time increased, then reached a plateau, same as for the natural cotton yarns.

Table 4.1 Shift factors of different temperatures, obtained from the TTS analysis on dried mercerized cotton yarns, used to plot Figure 4.9(d)

Temperature(°C)	α_T	$\ln \alpha_T$	Error in $\ln \alpha_T$
30	0.39	-0.93	0.05
35	0.55	-0.61	0.01
40	1	0	-
50	2.05	0.72	0.01

The dissolution of mercerized cotton yarns is quantified by coagulation fraction (CF_{XRD}), using Equation 2.1, according to the cellulose I area fraction from the deconvolution results of WAXD spectra depicted in Figure 4.8. How the CR_{XRD} changed with different processing conditions is shown in Figure 4.10(a), which

shows a similar dependence on dissolving time and temperature as for the single yarns. TTS analysis was again applied to these datasets, so as to prove the interchangeability between time and temperature by the formation of a convincing master curve at 40 °C, see Figure 4.10(b) and (c).

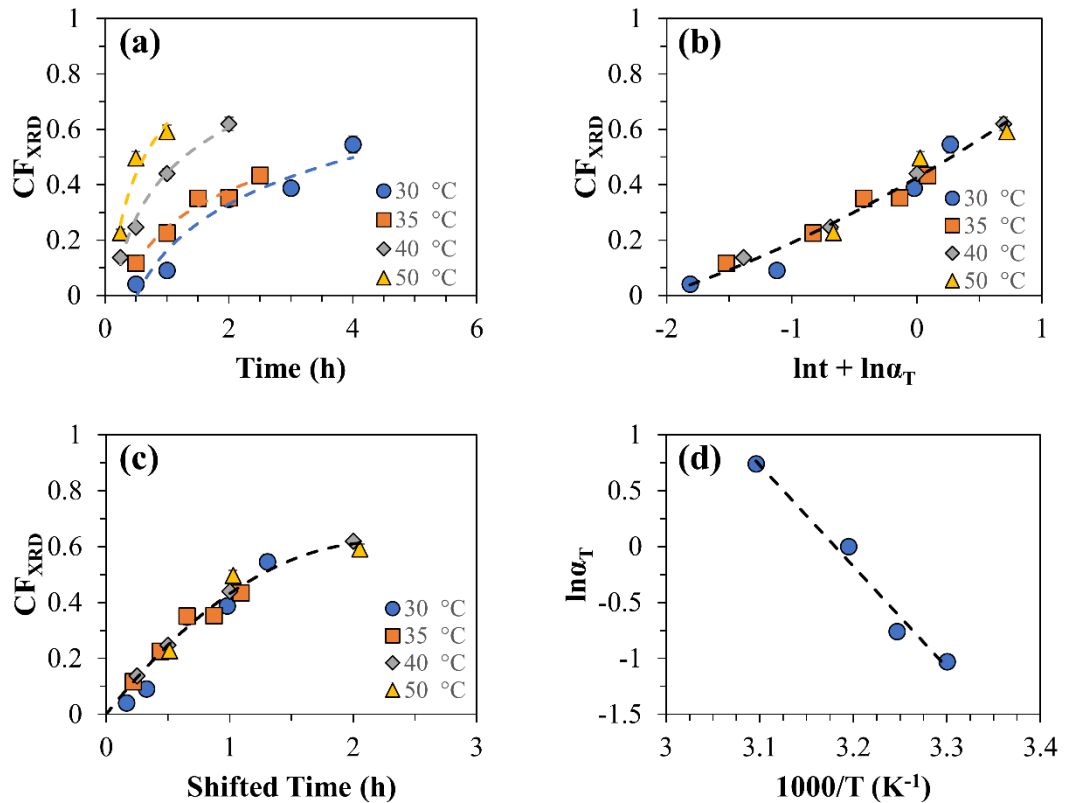


Figure 4.10 (a) Dependence of coagulation fraction (CF_{XRD}), calculated from WAXD results of DMCA, on time; the time-temperature superposition plot after being shifted to 40 °C on both (b) natural-logarithmic time scale and (c) linear time scale; (d) Arrhenius plot with $\chi^2 > 0.97$. Some error bars are smaller than the symbols, and the dash lines in (a)-(c) provide guide for eye, and that in (d) is a fitting line

The shift factors, α_T , used to form the master curve are tabulated in Table 4.2 and their natural logarithm value, $\ln \alpha_T$, is found to have a linear relationship with reverse temperature in kelvin, shown in Figure 4.10(d). The slope of the

Arrhenius plot gives a activation energy of 78 ± 10 kJ/mol to the dissolution of mercerized cotton arrays, which is comparable to the dissolution activation energy of mercerized cotton yarns, at 69 ± 5 kJ/mol, allowing an average value of 74 ± 3 kJ/mol to be calculated.

Table 4.2 Shift factors of different temperatures, obtained from the TTS analysis on dried mercerized cotton arrays, used to plot Figure 4.10(d)

Temperature(°C)	α_T	$\ln\alpha_T$	Error in $\ln\alpha_T$
30	0.33	-1.12	0.01
35	0.44	-0.83	0.01
40	1	0	-
50	2.05	0.72	0.01

This agreement again proves independence of dissolution activation energy on sample arrangement, and confirms the universality of our TTS method to investigate the dissolution behaviour of cellulose samples in [C2mim][OAc] that it is applicable not only to natural cellulose materials consisting of cellulose I and amorphous cellulose, but also to mercerized cellulose materials composed of cellulose I, cellulose II and amorphous fractions.

The other two quantifying methods, based on the coagulation fraction (CF_{OM-H}) and ring thickness (T_H) calculated by Equation 4.1 and Equation 4.2 respectively, were used to explore the dissolution of mercerized cotton samples. They were in conjunction with the size measurement results from the OM transverse-view images of MCYH shown in Figure 4.5(a)-(f), of which the drying, encapsulation and polishing process were not required, therefore,

saving significant time. The dependence of CF_{OM-H} and (T_H) on the processing time and temperature are plotted and depicted in Figure 4.11 and Figure 4.12. respectively.

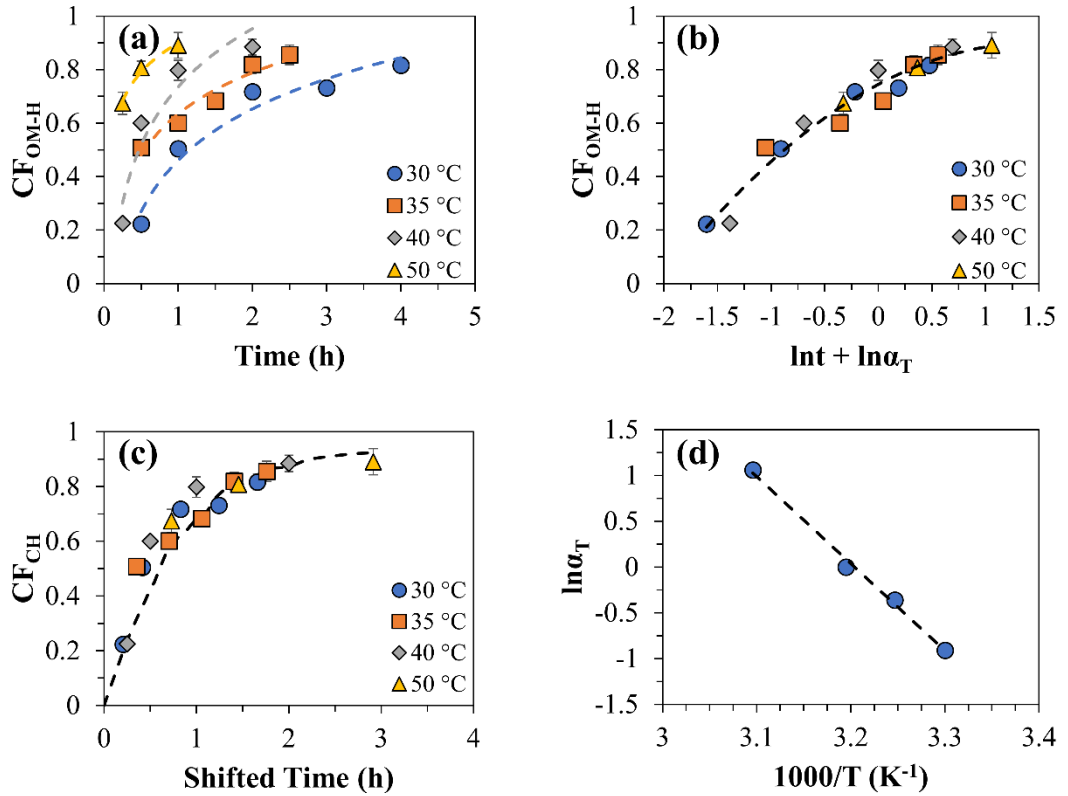


Figure 4.11 (a) Dependence of coagulation fraction (CF_{OM-H}), calculated from WAXD results of MCYH, on time; the time-temperature superposition plot after being shifted to 40 °C on both (b) natural-logarithmic time scale and (c) linear time scale; (d) Arrhenius plot with $\chi^2 > 0.99$. Some error bars are smaller than the symbols, and the dash lines in (a)-(c) provide guide for eye, and that in (d) is a fitting line

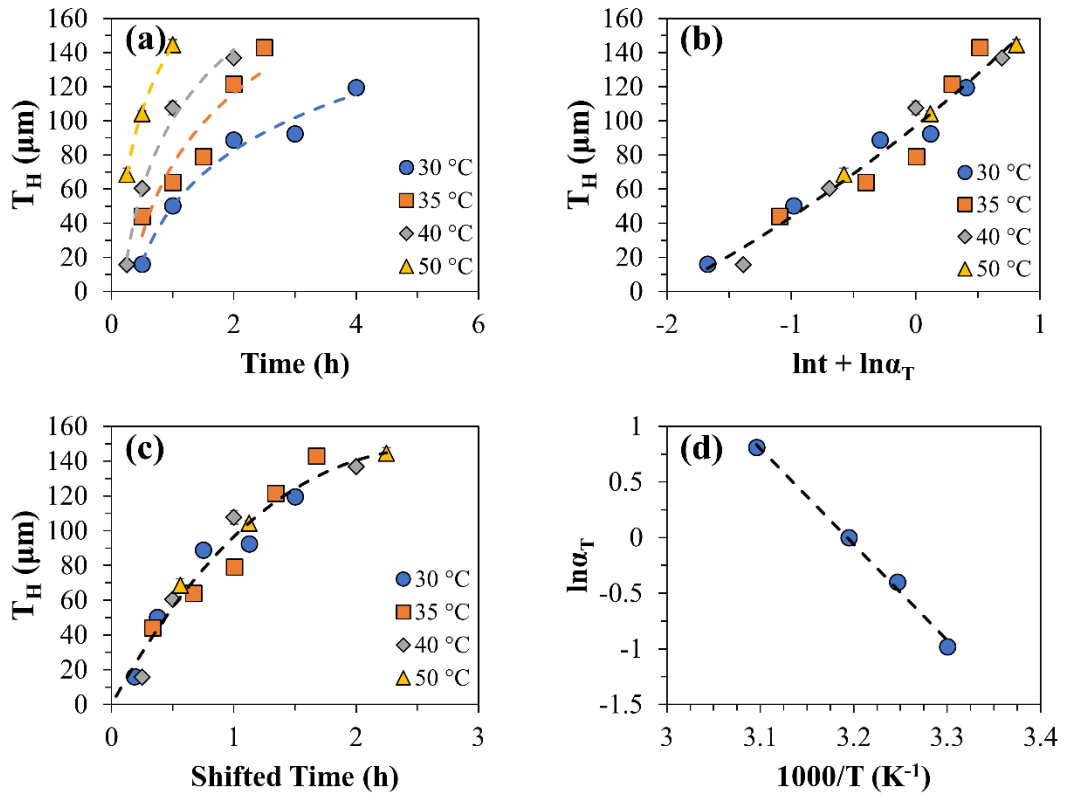


Figure 4.12 (a) Dependence of ring thickness (T_H), calculated from WAXD results of MCYH, on time; the time-temperature superposition plot after being shifted to 40 °C on both (b) natural-logarithmic time scale and (c) linear time scale; (d) Arrhenius plot with $\chi^2 > 0.99$. Some error bars are smaller than the symbols, and the dash lines in (a)-(c) provide guide for eye, and that in (d) is a fitting line

It is shown in Figure 4.11(a) and Figure 4.12(a) that both the CF_{OM-H} and T_H increased with time and/or temperature which is consistent with how the CF_{OM} and CF_{XRD} of the dried samples changed with time and temperature as shown above in Figure 4.9(a) and Figure 4.10(a). Time-temperature equivalence was again found, and master curves at 40 °C, shown in Figure 4.11(c) for CF_{OM-H} and Figure 4.12(c) for T_H , were constructed using our TTS method detailed in section 3.3.2.

Their shift factors (α_T) were summarized in Table 4.3 and found to follow the Arrhenius behaviour, leading to a linear relationship to be found between $\ln \alpha_T$ and the inverse of temperature for both measures of the dissolution, see Figure 4.11(d) and Figure 4.12(d). The gradients of the two lines give 78 ± 4 kJ/mol and 71 ± 3 kJ/mol of dissolution activation energies for CF_{OM-H} and T_H measures on MCYH, respectively. This is in excellent agreement with the value of 74 ± 3 kJ/mol obtained from the TTS analysis for the DMCY and DMCA samples, suggesting again that any parameters could be tracked as a function of time and temperature to check whether TTS holds. It can also be concluded that the measurement of the MCYH is an excellent candidate for following the dissolution of cellulose fibres and determining the activation energy as it saves a significant amount of time. Additionally, the outer ring region of MCYH are much easier to distinguish and follow for lower processing temperatures and times, thus reducing the requirement to the optical microscope - no need for high magnification lenses.

Table 4.3 Shift factors of different temperatures, obtained from the TTS analysis on mercerized cotton yarn hydrogels, used to plot Figure 4.11(d) and Figure 4.12(d)

Qualification parameter	Temperature(°C)	α_T	$\ln\alpha_T$	Error in $\ln\alpha_T$
CF_{OM-H}	30	0.41	-0.88	0.01
	35	0.70	-0.35	0.02
	40	1	0	-
	50	2.92	1.07	0.01
T_H	30	0.38	-0.97	0.01
	35	0.68	-0.39	0.01
	40	1	0	-
	50	2.25	0.81	0.01

The dissolution activation energies obtained from TTS analysis of different quantification parameters are tabulated in Table 4.4. By the comparison among the activation energies from different quantifying methods, they are consistent with each other within their uncertainties, giving an average dissolution activation energy of 74 ± 2 kJ/mol for the mercerized cotton which is about 22 % lower than 95 ± 2 kJ/mol, the dissolution activation energy of the natural cotton in [C2mim][OAc].

Table 4.4 Comparison among the four quantifying methods and the activation energies from them

Characterization	Sample	Quantification parameter	Activation energy (kJ/mol)
OM	DMCY	CF_{OM}	69 ± 5
WAXD	DMCA	CF_{XRD}	78 ± 10
OM	MCYH	CF_{OM-H}	78 ± 4
OM	MCYH	T_H	71 ± 4

4.3.4 Regional water volume fraction and swelling ratio of mercerized cotton yarn hydrogels

The water volume fraction of different regions in MCYH, including the outer ring and central core, was calculated with Equation 4.6. Its dependence on processing time and temperature is shown in Figure 4.13(a) and (b). Equation 4.7 and Equation 4.8 are used to calculate the swelling ratios at the outer ring and central core of different MCYH samples upon the drying process, respectively, and the results are depicted in Figure 4.13(c) and (d).

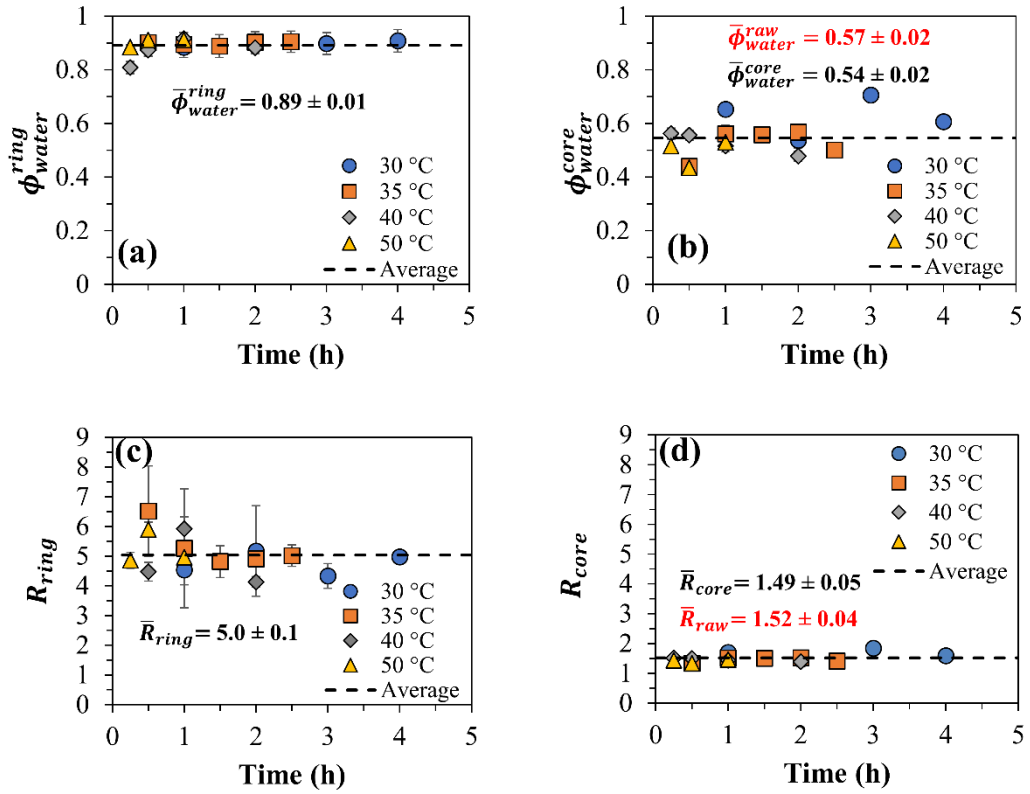


Figure 4.13 Water volume fraction of (a) outer ring and (b) central core of MCYH, and swelling ratio of (c) outer ring and (d) central core in MCYH, where the dash lines measure their average values and some error bars are smaller than the symbols

The water volume fraction in both regions was constant within the measurement uncertainties and was therefore independent of the processing time and/or temperature, see Figure 4.13(a) and (b), giving an average water volume fractions of 0.89 ± 0.01 for the outer ring and 0.54 ± 0.02 for central core. This indicates that there was more water in the outer ring/coagulated region than the central core/undissolved region. A similar independence on the dissolution time and/or temperature was found for the swelling ratio of both regions after the drying process. The average swelling ratio of the outer ring is 5.0 ± 0.1 which is about 3 times higher than that of the central region, 1.49 ± 0.05 . To recap, the higher is the swelling ratio, the more is the difference in

size between the hydrogel and dried sample, so that the outer ring shrank more than central region upon drying. This can be explained by the huge difference of water volume fraction between the two regions in MCYH samples and once the water was evaporated, different regions collapsed heterogeneously. The results are summarized and compared in Table 4.5.

Table 4.5 Comparative summary of different samples/regions in water volume fraction and shirring ratio

Region/Sample	Water volume fraction ϕ_{water}	Swelling ratio R
MCYH-raw*	0.57 ± 0.02	1.52 ± 0.04
Central core of MCYH	0.54 ± 0.02	1.49 ± 0.05
Outer ring of MCYH	0.89 ± 0.01	5.0 ± 0.1

*MCYH-raw means the damp raw sample after soaking in water for 24 hours.

Compared with the MCYH-raw, the central core of MCYH depicted high consistency in terms of both water volume fraction and swelling ratio when the uncertainties were taken into consideration, by contrary, the outer ring of MCYH presented a totally opposite result. This implies that no dissolution happened in the central region. Therefore, the earlier assumption that there is no dissolved cellulose in the central core is confirmed. Further, the hypothesis is confirmed that the dissolution only proceeds from the exterior surface of yarn samples.

The water volume fraction and swelling ratio of the MCYH-raw sample, made by soaking the raw mercerized cotton yarn in water for 24 hours, were

calculated by Equation 4.6 and Equation 4.8, respectively. It should be noted that, the radius and cross section area of the dried raw sample used in the calculations were measured on the DMCY-30-0.25 sample. This is because: filaments in the dry raw sample were swollen by the epoxy resin when preparing for OM, shown in Figure 4.7(g), which would lead to a larger size to be measured than the actual; and the processing at low temperature for short time, i.e. 30 °C for 0.25 hours, could just start the dissolution at the sample's very outer edge, allowing the formation of an invisible and unmeasurable thin layer with OM, which protected the filaments from swelling caused by epoxy resin, see Figure 4.7(b) and (h). Besides, as no dissolution happened to the MCYH-raw sample, the water volume fraction and swelling ratio of its outer ring cannot be calculated and so not to be discussed.

Further, to verify if DMCY-30-0.25 could be used instead of the dry raw sample in the size measurements, a method for measuring the theoretical values is introduced - the plots of radius of the central core vs. ring thickness of both DMCY and MCYH are used to measure the theoretical diameters of DMCY-raw and MCYH-raw respectively, see Figure 4.14.

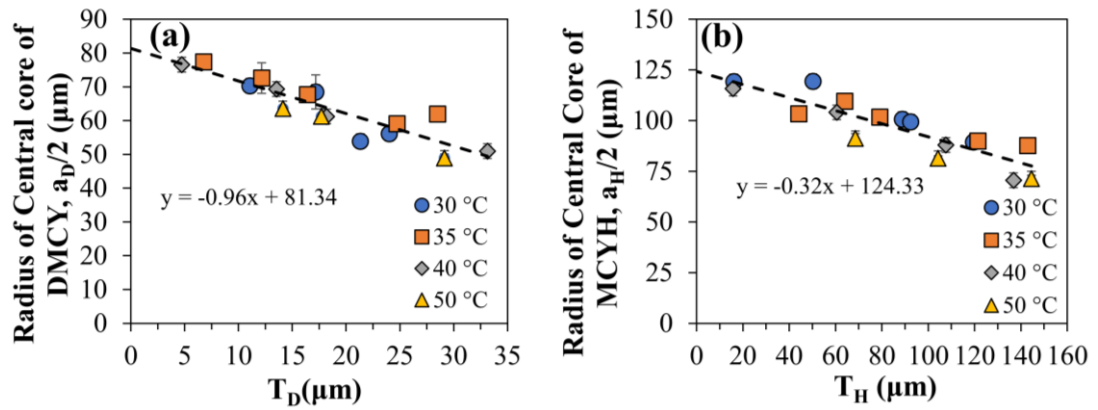


Figure 4.14 Radius of central core dependence on the ring thickness in (a) dried mercerized cotton yarn (DMCY) samples and (b) mercerized cotton yarn hydrogel (MCYH) samples, where the dash lines are linear fitting lines, and some error bars are smaller than the symbols

The results show that with the ring thickness increasing – with the dissolution progressing – the radius of central core was decreasing, and this was found on both DMCY and MCYH samples. By examination, a linear relationship between the central core radius and ring thickness was confirmed, see the dash lines in both Figure 4.14(a) and (b), suggesting a further time-temperature equivalence. By extrapolating the corresponding ring thickness to zero, which would correspond to a sample with no coagulated material, i.e. the raw sample, the central core radii for DMCY-raw and MCYH-raw were found to be $81 \pm 2 \mu\text{m}$ and $124 \pm 4 \mu\text{m}$ respectively, by assistance of the LINEST method in Excel. Shown in Table 4.6, the later one, $124 \pm 4 \mu\text{m}$, is in a good agreement with the OM-measured radius of MCYH-raw sample, $122 \pm 1 \mu\text{m}$, suggesting that the way of measuring the theoretical size of raw sample introduced in Figure 4.14 is reliable. By the comparison between the radius of DMCY-30-0.25 and the theoretical value of DMCY-raw, they are

consistent with each other which confirms that the DMCY-30-0.25 represents the DMCY-raw with a good approximation.

Table 4.6 Theoretical radii of MCHY-raw and DMCY-raw obtained from the extrapolating method and those in brackets measured directly from microscope pictures

The radius of MCHY-raw (r') (μm)	The radius of DMCY-raw (r) (μm)	Swelling ratio ($R_o=r'/r$)
124 ± 4 (122 ± 1)	81 ± 2 ($80 \pm 2^*$)	1.53 ± 0.06 (1.52 ± 0.04)

*the DMCY-raw radius shown within the brackets was measured on DMCY-30-0.25 from its OM image, Figure 4.7(h).

4.4 Conclusions

The dissolution of mercerized cotton cellulose in [C2mim][OAc] has been successfully studied using OM and WAXD at different dissolving times and temperatures. OM was used to both MCHY and DMCY samples for characterizing their micromorphology and a coagulated ring-like region was found surrounding the central-undissolved core. WAXD was applied to DMCA samples for measuring their crystalline structure after the dissolution in [C2mim][OAc] and the raw material consists of 40.7 % cellulose I, 19.7 % cellulose II and 39.6% amorphous region. Similar to the dissolution of natural cotton, the dissolution of mercerized cotton also showed time-temperature equivalence. For further understanding the dissolution behaviour, four quantifying methods were applied by tracking different quantification parameters, CF_{OM} for DMCY from OM, CF_{XRD} for DMCA from WAXD, CF_{OM-H} and T_H both for MCHY from OM, as a function of time and temperature, to create master curves using TTS analysis. The Arrhenius

behaviour was used to quantify the kinetics of dissolution of the mercerized cotton cellulose, allowing the activation energies associated with CF_{OM} , CF_{XRD} , CF_{OMH} and T_H to be obtained as 69 ± 5 kJ/mol, 78 ± 10 kJ/mol, 78 ± 4 kJ/mol and 71 ± 4 , respectively. Interestingly, these activation energies show an independence of quantifying method, giving an average value of 74 ± 2 kJ/mol. It indicates the measurement of MCYH with OM is an excellent candidate for investigating the cellulose dissolution behaviour, as it significantly shortens time on experiment and also confirms the universality of our TTS analysis method – feasible on both natural and mercerized cotton cellulose.

In addition, regional water volume fraction and swelling ratio of MCYH were also measured with a facile and novel method which to the best of our knowledge has been reported for the first time. The water volume fraction and swelling ratio at the central core of MCYH are consistent with that of the undissolved raw material, proving the hypothesis that little/no dissolution happened in the central core.

The findings in this chapter can be used for exploring the dissolution of other cellulose materials. In the following chapters: the dissolution master curves will be further applied to direct the fabrication of all cellulose composites from the mercerized-cotton based textiles; and the reasons for the difference of dissolution activation energy between the natural cotton cellulose and mercerized cotton cellulose could be due to the difference in crystalline structure, carbohydrate composition and molecular weight. The effecting factors will be further analysed in Chapter 5.

Chapter 5 Comparative analysis of cellulose from the natural and mercerized cotton in chemical composition, molecular weight, thermal stability and dissolution kinetics

5.1 Introduction

The dissolution process of cellulose from natural cotton and mercerized cotton in EMIMAc has been investigated earlier in this thesis via TTS analysis, where the dissolution was quantified with an activation energy via an Arrhenius plot. The dissolution activation energy was found to be independent of the sample arrangement and the quantifying method, giving an average activation energy of dissolution of the cellulose, from natural cotton and mercerized cotton, to be 95 ± 2 kJ/mol and 74 ± 2 kJ/mol, respectively. The work reported in this chapter is the main content of Paper IV.

Different cellulose polymorphs are reported to have different thermal stabilities, which is usually measured via thermogravimetric analysis (TGA). Published results suggest that cellulose II is more thermally stable than cellulose I, due to a higher degradation temperature and a higher pyrolysis activation energy of cellulose II.[188, 190] The kinetic research on the pyrolysis of cellulose-based materials can be tracked back to the 1950s [194]. Although pyrolysis is a thermally stimulated heterogeneous reaction, the theories of the kinetic model are mostly developed from those of homogeneous reaction kinetics [195]. The conversion, γ , expressing how much of the organic substance is pyrolyzed, is applied rather than the reactant concentration, which can be calculated with the initial sample weight (w_o), the initial water content (w_{H_2O}) the sample weight at time t , w_t , and the residual

char weight (w_{∞}) via Equation 2.1 [196]. The reaction rate can then be expressed by Equation 5.2 [197]:

$$\gamma = \frac{w_o - w_{H_2O} - w_t}{w_o - w_{H_2O} - w_{\infty}} \quad \text{Equation 5.1}$$

$$\frac{d\gamma}{dt} = k(T)f(\gamma) \quad \text{Equation 5.2}$$

where the rate constant $k(T)$ can be described with an Arrhenius theory with Equation 5.3, of which A and E are the pre-factor and the pyrolysis activation energy respectively; and $f(\gamma)$ is a chosen reaction model, with reaction order to be n , and is generally written as Equation 5.4 [197].

$$k(T) = A \exp\left(-\frac{E}{RT}\right) \quad \text{Equation 5.3}$$

$$f(\gamma) = (1 - \gamma)^n \quad \text{Equation 5.4}$$

In the kinetic research of cellulose pyrolysis, two measurements, isothermal [198] and non-isothermal measurements [199], are used. In this thesis only linear heating methods with a heating rate of β as shown in Equation 5.5, belonging to non-isothermal measurements, are used, and discussed.

$$T = T_o + \beta t \quad \text{Equation 5.5}$$

where T_o and t are the initial temperature and the evolving time, respectively. By combining the equations above, Equation 5.2 can be rewritten as:

$$\frac{d\gamma}{dt} = \frac{d\gamma}{dT} \frac{dT}{dt} = \frac{d\gamma}{dT} \beta = A \exp\left(-\frac{E}{RT}\right) (1 - \gamma)^n \quad \text{Equation 5.6}$$

Among the non-isothermal measurements, two method directions can be summarised: the model-fitting method and the so-called “model-free” method. For the former, the reaction model, $f(\gamma)$, is assumed in advance and then fitted to the experimental data to obtain the kinetic parameters. The first order global model (FOG), where n in Equation 5.4 is unity, has been intensively used for cellulose pyrolysis. It is considered as satisfactorily manifesting the process at linear heating rates up to 100 °C/min and the kinetics can be represented by this single-step process [195, 200]. Although there have been huge research efforts on the subject of cellulose pyrolysis models, the most appropriate kinetic model still remains unclear. But in terms of chemical reactions, three stages related to three chemical transformations were proposed by Garcia-Perez [201], which are described as follows: The primary thermal pyrolysis stage is the thermal degradation observed at up to 700 °C where cellulose-derived molecules - mainly fluids such as levoglucosane and hydroxylacetaldehyde - are generated; the second stage is between 700-850 °C where some gaseous olefins and secondary condensed oils are produced; in the tertiary stage ranging from 850-1000 °C, non-condensable gases are formed with secondary pyrolysis products. Moreover, a primary cellulose pyrolysis stage at 230 to 380 °C was confirmed by an in-situ visualisation technique by Zhu et al [202].

For the model-free methods, they are based on the principle that the reaction speed is only a function of temperature at constant conversion, also called the iso-conversional method, and does not need the prior assumption of the form

of $f(\gamma)$. The kinetic parameters, activation energy and pre-factor, can be determined from a series of TGA tests carried out with different heating rates, normally at least three rates [195, 203]. There are two categories of iso-conversional methods: differential methods and integral methods. Due to the fact that no approximations which could lead to discrepancies of the temperature integral and no requirement on the prior assumption of $f(\gamma)$ are needed; the differential methods on the same equations are theoretically more reliable than the integral methods [197]. The Friedman method is the most commonly used differential method [197], where the pyrolysis activation energy can be calculated from the slope obtained by linear regression of $\ln\left(\frac{d\gamma}{dt}\right)$ against $\frac{1}{T}$ and it can be derived from Equation 5.6 to be:

$$\ln\left(\frac{d\gamma}{dt}\right) = \ln\left(\frac{d\gamma}{dT} \frac{dT}{dt}\right) = \ln\left(\beta \frac{d\gamma}{dT}\right) = \ln[Af(\gamma)] - \frac{E}{R} * \frac{1}{T} \quad \text{Equation 5.7}$$

The reported pyrolysis activation energy ranges of cellulose, hemicellulose and lignin are from 135 to 223 kJ/mol [204-211], 115 to 144 kJ/mol [208, 209, 211-214] and 23 to 108 kJ/mol [208, 209, 211, 212, 215], respectively. Their decomposition temperatures range from 220 to 315 °C for hemicellulose, from 300 to 400 °C for cellulose and 150 to 900 °C for lignin [216, 217]. In other words, the hemicellulose is less thermally stable than cellulose, and lignin has the widest thermal degradation temperature range among them. It has been reported that the crystallinity/crystalline size [218, 219], chemical composition [211, 220] and degree of polymerization [221] can influence the thermal stability of lignocellulose in a complex way.

In contrast, there has been almost no research into the factors affecting the dissolution activation energy of these cellulose-based materials in [C2mim][OAc]. Research conducted by Qi et al. shows that the dissolution behaviour of cellulose in NaOH/urea aqueous solution is dependent on the viscose-average molecular weight and the crystallinity of the cellulose samples, where the higher the molecular weight and/or the crystallinity, the more difficult the dissolution was, where the solubility activation energy varied from 47 to 134 kJ/mol [222].

In this chapter, the two cotton samples, raw and mercerised, are compared according to the results of OM, XRD, chemical-compositional analysis, molecular weight and distribution analysis, and TGA. The FOG method and Friedman method are compared in order to confirm the appropriate one for the pyrolysis analysis on the two samples under the TGA measurement conditions implemented in this section, and a modified first order global (FOG) method is developed for modelling, giving pyrolysis activation energies to be confirmed on both the cotton samples. Then the difference in the dissolution activation energy in [C2mim][OAc] and the pyrolysis activation energy can be analysed according to the other characteristics of the samples, such as crystalline structure, molecular weight, and chemical composition.

5.2 Methods

5.2.1 Optical microscopy

The images of cross sections of the raw natural cotton yarn (NY-raw) and raw mercerized cotton yarn (MCY-raw) are obtained via an optical microscope under the light reflection mode, are detailed earlier in section 2.2.1.

5.2.2 Wide-angle X-ray Diffraction

To characterize the crystalline allomorph of the NY-raw and MCY-raw, WAXD was performed with more detail as described earlier in section 2.2.2.

5.2.3 Determination of weight-average molecular weight and molecular weight distribution

The weight-average molecular weight (M_w), number-average molecular weight (M_n) and the molecular weight distribution (MWD) of the natural cotton and mercerized cotton samples are measured with the technique of multi-angle laser light scattering (MALLS), where the refractive index (RI) is used to determine the molecular weight [223, 224]. The solution used for injection was prepared as the following: First, the cotton samples were soaked in a water bath for 7 days at 40 °C before the solvent was exchanged from water to ethanol and finally into dimethylacetamide (DMAc). The samples were kept in the DMAc for 12 hours and then fully dissolved in a 9% solution of LiCl in DMAc. Each sample was measured twice. Here, I would like to express my special gratitude to Prof. Antje Potthast, University of Natural Resources and Life Science for conducting the above-mentioned measurements, i.e. the measurement of molecular weights and molecular weight distribution.

5.2.4 Determination of the content of lignin and hemicellulose

First, the samples were cryogenically milled in a Retsch mill for 5-10 min and then thoroughly dried at 40 °C with a vacuum oven.

In terms of the determination of the lignin content, the protocol of Iiyama and Wallis [225] and the modification of Hatfield et. al. [226] was used on both the

natural cotton and the mercerized cotton samples. Triplicate measurements were done on each sample. The analysis of the hemicellulose content was performed in accordance to the acid methanolysis reported by Sundberg et al. [227]. Again, here, I would like to express my special gratitude to Prof. Antje Potthast, University of Natural Resources and Life Science for conducting the above-mentioned measurements, i.e. the determination of the contents of lignin and hemicellulose.

5.2.5 Thermogravimetric analysis

A TGA machine (STA 449 F3, NETZSCH-Gerätebau GmbH, Germany) was applied to perform the thermal stability analysis of the cotton samples from 30 °C to 650 °C with linear ramping speeds of 5, 10, 20 and 50 °C/min, under a Nitrogen purge gas of 40 ml/min. Each sample was cut into about 0.5 mm long short fibres, and the total weight was ca. 10 mg for each test, contained in 70uL Al₂O₃ crucibles. All the TGA measurements mentioned above were conducted with the help of Dr. Adrian Cunliffe and Karine Alves Thorne, CAPE Analytical Facilities Organisation, University of Leeds.

5.2.6 Theoretical considerations and calculation procedures for the pyrolysis analysis

The TGA data were analysed and modelled with a method modified from the simple FOG model [195, 196, 200], and the equations used in this method are shown as:

$$\int_y^1 \frac{dy}{y^n} = \int_y^1 \frac{dy}{y} = \frac{A}{\beta} \int_{T_o}^T \exp\left(-\frac{E}{RT}\right) dT \quad \text{Equation 5.8}$$

Where y equals $1 - \gamma$, and the left-hand side could be integrated to be:

$$\int_y^1 \frac{dy}{y^1} = \ln\left(\frac{1}{y}\right) \quad \text{Equation 5.9}$$

As the right-hand side of Equation 5.8 cannot be integrated simply, approximations have to therefore be applied for its integration. When T is very close to the temperature of maximum pyrolysis speed, T_m , whose value can be confirmed from DTG curves, three approximations can be applied [196]:

$$\exp\left(-\frac{E}{RT}\right) \approx \left[\left(\frac{T}{T_m}\right) e^{-1}\right]^{\frac{E}{RT_m}} \quad \text{Equation 5.10}$$

$$\exp\left(-\frac{E}{RT}\right) \approx \exp\left[-\frac{E}{RT_m} * \left(2 - \frac{T}{T_m}\right)\right] \quad \text{Equation 5.11}$$

$$\exp\left(-\frac{E}{RT}\right) \approx \left(\frac{T_m}{T}\right)^2 \exp\left(-\frac{E}{RT}\right) \quad \text{Equation 5.12}$$

The three approximations yield three integration results, respectively

$$\ln\left[\ln\left(\frac{1}{y}\right)\right] = \left(\frac{E}{RT_m} + 1\right) \ln T + C_1 \quad \text{Equation 5.13}$$

$$\ln\left[\ln\left(\frac{1}{y}\right)\right] = \frac{E}{RT_m^2} * T + C_2 \quad \text{Equation 5.14}$$

$$\ln \left[\ln \left(\frac{1}{y} \right) \right] = -\frac{E}{R} * \frac{1}{T} + C_3 \quad \text{Equation 5.15}$$

where C_1 , C_2 and C_3 are constants, and slopes from the linear fittings ($\frac{E}{RT_m} + 1$, $\frac{E}{RT_m^2}$ and $-\frac{E}{R}$) can be used to calculate the activation energy. For the sake of simplicity, hereafter the three equations, Equation 5.13, Equation 5.14 and Equation 5.15, are referred to as the $\ln T$, T and $\frac{1}{T}$ methods, respectively. These approximations are only valid when the temperature range is very close to T_m , otherwise wide temperature ranges will introduce non-negligible errors. Therefore, in this thesis a modified FOG method is applied for the kinetic research on the pyrolysis of natural cotton and mercerized cotton samples, and more details will be given later.

5.3 Results and discussion

5.3.1 Morphology of the two cotton yarns

The microscopic cross-section pictures of the NY-raw and MCY-raw are obtained from the optical microscope via light-reflection mode and shown in Figure 5.1.

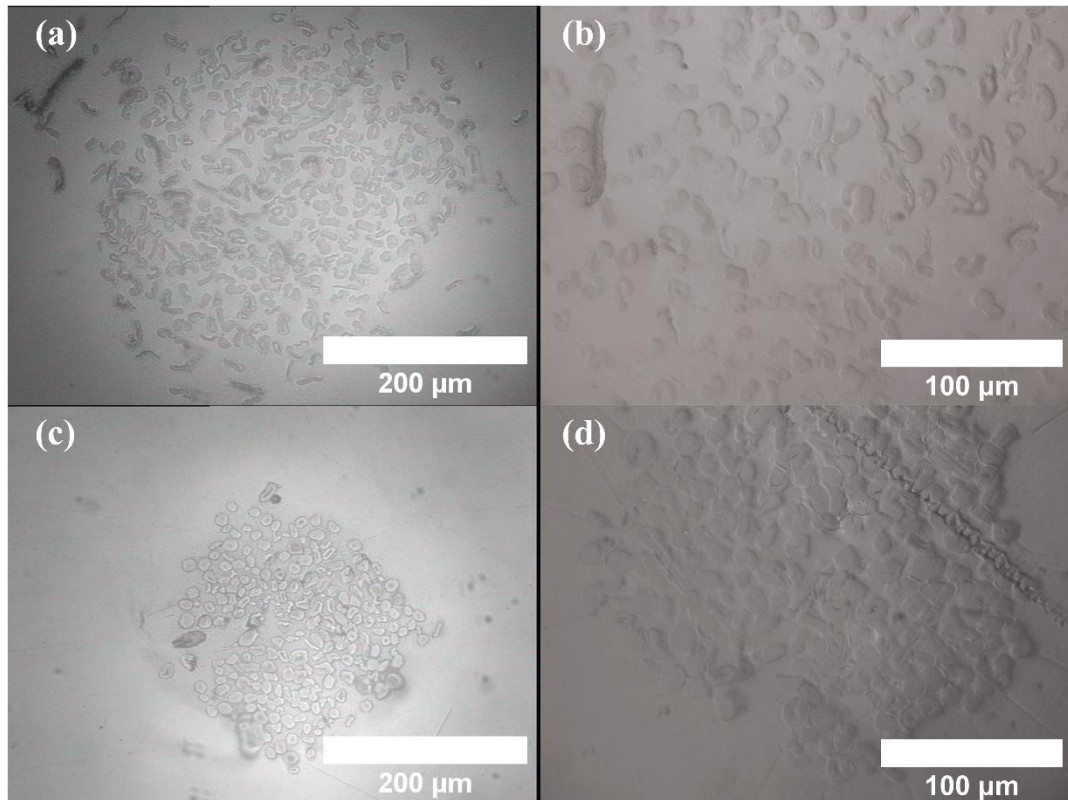


Figure 5.1 Cross-section images of the raw natural cotton yarn (NY-raw) in (a) low magnification and (b) high magnification; the raw mercerized cotton yarn (MCY-raw) in (c) low magnification and (d) high magnification

Shown in Figure 5.1 (a), the filaments comprising the NY-raw sample are kidney shaped, which can be further confirmed by a higher magnification image in Figure 5.1 (b), showing a distorted and contorted cross-section of the crushed lumens. While in the MCY-raw sample, the cross-sections of filaments are substantially round, see Figure 5.1 (c) and (d). The changes in morphology are consistent with the results reported elsewhere, in which the bean-like natural cotton fibre finally transformed into a round shape upon the mercerization process [190]. The difference in the cross-section shape is caused by the high affinity of caustic soda for cellulose which makes it penetrate both the crystalline and amorphous regions, leading to a weakening effect on the interactions between cellulose molecules and a decrease in

strength [185]. After the cotton samples are rinsed and dried, the strength recovers. Upon this process, cellulose I is partially transformed to cellulose II, and decrease is seen in crystallinity, which is usually accompanied by the decrease/removal of hemicellulose and lignin[188].

5.3.2 Comparison between the natural cotton yarn and the mercerized cotton yarn in terms of carbohydrate composition and molecular weight

The carbohydrate composition analysis and the MALLS/RI measurement for the molecular weight analysis were conducted by Prof. Antje Potthast's group in the University of Natural Resource and Life Science, and the results are shown in Table 5.1 and Table 5.2.

As shown in Table 5.1, the lignin content in the NY-raw, at 1.29 %, was slightly higher than that in the MCY-raw, at 1.04%; and the carbohydrate composition resultants of hemicellulose were detected in the NY-raw sample. While they were not detectable in the MCY-raw sample, which means the mercerization process removed some lignin and all/most the hemicelluloses from the cotton samples. These results indicate a good agreement with the results from the microscopic images in Figure 5.1 and the WAXD spectra in Figure 2.1.

Table 5.1 Comparison of the natural cotton yarn and the mercerized cotton yarn in carbohydrate composition, including lignin and hemicellulose

Property	NY-raw	MCY-raw
Lignin content of dry samples (mg/g)	12.90	10.40
Arabinose (mg/g)	3.94	null
Rhamnose (mg/g)	1.23	null
Xylose (mg/g)	2.08	null
Galacturonic acid (mg/g)	6.73	null
Mannose (mg/g)	null	null
Galactose (mg/g)	2.72	null
Glucose (mg/g)	156.69	142.95

Table 5.2 Results of molecular weight analysis on the raw natural cotton yarn and the raw mercerized cotton yarn samples

Sample	M_n (kDa)	M_w (kDa)	Polydispersity [M_w/M_n]	Reg (μmol/g)
NY-raw	653 ± 18	1069 ± 19	1.64 ± 0.07	1.53 ± 0.04
MCY-raw	252 ± 5	385 ± 4	1.53 ± 0.02	3.98 ± 0.09

As for the molecular weights including the M_n, M_w and the dispersity, the NY-raw sample is about 2.5 times higher than the MCY-raw sample in the molecular weights, and also shows a slightly larger dispersity, see Table 5.2 and Figure 5.2. This could be due to the fact that the mercerization process degrades the cellulose molecules and reduces the low molecular weight carbohydrate polymers, i.e. the hemicellulose, which is consistent with the carbohydrate composition analysis showing no detectable hemicellulose in

the MCY-raw sample. It could also be due to the different plant source for the raw cotton before it was mercerized.

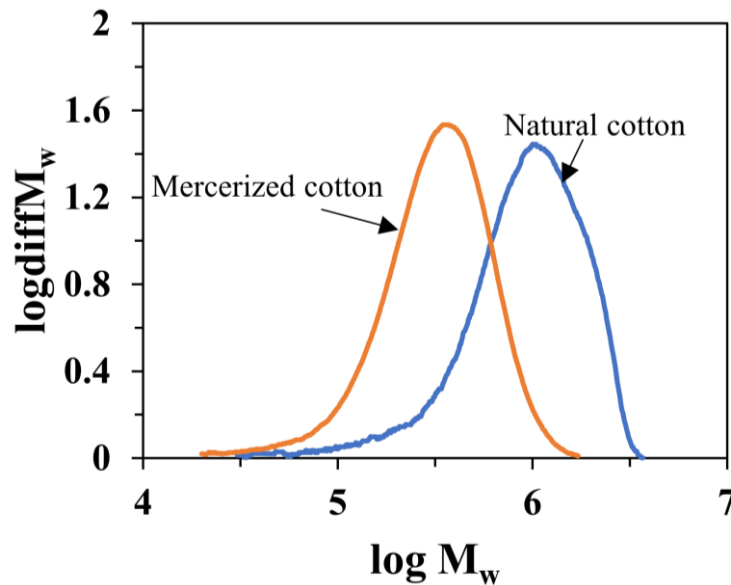


Figure 5.2 Molecular weight distribution of the mercerized cotton and the natural cotton

It has been concluded in a recent paper [222] that the dissolution activation energy of cellulose, measured by tracking the changes in solubility, with viscosity-average molecular weight (M_{η}) ranging from $3.1 \cdot 10^4$ to $13.1 \cdot 10^4$ in NaOH/urea aqueous solution was significantly dependant on M_{η} . The dependence of the dissolution activation energy of cellulose on M_{η} reported in the paper is shown in Figure 5.3 , where the dissolution activation energy of cellulose increased as the M_{η} increased, and this is in agreement with our finding that the NY-raw with larger molecular weight has higher dissolution activation energy in [C2mim][OAc] than MCY-raw with lower molecular weight. The reason can be hypothesized as that the dissolution is happening at a molecular level, and the higher the molecular weight is, the longer the

cellulose molecules are, leading to a higher energy barrier to overcome for separating different molecules during dissolution process.

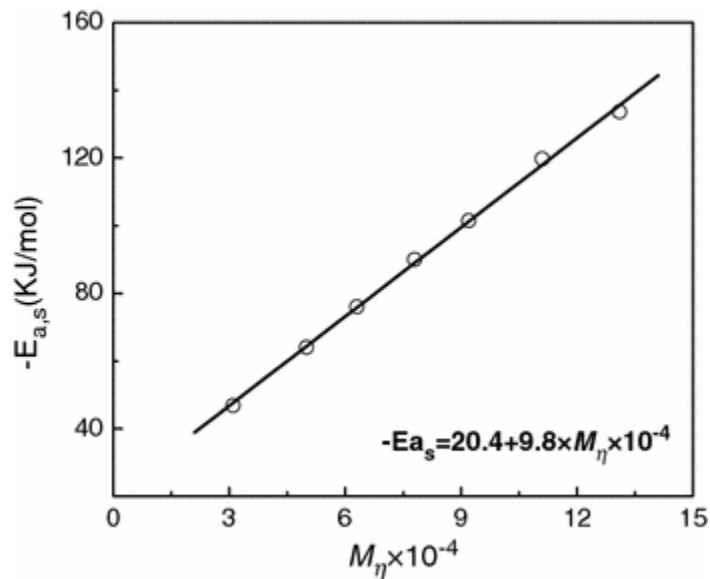


Figure 5.3 Plot of dependence of dissolution activation energy ($E_{a,s}$) of cellulose samples on viscosity-average molecular weight (M_{η}) reported by Qi et al. [222]

It is noteworthy that the carbohydrate composition and crystalline structure are different in the two samples, which could also be reasons for the difference of dissolution activation energy. In terms of the effect of crystalline structure on the dissolution of cellulose in [C2mim][OAc], it has been reported that this dissolving process is controlled by molecular disentanglement - the crystalline structure has a small impact on the dissolution [228, 229]. As of the time of writing, there has not been any research reported on the influence of carbohydrate composition on the dissolution activation energy of cellulose samples. Therefore, we propose a method that could solve this issue - mercerizing the natural cotton yarn with different combinations of NaOH aqueous solution concentrations and processing temperature to control the carbohydrate composition where the change in molecular weight should be

controlled to be as less as possible, and do TTS analysis on their dissolution behaviour, according to the methods introduced in the previous chapters. This will be focus of future studies.

5.3.3 Thermal stability comparison of the natural cotton yarns and the mercerized cotton yarns via TGA

TGA was conducted to characterize the thermostability of the two cotton samples at different heating speeds (5, 10, 20 and 50 °C/min), and the results are shown in Figure 5.4.

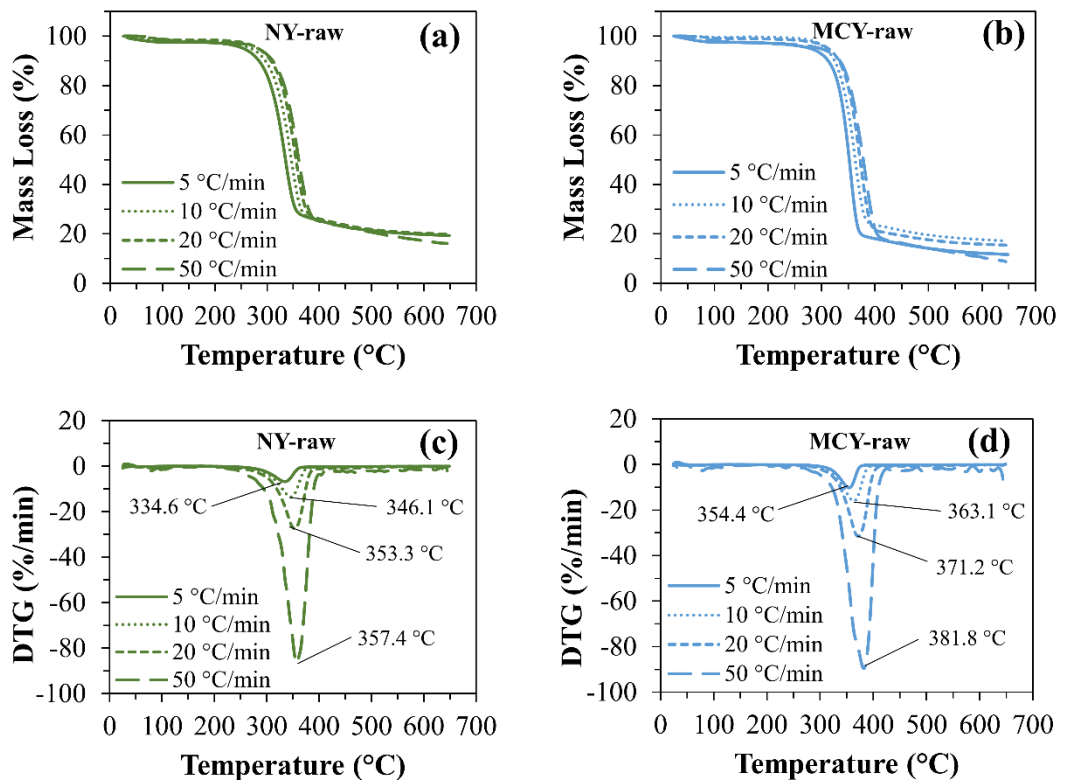


Figure 5.4 Thermogravimetric analysis curves at different heating speeds for (a) the raw natural cotton yarn (NY-raw) and the raw mercerized cotton yarn (MCY-raw); and derivative thermogravimetric (DTG) curves at different temperature ramping rates for (c) NY-raw and (d) MCY-raw

It can be shown from Figure 5.1 (a) and (b) that every TGA curve presents a single decomposition stage after a tiny weight loss step, ca. 4 %, located at around 80 °C and attributed to water loss, indicating a primary pyrolysis stage. For both NY-raw and MCY-raw samples, the decomposition stage shifted to higher temperature ranges as the heating rate increased, see the DTG curves in Figure 5.4 (c) and (d). The shifting of the decomposition stage is caused by the transfer limitation of heat and mass, resulting in a temperature gradient inside the samples [230].

For NY-raw, the decomposition began at around 270 °C and continued until 390 °C, while for MCY-raw, the start-decomposition temperature was found from 310 °C to 410 °C. Figure 5.4 (c) indicates that the maximum decomposition rate of NY-raw was between 334.6 °C and 357.4 °C within the range of heating rate, which is lower than MCY-raw, from 354.4 °C to 381.8 °C, shown in Figure 5.4 (d). The temperature at the maximum decomposition rate, T_m , increased with heating rate, β , and in order to get the intrinsic temperature at the maximum decomposition rate, $[T_m]$, which is the T_m when $\beta = 0$, the dependence of T_m on β is plotted and shown in Figure 5.5. Examination of the plots suggests that T_m dramatically increased in the beginning until it reached a plateau, and this applies to both sample cases. Therefore, we propose an exponential fitting equation to do modelling of the two datasets, expressed with the equation below to determine T_m :

$$T_m = a \times (1 - e^{-b\beta}) + [T_m] \quad \text{Equation 5.16}$$

where a , b are constants, and $[T_m]$ can be confirmed from the intercept where heating rate is zero, see Figure 5.5. The confidence of the fitting can be

expressed with the coefficient of determination, χ^2 which are larger than 0.99 in both NY-raw and MCY-raw datasets, giving $[T_m]$ to be 317 ± 6 °C and 346 ± 3 °C respectively.

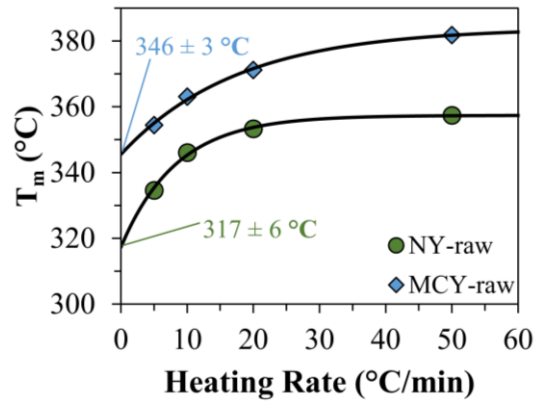


Figure 5.5 Dependence of the temperature at the maximum decomposition rate (T_m) on the heating rate of TGA on both raw natural cotton yarn (NY-raw) and raw mercerized cotton yarn (MCY-raw) where the datasets are fitted with an exponential approach equation (Equation 5.16) shown with the black solid lines with $\chi^2 > 0.99$

The TGA results imply that the mercerized cotton possesses a higher thermostability than the raw cotton samples. Associated with the results of XRD (Figure 2.1) and composition analysis (Table 5.1), the reasons could be the presence of cellulose II in MCY-raw which is more thermally stable than cellulose I [188, 190], the only cellulose crystalline structure in NY-raw; and that the removal of hemicellulose by the mercerization process of MCY-raw shifted the decomposition temperature to a higher value, as the decomposition temperature of hemicellulose is reported to be lower than that cellulose and lignin [231].

5.3.4 Determination of the pyrolysis activation energy

As to the determination of the pyrolysis activation energy, it is essential to choose the suitable modelling method. Here, two methods are compared regarding to their applicability and reliability on the two cotton samples, based on the conditions applied on the TGA measurements - the FOG method belonging to the model-fitting method, and the Friedman method, a model-free method or iso-conventional method. According to Equation 5.6 and Equation 5.8, both are dependent on the heating rate, β , and even though the heating rate was set to be a constant on the machine when measuring, in reality it might not be. So, it is essential to quantify the real heating rate during the measurement, therefore the instantaneous heating rate (β') is introduced and expressed with the equation below:

$$\beta' = \frac{T_n - T_{n-1}}{t_n - t_{n-1}} \quad \text{Equation 5.17}$$

where T_n , and T_{n-1} measure the n^{th} temperature and the $(n-1)^{\text{th}}$ temperature of the TGA measurement range, and t_n and t_{n-1} represent the corresponding time at each temperature, respectively.

How the instantaneous heating rate (β') changes with temperature for the two cotton samples, at different target heating rates, is shown in Figure 5.6.

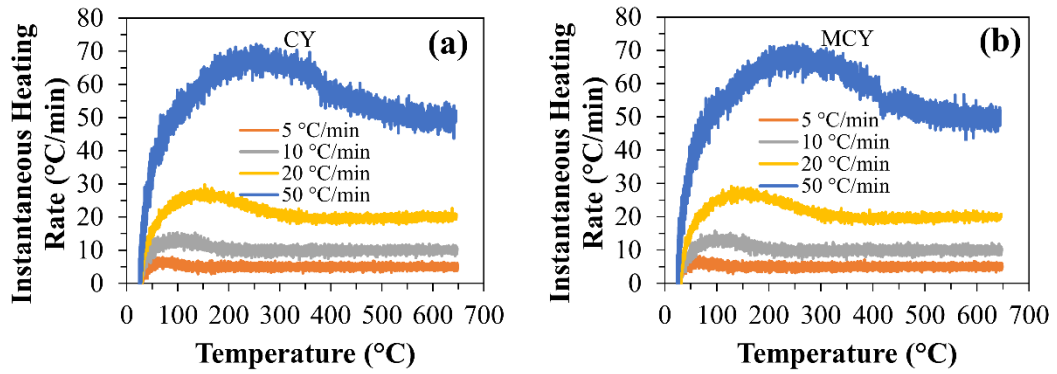


Figure 5.6 Dependence of the TGA instantaneous heating rate (β') on temperature for (a) the nature cotton yarn (CY) and (b) the mercerized cotton yarn (MCY), where the legends represent target heating rates set on the TGA machine

As shown in Figure 5.6, for both the CY and MCY samples, the instantaneous heating rates were not constant with temperature, and it firstly increased to a temperature higher than the target and then dropped down to a steady value – close to the target heating rate (β_t), which does not conform to the assumptions applied in the FOG and Friedman method. As the target heating rate increases, the temperature at which the β' turns over increased, e.g. for 5 $^{\circ}\text{C}/\text{min}$ the turn-over temperature is ca. 80 $^{\circ}\text{C}$, while as to 50 $^{\circ}\text{C}/\text{min}$ it becomes ca. 250 $^{\circ}\text{C}$. A larger fluctuation can be found at higher target heating rates, and this can be further proved from the results shown in Table 5.3, where the higher the β_t is, the larger the difference between the maximum instantaneous heating rate (β_i^{max}) and the minimum instantaneous heating rate (β_i^{min}) is, and for the β_t of 50 $^{\circ}\text{C}/\text{min}$ the difference is large as ca. 100 $^{\circ}\text{C}/\text{min}$.

Table 5.3 Statistical results of instantaneous heating rate for the NY-raw and the MCY-raw at different target heating rates set for TGA measurements

Sample	Target heating rate (β_t) (°C/min)	Average instantaneous heating rate ($\bar{\beta}_i$) (°C/min)	Maximum instantaneous heating rate (β_i^{max}) (°C/min)	Minimum instantaneous heating rate (β_i^{min}) (°C/min)
NY-raw	5.0	5.0 ± 0.1	7.9	0.2
	10.0	10.0 ± 0.1	15.3	0.3
	20.0	20.0 ± 0.1	29.1	0.1
	50.0	50.0 ± 0.3	98.8	0.3
MCY-raw	5.0	5.0 ± 0.1	8.1	0.8
	10.0	10.0 ± 0.1	15.7	0.3
	20.0	19.9 ± 0.1	29.1	0.2
	50.0	50.1 ± 0.3	100.9	0.3

$\bar{\beta}_i$ is calculated with Equation 5.18.

Recall Equation 5.7 for the Friedman method and Equation 5.8 for the FOG method. The former relies more on β' , as it is in a differential format depending on the instantaneous changing – the value of $\frac{d\gamma}{dt} = \frac{\beta d\gamma}{dT}$, but the latter relies on the average heating rate, $\bar{\beta}_i$, within the temperature range for the integration.

$\bar{\beta}_i$ is expressed as

$$\bar{\beta}_i = \frac{\sum_{j=1}^n \beta'(T_j)}{n} \quad \text{Equation 5.18}$$

where $\beta'(T_j)$ measures the instantaneous heating rate at temperature T_j .

Therefore, in our case - the temperature controlling ability of the TGA machine shown in Figure 5.6 – the FOG method is better to be used for analysing the pyrolysis behaviour of the two cotton samples. However, the reliability of the

approximations for the exponential term on the right-hand side of Equation 5.8 needs to be further proved, see Equation 5.10, Equation 5.11 and Equation 5.12.

To examine the discrepancy of the three approximations from the origin, the difference between them within the measuring temperature range is analysed, see Figure 5.7, where the difference, Δ , is calculated, according to the integration result of the left-hand side (I_L) and the right-hand side (I_R) of the comparison item shown in each plot in Figure 5.7, through the equation below:

$$\Delta = \frac{|I_L - I_R|}{I_L} \times 100\% \quad \text{Equation 5.19}$$

From the simulated results shown in Figure 5.7, the discrepancy decreases as the temperature increases until the temperature of the maximum decomposition rate ($T_m=619$ K (346 °C)) The values used for the simulation in Figure 5.7 come from ranges of the corresponding values for the cellulose pyrolysis reported in the literature These have been reported as 135 to 223 kJ/mol for the range of activation energy and 300 to 400 °C for the range of temperature at maximum decomposition rate, where the discrepancy reaches the lowest value in all the three cases, after that, the discrepancy bounces back and increases with temperature. This suggests that as the temperature gets close to T_m , the discrepancy is smaller and the more reliable is the approximation. In terms of different approximations, the discrepancy of the approximation in Equation 5.10 is very close to that in Equation 5.11, both at less than 2 %, and they are smaller than that in Equation 5.12 which could be as large as 300%. In order to decrease the discrepancy of the approximations

of the FOG method, and to improve the its reliability and applicability, the temperature ranges applied to the integrations shown in Equation 5.13, Equation 5.14 and Equation 5.15 need to be narrowed down to the temperature at the maximum decomposition rate, T_m .

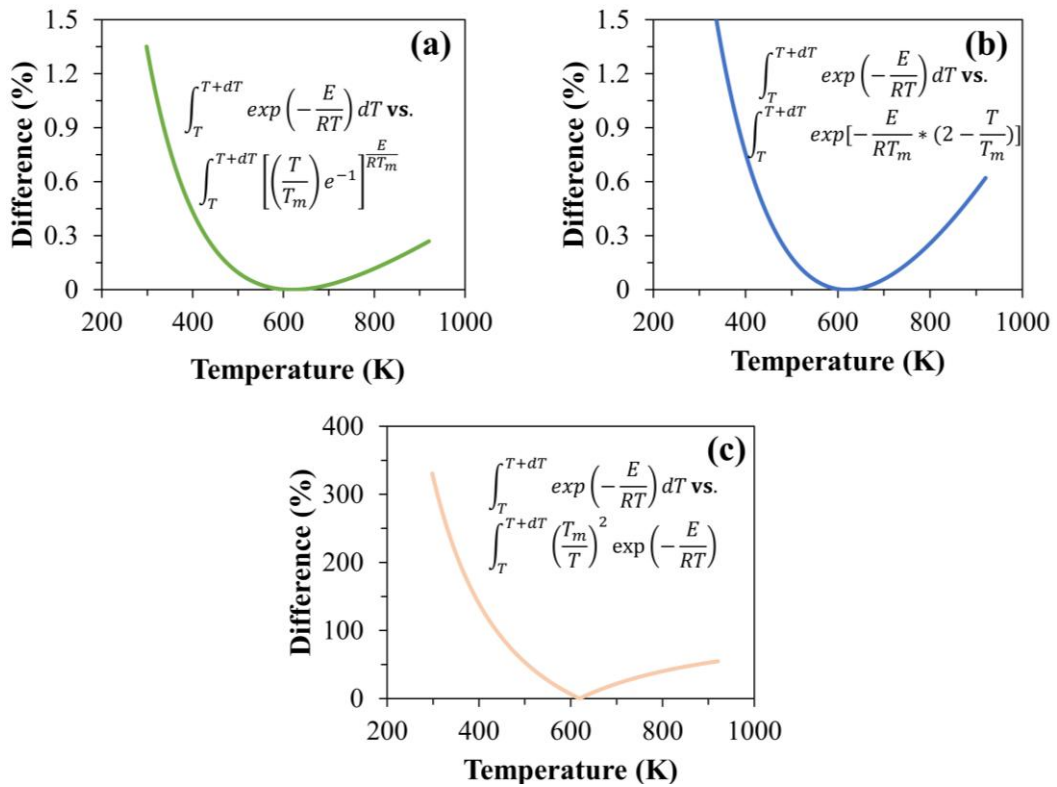


Figure 5.7 Discrepancy analysis of the approximations from the origin based on the first order global method (Equation 5.10, Equation 5.11 and Equation 5.12), with the computing parameters of E , T_m and R to be 200 kJ/mol, 619 K (346 °C) and 8.314 J/(K.mol), respectively

Therefore, the FOG method needs to be modified to overcome the large discrepancy caused by the wide temperature range. Here we develop a modified FOG method to get the pyrolysis activation energy by gradually narrowing the temperature range centred at T_m , which can be confirmed from the DTG plots in Figure 5.4, for $\ln T$, T and $\frac{1}{T}$ methods. A series of temperature

ranges are adapted in the approximations to calculate the pyrolysis activation energy with the method introduced in 5.2.6, for each sample at each target heating rate, and the dependence of pyrolysis activation energy as a function of the temperature range can be obtained, after which the tendency is used for further analysis. A practical example of how to get the pyrolysis activation energy for NY-raw at the heating rate of 50 °C/min is shown in Figure 5.8. The pyrolysis activation energy can be obtained as follows. To begin, a series of temperature range for the integration of each of the three equations, Equation 5.13, Equation 5.14 and Equation 5.15, is chosen to be $\pm 10\%$, $\pm 5\%$, $\pm 3\%$ and $\pm 1\%$ of T_m . Then, in order to get the pyrolysis activation energy from different approximations, a linear fitting is applied to each plot of $\ln(\ln(1/y))$ vs. the temperature item, $\ln(T)$ for Equation 5.13, T for Equation 5.14 and $1000/T$ for Equation 5.15, for every temperature range, see the dot lines in Figure 5.8; the gradient of each line can be measured with the LINEST regression function in EXCEL.

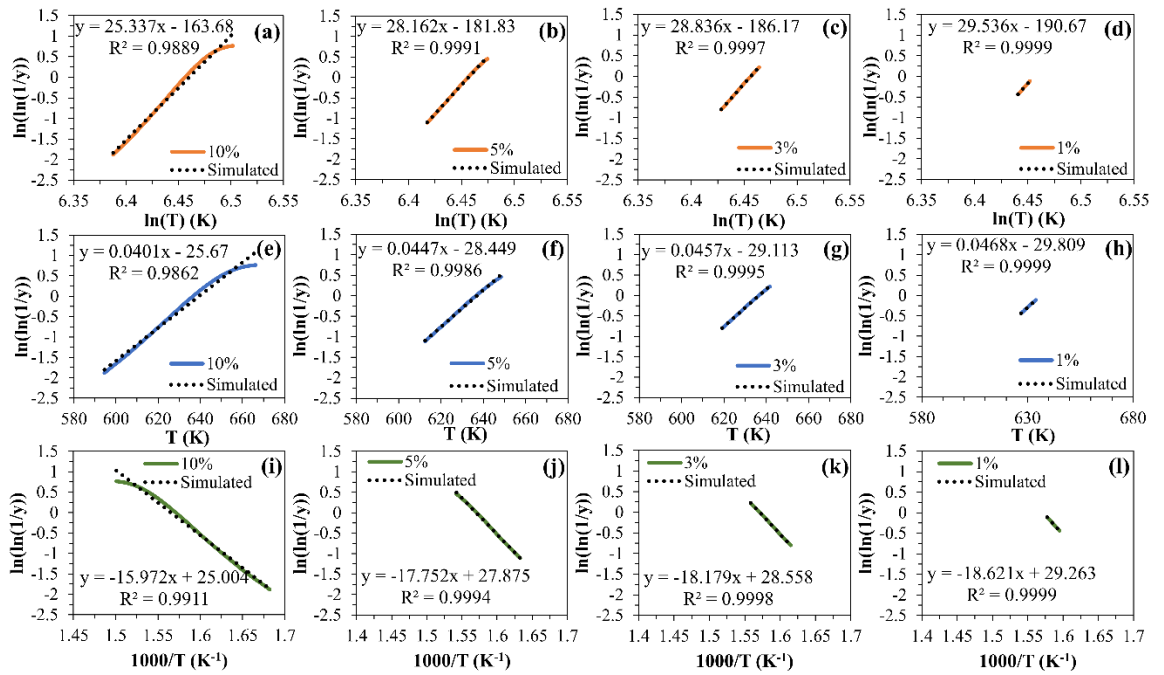


Figure 5.8 Plots of $\ln(\ln(1/y))$ as a function of $\ln(T)$ within the temperature ranges of (a) $\pm 10\%$, (b) $\pm 5\%$, (c) $\pm 3\%$ and (d) $\pm 1\%$ of the temperature of the maximum decomposition speed (T_m), based on Equation 5.13; $\ln(\ln(1/y))$ as a function of T within the temperature ranges of (e) $\pm 10\%$, (f) $\pm 5\%$, (g) $\pm 3\%$ and (h) $\pm 1\%$ of the T_m , based on Equation 5.14; $\ln(\ln(1/y))$ as a function of T within the temperature ranges of (i) $\pm 10\%$, (j) $\pm 5\%$, (k) $\pm 3\%$ and (l) $\pm 1\%$ of the T_m , based on Equation 5.15, and all the data are for the natural cotton yarn measured with the target heating rate of $50\text{ }^\circ\text{C}/\text{min}$

Recall the method introduced in section 5.2.6, the pyrolysis activation energy associated with the temperature range and approximation is calculated with the equations below:

$$E_{\ln T}^i = (G_{\ln T}^i - 1) \times RT_m \quad \text{Equation 5.20}$$

$$E_T^i = G_T^i \times RT_m^2 \quad \text{Equation 5.21}$$

$$E_{1/T}^i = -G_{1/T}^i \times R \quad \text{Equation 5.22}$$

where G_{lnT}^i , G_T^i and $G_{1/T}^i$ measure the gradients of the straight lines according to the Equation 5.13, Equation 5.14 and Equation 5.15 respectively, and correspondingly E_{lnT}^i , E_T^i and $E_{1/T}^i$ represent the pyrolysis activation energy; the superscript i means one of the temperature ranges from $\pm 10\%$, $\pm 5\%$, $\pm 3\%$ and $\pm 1\%$. The dependence of the pyrolysis activation energy as a function of the temperature range at different target heating rates is shown in Figure 5.9. These results indicate that the pyrolysis activation energy increased as the temperature range decreased, e.g. for the of NY-raw, it increased from 119.0 ± 0.5 kJ/mol to 143.0 ± 0.1 kJ/mol when the temperature range decreased from $\pm 10\%$ to $\pm 1\%$ at the target heating rate of $5\text{ }^\circ\text{C}/\text{min}$ (the dataset in orange in Figure 5.9(a)). Recall, the difference between the approximation and the origin decreases as the temperature range decreases, see Figure 5.7. Therefore, we develop a method to determine the pyrolysis activation energy when the temperature range is in the limit zero, and hereafter it is called the intrinsic pyrolysis activation energy ($[E]$), as follows. First, by examination, the quadratic equation was found to adequately match the dependence of pyrolysis activation energy as a function of temperature range with the determination coefficient $\chi^2 > 0.99$, shown in Figure 5.9; by extrapolating the temperature range to zero, at which the difference between the approximation and origin reaches the smallest, corresponding to the

lowest points of Figure 5.7, the intrinsic pyrolysis activation energy was confirmed to be the constant item of the quadratic fitting line, using the advanced LINEST regression function in EXCEL.

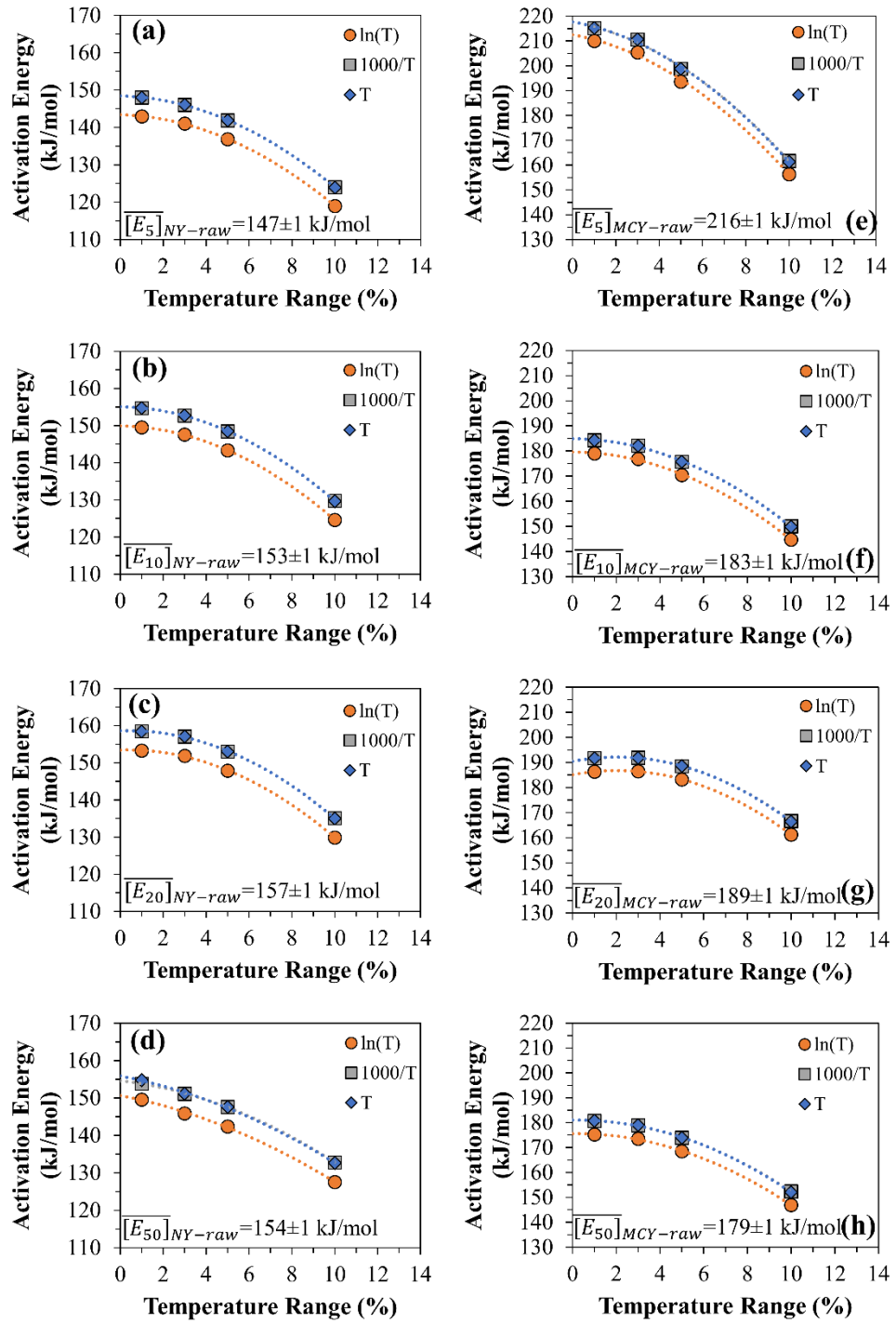


Figure 5.9 Pyrolysis activation energy dependence on temperature range applied for the integration, where (a)-(d) are for the natural cotton yarn(NY-raw) measured at the target heating rate of 5, 10, 20 and 50 °C/min respectively, and (e)-(h) are for the mercerized cotton yarn (MCY-raw) measured at different target heating rates of 5, 10, 20 and 50 °C/min, respectively. The dot lines are quadratic fitting results with

$$\chi^2 > 0.99$$

The results in Figure 5.9 are further tabulated in Table 5.4, indicating that there is not much difference in the intrinsic pyrolysis activation energy among the three approximations when the measurement was conducted under the same target heating rate (β_t), giving an average intrinsic pyrolysis activation energy, $\overline{[E_{\beta_t}]}$, to be confirmed for each β_t . An independence of $\overline{[E_{\beta_t}]}$ on β_t is found on both the NY-raw and the MCY-raw samples, and the former has a lower $\overline{[E_{\beta_t}]}$ than the later at each β_t .

Table 5.4 Activation energy for the pyrolysis of NY-raw and MCY-raw calculated from the results in Figure 5.9

Sample	Target heating rate β_t (°C/min)	Approx.*	Intrinsic pyrolysis activation energy $[E_{\beta_t}]$ (kJ/mol)	Average intrinsic pyrolysis activation energy $\overline{[E_{\beta_t}]}$ (kJ/mol)
NY-raw	5	ln(T)	143.4 ± 0.3	147 ± 1
		1000/T	148.5 ± 0.3	
		T	148.4 ± 0.3	
	10	ln(T)	149.9 ± 0.2	153 ± 1
		1000/T	155.1 ± 0.2	
		T	155.1 ± 0.2	
	20	ln(T)	153.4 ± 0.4	157 ± 1
		1000/T	158.7 ± 0.4	
		T	158.6 ± 0.4	
	50	ln(T)	150.7 ± 0.7	154 ± 1
		1000/T	154.6 ± 0.2	
		T	155.9 ± 0.7	
MCY-raw	5	ln(T)	212 ± 2	216 ± 1
		1000/T	218 ± 2	
		T	218 ± 2	
	10	ln(T)	179.6 ± 0.9	183 ± 1
		1000/T	184.9 ± 0.9	
		T	184.9 ± 0.9	
	20	ln(T)	185.1 ± 0.1	189 ± 1
		1000/T	190.5 ± 0.2	
		T	190.5 ± 0.1	
	50	ln(T)	160.3 ± 0.5	179 ± 1
		1000/T	165.8 ± 0.5	
		T	165.7 ± 0.6	

*ln(T), 1000/T and T represent the approximations expressed in Equation 5.10, Equation 5.11 and Equation 5.12, respectively.

To further analyse the dependence of $\overline{[E_{\beta_t}]}$ on sample and heating rate β_t , the plot of $[E_{\beta_t}]$ against β_t for both the cotton samples is conducted and shown in Figure 5.10. For the NY-raw sample, the $\overline{[E_{\beta_t}]}$ obtained at different β_t are very close to each other, suggesting its independence on β_t and giving a mean value of the average intrinsic pyrolysis activation energy, $\overline{[E]}_{NY-raw}$, to be 153 ± 2 kJ/mol, see the solid green circles and the green line in Figure 5.10. As for the MCY-raw sample, a similar phenomenon is found that its $\overline{[E_{\beta_t}]}$ shows independence on β_t , therefore its mean value of the average intrinsic pyrolysis activation energy was calculated to be $\overline{[E]}_{MCY-raw} = 191 \pm 7$ kJ/mol. This independence of pyrolysis activation energy on β_t proves the applicability and reliability of the modified FOG method to the samples under the conditions conducted for the TGA measurements in this study.

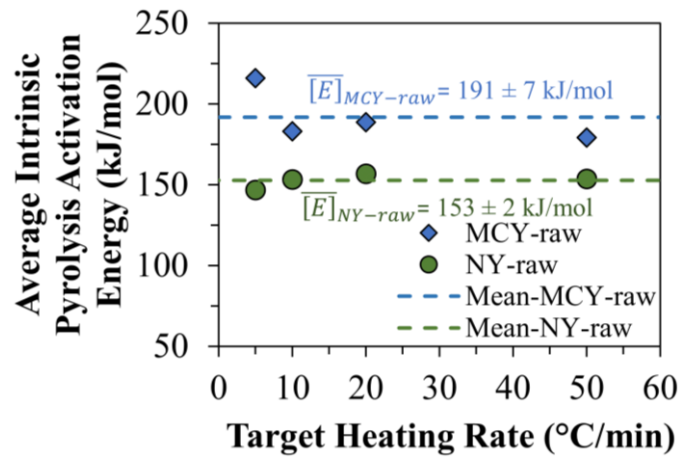


Figure 5.10 Plot of average intrinsic pyrolysis activation energy ($\overline{[E_{\beta_t}]}$) vs. target heating rate (β_t) for the natural cotton yarn (NY-raw) and themergerized cotton yarn (MCY-raw), where the dash lines show the locations of the mean values ($\overline{[E]}_{NY-raw}$ and $\overline{[E]}_{MCY-raw}$), where some error bars are smaller than the symbols

Compared with NY-raw, MCY-raw has about 23% higher pyrolysis activation energy, and this result is consistent with the decomposition temperature analysis result shown in Figure 5.5, suggesting the mercerized cotton is more thermally stable compared to the raw cotton. The pyrolysis activation energy, $\overline{[E]}_{NY-raw}=153 \pm 2$ kJ/mol for the natural cotton yarn and $\overline{[E]}_{MCY-raw}=191 \pm 7$ kJ/mol for the mercerized cotton yarn, compares to the pyrolysis activation energy reported by Morgado, et al., at 158 kJ/mol and 187 kJ/mol for untreated cotton linters and mercerized cotton linters, respectively [210], and the pyrolysis activation energy of hemicellulose and lignin are reported to be within the range from 115 to 144 kJ/mol and from 23 to 108 kJ/mol, respectively [211]. In combination with the carbohydrate-compositional analysis and XRD results, the reasons for the difference in pyrolysis activation energy between NY-raw and MCY-raw are hypothesized: the existence of hemicellulose, with lower pyrolysis activation energy than cellulose, in the NY-raw sample shifted the apparent pyrolysis activation energy to a lower value; and the thermal stability of cellulose II existing in MCY-raw is higher than that of cellulose I, the only cellulose crystalline structure in NY-raw. Besides, even though the molecular weight of NY-raw is higher than that of MCY-raw, the thermal stability of NY-raw is worse than that of MCY-raw, with lower decomposition temperature and pyrolysis activation energy, suggesting that the molecular weight plays minor role in the thermal stability of cellulose-base materials, while the carbohydrate composition and crystalline structure dominate, when non-cellulose lignocellulose materials existing, i.e. hemicellulose and lignin. In contrast, in terms of dissolution activation energy, the MCY-raw, with lower molecular weight has higher dissolution activation energy than NY-raw, suggesting that molecular weight dominates the

dissolution kinetics other than the chemical composition, see detailed summary in Table 7.1.

5.4 Conclusions

The comparable properties of the two samples – NY-raw and MCY-raw, including morphology, chemical composition, molecular weight, dissolution behaviour in [C2mim][OAc], and thermal decomposition kinetics are investigated in this chapter. From the OM results, the shape of filaments in NY-raw samples was kidney-like, while for the MCY-raw samples, it shows round shape, in line with the findings from other papers. In terms of molecular weight, M_n and M_w , the NY-raw is about 2.5 times higher than MCY-raw, and there was no detectable amount of hemicellulose found in MCY-raw from the chemical composition test on the two samples. The existence of cellulose II region was confirmed in the MCY-raw via WAXD measurements, which was not detected in NY-raw. The above results are attributed to the mercerization process and in line with the findings in literature.

As to the dissolution kinetics, the dissolution activation energy of NY-raw in [C2mim][OAc] is higher than that of MCY-raw, and this is due to the difference in either molecular weight or the carbohydrate composition between the two samples, which could be verified in the future by mercerizing the NY-raw sample and measuring the dissolution activation energy as a function of its molecular weight, as what the other researchers have done on cellulose materials with NaOH/urea aqueous solution [222]. In the matter of thermal decomposition behaviour, TGA was conducted on the two cotton samples, whose results suggest that the decomposition temperature is dependent on

heating rate, showing an exponential approach tendency with $\chi^2 > 0.99$. In order to confirm $[T_m]$ with zero heating rate, a method was successfully developed by extrapolating the heating rate to be zero where the corresponding value on y axis is the $[T_m]$, giving that of NY-raw and MCY-raw to be 317 ± 3 °C and 346 ± 6 °C, respectively.

According to the analysis of the effect of instantaneous heating rate on the Friedman method and FOG method, FOG method was found to be more reliable and applicable in our case, and a modified FOG method was developed and effectively applied to calculate $[E_{\beta_t}]$ by narrowing the integration temperature range. $[E_{\beta_t}]$ is found to be independent on β_t , resulting in $\overline{[E]}_{NY-raw}$ and $\overline{[E]}_{MCY-raw}$ to be confirmed as 153 ± 2 kJ/mol and 191 ± 7 kJ/mol, respectively. All the TGA analysis suggests that MCY-raw is more thermally stable than NY-raw, as a result of the low-thermal-stable hemicellulose only detected in NY-raw and the cellulose II formed upon the mercerization process of MCY-raw.

The findings in this chapter could be instructive to the researchers conducting studies on the effect of processing progress such as mercerization and bleaching process on other cellulose-based materials, and suggest a prospective research plan to verify the hypothesized reasons for the difference in dissolution and pyrolysis behaviour mentioned above, by mercerizing the NY-raw sample. Besides, the thermal stability measurement results will instruct the choice of cotton sample for the fabrication of all cellulose composites in the later chapter.

Chapter 6 Fabrication of all cellulose composites from the mercerized cotton

6.1 Introduction

An all cellulose composite (ACC) is a mono-component composite where both the reinforcement phase and the matrix phase are comprised of cellulose. There are two key processing methods in the literature for the manufacture of ACC's, a one-step method and a two-step method, and they are classified according to if the matrix phase is separately prepared from a fully dissolved cellulose solution (two-step), or if the matrix phase is produced from partially dissolved cellulose from the surfaces of the reinforcement phase itself (one-step) [4, 232, 233].

In terms of the fabrication of all cellulose composites using the one-step method (partial dissolving method), there have been several papers reported in the literature [155, 233-235]. However, most of them are more suitable for batch processing, as the reported process is potentially difficult to be applied as a continuous-fabricating process, which is mostly restricted by the requirement of simultaneously hot-pressing and dissolving the samples. Therefore, the fabrication efficiency and the size of the sample could be limited.

In this chapter, a new technique, based on the one-step method, is introduced to fabricate two-layer all cellulose composites from mercerized cotton plain fabrics using [C2mim][OAc], where the effect of process conditions, such as pressure, pressing time and number of pressing steps, on the tensile strength,

Young's modulus and peel strength are investigated. The scale-up potential of the new method used as a continuous process is discussed and proposed.

6.2 Methods

6.2.1 Preparation of all cellulose composites from fabrics woven from the mercerized cotton yarn

A basket weave plain fabric was hand woven from the mercerized cotton yarn (the same fibre as investigated in Chapter 4), hereafter called MCYF and used to make all cellulose composites, where a pair of weft threads is passed over and under a pair warp threads – a simple variation of plain weave as shown in Figure 6.1(a)). The fabric comprised 13 threads/cm in the warp direction (align with y axis) and 70 threads/cm in the weft direction leading to a weft/warp thread count ratio of 5.4 (see Figure 6.1(b)). The fabric area density was measured to be of 334 grams per square metre (GSM).

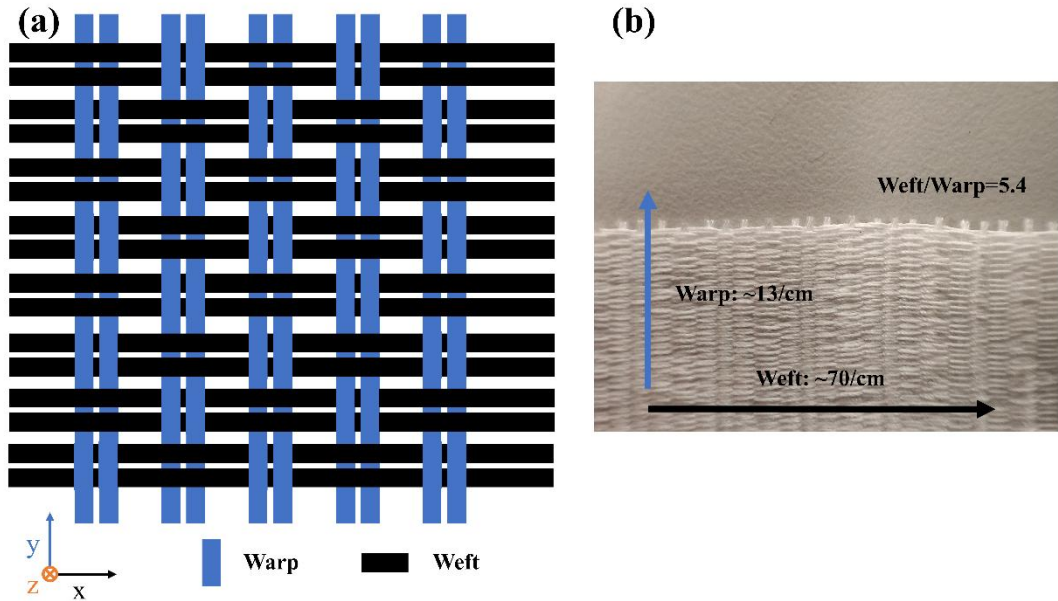


Figure 6.1(a) Schematic graph of the basket weave with a coordinate shown at the right bottom and (b) photograph of the basket MCY-woven fabric applied for the fabrication of all cellulose composites in this chapter, where the warp and weft are in line with y axis and x axis, respectively

ACCs were made with two layers of $50 * 50 \text{ mm}^2$ -sized MCYF using [C2mim][OAc] as the solvent through the following steps. First, two layers of cut MCYF samples were immersed in [C2mim][OAc] contained in the same Teflon dish, where the [C2mim][OAc] had been preheated at $40 \text{ }^\circ\text{C}$ for 1 hour. The solid to solvent ratio was controlled to be 1 to 40, such that [C2mim][OAc] exceeded the critical amount [179] needed for a full dissolution of the cellulose samples. The conditions applied for the dissolving process is confirmed from the dissolution master curve of MCY, and this will be discussed in detail later. Next, the submerged cloth layers in the [C2mim][OAc] were put into a vacuum oven for partially dissolving, of which the dissolving conditions will be confirmed later in Section 6.3.1; then these processed MCYF samples were taken out from the [C2mim][OAc] bath and transferred to an aluminium- mould

(dimensions also 50 mm * 50 mm) and then pressed together using a hot-press machine for a certain chosen pressure and for a certain chosen of time at room temperature. After this consolidation stage the pressed samples were transferred to a water bath to coagulate the dissolved cellulose, and left under running tap water to remove any residual [C2mim][OAc] in the samples for 24 hours. Finally, a drying process followed, using the hot-press machine again but this time set to a temperature of 120 °C and using a pressure of 1MPa for 1 hour. To prevent adhesion between the samples and the mould, Teflon films were put on the top and bottom of the two-layer MCYF samples during the consolidation process. The fabrication process is presented schematically in Figure 6.2. Samples were made to assess the effect of the following variables on ACC mechanical properties. The alignment of the two layers (unidirectional with the warp and weft aligned and alternating, termed 90/0), the consolidation pressure (0.2MPa, 1MPa, 2MPa and 4MPa), the number of consolidation stages (single stage and two stages) and the total consolidation time (1 min and 2 min). Two samples were prepared for each condition. All the samples were stored at room temperature with a relative humidity of ca. 50 % for over 48 hours before any mechanical test.

The ACC made under different conditions are named as follows (see Table 6.1 for a summary): for those with unidirectional alignment, Uni or 90/0 -a(b) or/and -c(d), where Uni and 90/0 stand for the unidirectional alignment and 90/0 alignment respectively, and a(b) means the first processing step is @ 'a' MPa for time of 'b' min, and if available the second processing step is @ 'c' MPa for time of 'd' min. For example, Uni-0.2(1)-2(1) means the alignment of

the two layers of fabrics are unidirectional, and they are processed @ 0.2MPa for 1 min followed by a second processing step @ 2MPa for 1 min.

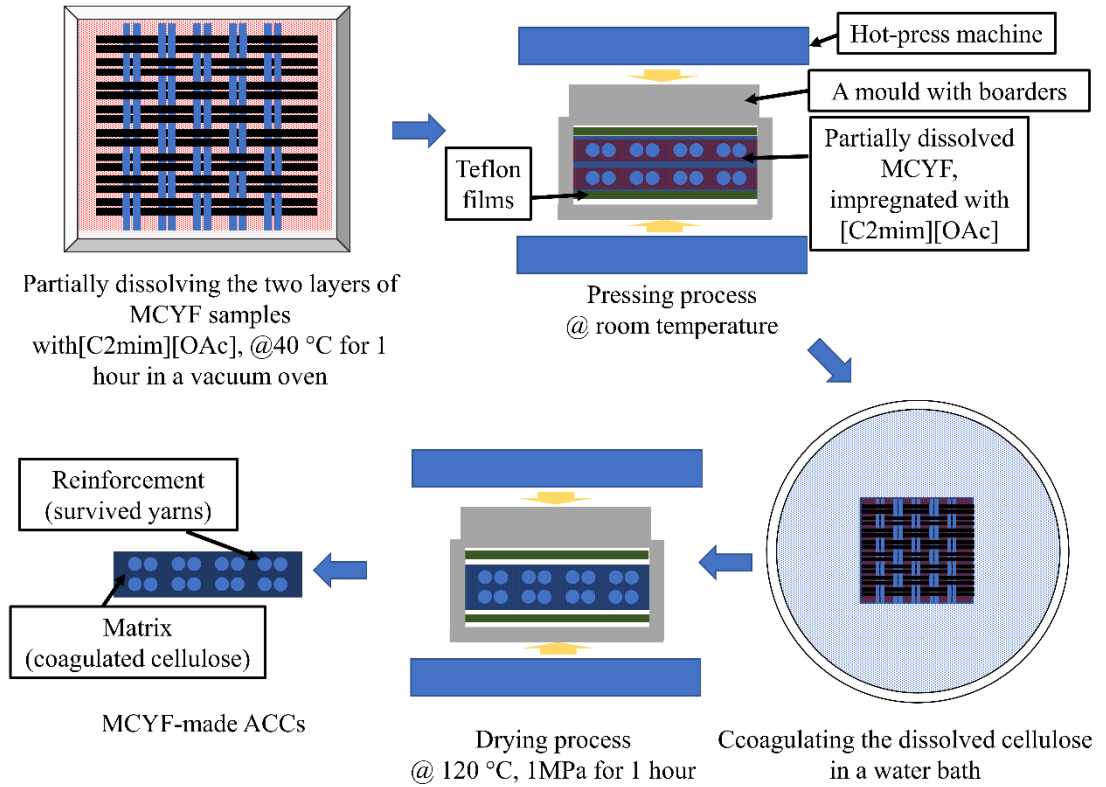


Figure 6.2 Fabrication procedure of two-layer all cellulose composites out of mercerized cotton yarn-woven fabrics (MCYF)

Table 6.1 Nomenclature of ACC and the corresponding processing conditions

Sample	Number of processing stage	Processing conditions	Alignment of the two layers of fabrics
Uni-0.2(1)	1	0.2 MPa for 1 min @100 °C	unidirectional
Uni-1(1)	1	1 MPa for 1 min @100 °C	unidirectional
Uni-2(1)	1	2 MPa for 1 min @100 °C	unidirectional
Uni-4(1)	1	4 MPa for 1 min @100 °C	unidirectional
Uni-2(2)	1	4 MPa for 2 min @100 °C	unidirectional
Uni-0.2(1)-2(1)	2	0.2 MPa for 1 min plus 2 MPa for 1 min @100 °C	unidirectional
0/90-2(1)	1	2 MPa for 1 min @100 °C	90/0

6.2.2 Optical microscopy

Optical Microscopy in reflection mode was used to investigate cross-section morphology of the manufactured all cellulose composites, and the sample preparation for optical microscopy followed that previously described in section 2.2.1.

6.2.3 Tensile test and peel test

The tensile properties of ACCs were measured using an Instron tensile machine with a 2000 N load cell at a displacement rate of 10 mm/min. The extension came from the movement of two clamps, and the tensile force was loaded on the sample which is in line with the weft direction of the specimen. The tensile strength is defined as the tensile stress, σ , at break in this study,

which is calculated as the ratio of the force at break, F , to the initial cross-section area of the specimen, S , and calculated by the equation:

$$\sigma = \frac{F}{S} \quad \text{Equation 6.1}$$

where the cross-section area, A , is calculated by the equation below:

$$S = W * d \quad \text{Equation 6.2}$$

where W and d measure the width and thickness of the specimen, respectively.

The strain, ε , which measures the deformation during the stretching test is calculated with the change in length, Δl , and the original length, l_o , along the stretching direction via the equation:

$$\varepsilon = \frac{\Delta l}{l_o} \quad \text{Equation 6.3}$$

The original length l_o is set as the distance between the two clamps, which is usually called the gauge length. For each sample, three specimens with width of about 5 mm were used, and the gauge length was kept to be about 25 mm which makes the ratio width/gauge length to be about 1:5. The Young's modulus, G' , was calculated from the initial linear region of the stress-strain curve, where the elastic deformation dominated, by the equation:

$$G' = \frac{\Delta\sigma_e}{\Delta\varepsilon_e} \quad \text{Equation 6.4}$$

where $\Delta\sigma_e$ and $\Delta\varepsilon_e$ stand for the changes in stress and strain during the elastic deformation region, respectively. Finally, the average value and the standard error of the three specimens were calculated and used.

As to the peel test, the same Instron machine was used as for tensile test with a load cell of 2000 N. For each sample, two specimens with width of ca. 1 cm and length of ca. 6 cm were applied. The peel strength, P , is defined as the average load per unit width required to separate bonded materials where the loading force is 180 degrees to the separation progressing direction. It can be then calculated as the equation:

$$P = \frac{\bar{F}}{W} \quad \text{Equation 6.5}$$

Where \bar{F} , and W measure the average load during the peeling process and the sample width. Two specimens are tested for each sample, and the mean and standard error were again calculated. Both tensile test and peel test were conducted at room temperature with a relative humidity of ca. 50 %.

6.3 Results and discussion

6.3.1 Determination of the conditions for dissolving the MCYF samples

In order to estimate the minimum amount of cellulose needed to be selectively dissolved to fill all gaps between adjacent yarns, which contributes to the

matrix phase in the final ACCs, a schematic image is proposed as shown in Figure 6.3.

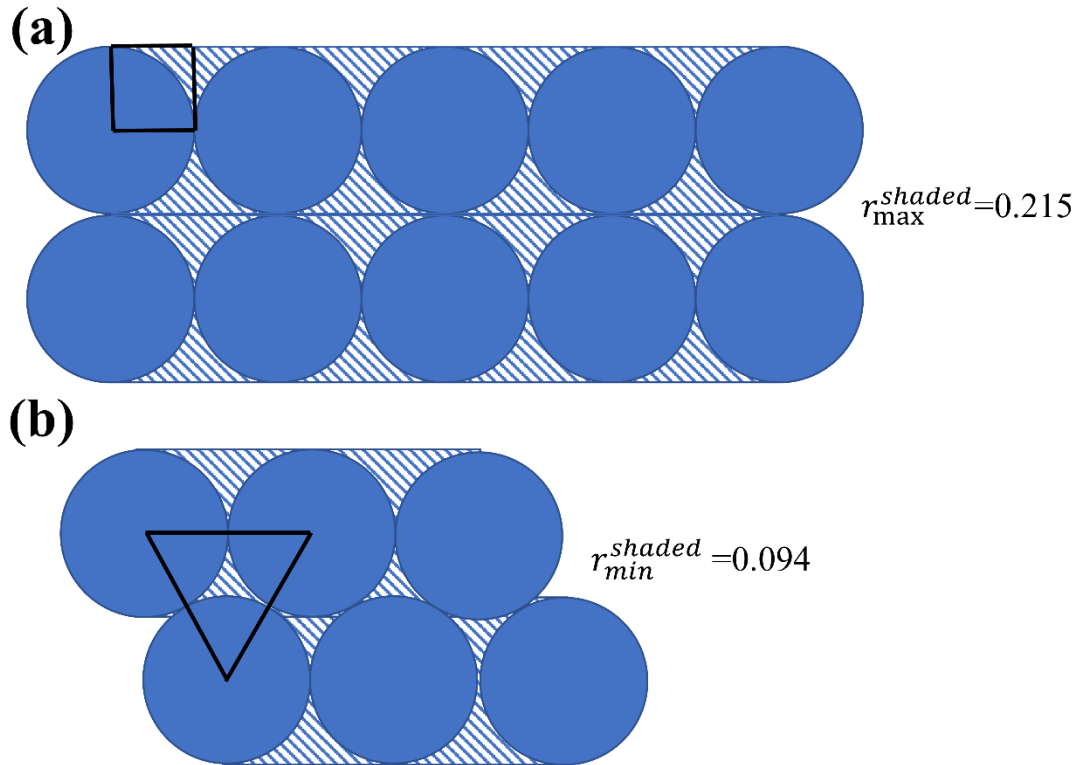


Figure 6.3 Schematic images illustrating the amount of cellulose needed to be dissolved to make enough matrix in ACCs, which is denoted by the shaded area in two ideal scenarios of alignment between two cotton fabrics: (a) the maximum and (b) the minimum, where the matrix volume fractions are represented by the shaded areas in the rectangular and triangular areas, and they are labelled to be r_{max}^{shaded}

and r_{min}^{shaded} , respectively

Figure 6.3 shows two possible packing scenarios for adjacent cotton fabrics layers, which are used to estimate the required matrix volume fraction, where only the closely packed weft threads are considered as they are in the majority, with the ratio of weft to warp to be about 5.4. The matrix fractions in the two cases, the maximum (r_{max}^{shaded}) and the minimum (r_{min}^{shaded}), are

calculated as the shaded areas involved the rectangular (Figure 6.3(a)) and triangular (Figure 6.3(b)) areas, respectively.

In order to make sure that there is enough partially dissolved matrix to fill all the gaps between the adjacent woven layers, then we choose the worst case scenario which is that at least 21.5% of MCYF needs to be dissolved. In practice, it is safer if we dissolve slightly more than this amount, then during the consolidation process, any excess matrix will be expelled (and will be seen as 'flash' outside the woven composite layers), and the composite will then contain the 'optimum' matrix fraction. If we see this 'flash' on the final produced ACC then we can conclude we have sufficient dissolved matrix.

In order to dissolve enough cellulose to make sure we have more than 21.5% and to produce the 'flash' (which we take as evidence of dissolved cellulose filling all the gaps between the two woven layers) - we decided to dissolve twice as much this limit, ca. 40% of the MCYF. Recall the master curve at 40 °C in Figure 4.9(c) for the same fibre, the coagulation fraction of 40% corresponds to the dissolution process carried out at 40 °C for ca. 1 hour. This is a relatively low temperature, compared with over 90 °C reported by most other papers [3, 139, 142, 156], and appropriate length of time which could ensure high efficiency and ease to control. As a result, the processing conditions for dissolution is confirmed as 40 °C for ca. 1 hour, which has been applied to all the fabrication of ACCs mentioned in this thesis. Here, an example of the appearance of Uni-0.2(1)-2(1) is shown in Figure 6.4, where on both images, one for its damp sample upon the coagulating process and another for its dried sample upon the drying process, flash was found, which is pointed at by the blue arrows. We take the presence of the flash as evidence

that we have achieved the optimum amount of dissolved and coagulated matrix fraction inside the ACC for this weave style.

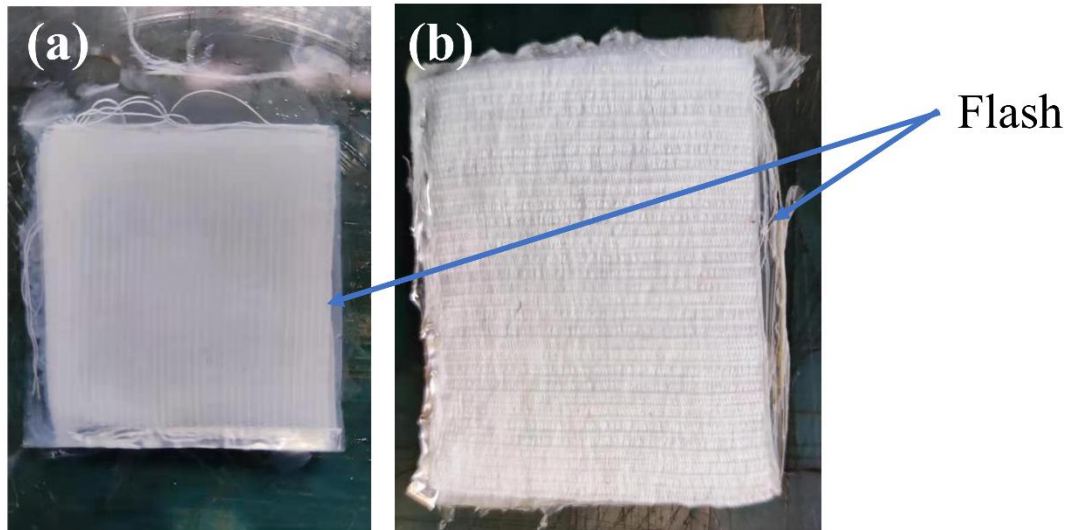


Figure 6.4 Appearance of Uni-0.2(1)-2(1) (a) when it was soaking in the water bath upon coagulation and (b) it was dried, with the flash cellulose indicated by the blue arrows

6.3.2 Microscopy results

Optical microscopy was used to study the cross sections of the ACC samples made under different processing conditions, see Figure 6.5.

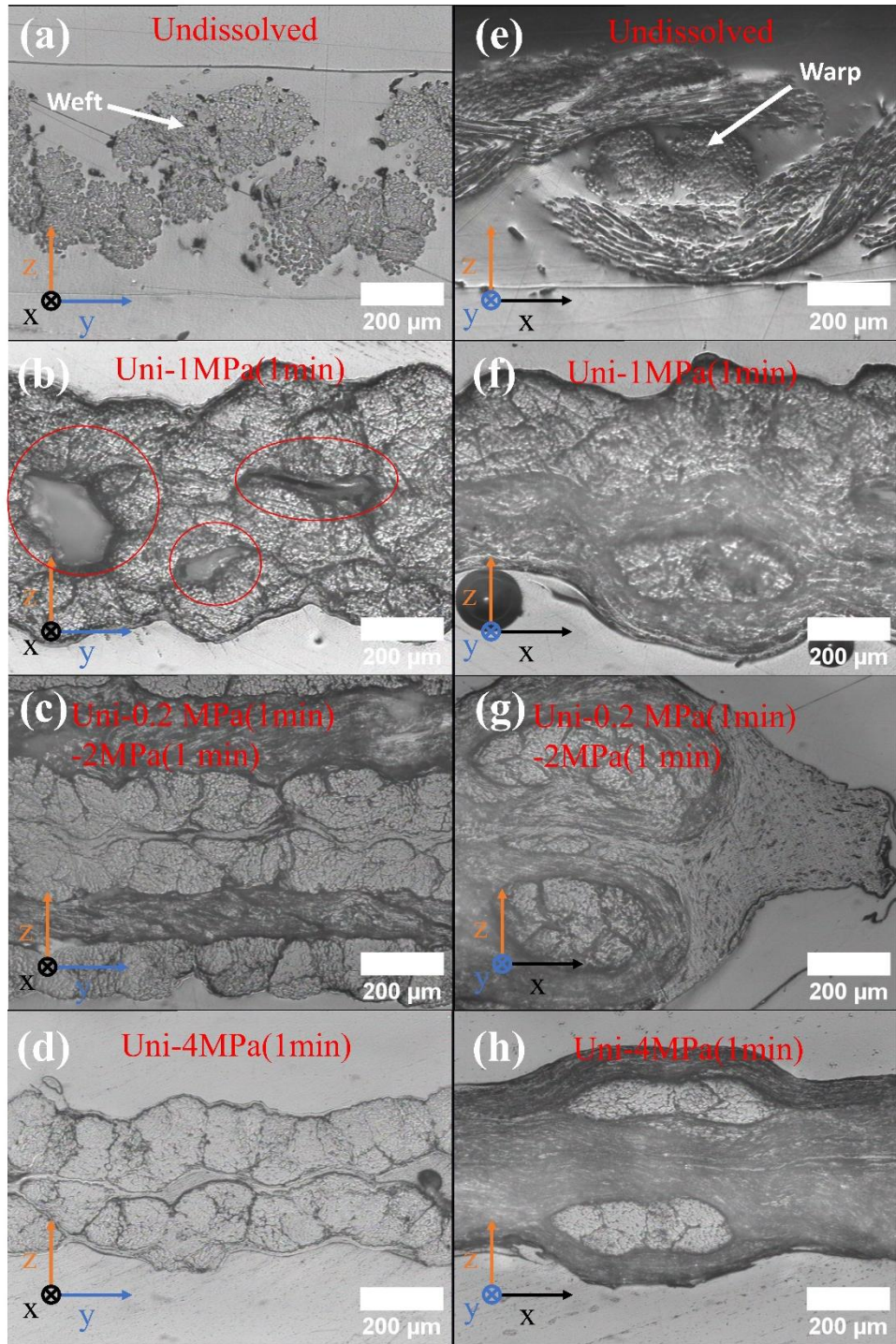


Figure 6.5 Cross-section images of (a) (e) single layer of the raw MCYF, (b) and (f) show Uni-1(1), (c) and (g) Uni-0.2(1)-2(1) and (d) and (h) Uni-4(1), where in (a)-(d) the axis of wefts, denoted by x, is perpendicular to the plane of cross section, while in (e)-(h) the axis of warps, represented by y, is perpendicular to the plane of cross section; and visible defects/air gaps are shown with red ellipses in (b). Recall Table

6.1 for nomenclature

Compared with the raw mercerized cotton yarn fabric (MCYF-raw), MCY weft fibres were merged together upon the dissolving process, see Figure 6.5(a)-(d). For the raw cloth, the fibres are not bonded together and so they move away from each other during the epoxy encapsulation process for sample preparation. Once there is some dissolved and coagulated matrix this no longer occurs. The visible remaining MCY fibres indicate that the MCY was partially dissolved/selectively dissolved from its outside, which is in line with the OM results on single MCY, see Figure 4.7, where the dissolution started from the exterior of the MCY and moves into the central core region, resulting in non-visible dissolved cellulose able to be observed in the central region.

Figure 6.5(b) shows that there were lots of air gaps between the two layers of fabrics, circled in red, found when using a lower consolidation pressure and a short consolidation time (in Uni-1(1)), suggesting there is not enough matrix, or poor consolidation. Alternatively, there were no visible internal voids when using either a two-stage process (0.2MPa for 1 minute followed by 2MPa for 1 minute, Uni-0.2(1)-2(1)) or a single stage at a higher pressure (Uni-4(1)). Figures (c) and (d) in particular show a nice layer of dissolved and coagulated matrix between the woven layers suggesting good composite manufacture. The results indicate that with the processing pressure increase from 1 MPa to 4 MPa, the internal voiding is decreased as so we will expect improved mechanical properties and interlayer peel strength. How the number of processing stages influences the bonding property remains unclear and therefore needs further measurement, such as peel test which will be discussed later.

As the pressure applied during the fabricating process was increased from 1 MPa (Figure 6.5(f)) to 4 MPa (Figure 6.5(h)), the flatness of warps increased, and compared with MCYF-raw in Figure 6.5 (e), the gaps between filaments comprising the yarns disappeared upon the fabricating process. This finding is also consistent with the analysis results on the microscopic images of mercerized cotton yarns shown in Figure 4.7. Cellulose flash was observed on Uni-0.2(1)-2(1), which is caused by excessive dissolved cellulose filling the gaps between the two layers, see Figure 6.5(g), which indicates sufficient cellulose has dissolved to form the matrix phase under the processing condition of 40 °C, 1 hour.

6.3.3 Mechanical properties

Tensile test and peel test were carried out to measure the mechanical properties of the various ACCs, including tensile strength (Equation 6.2), Young's modulus (Equation 2.1) and peel strength (Equation 5.18), to explore the effect of different fabricating conditions. Their results are shown in Figure 6.6, Figure 6.7 and Figure 6.8.

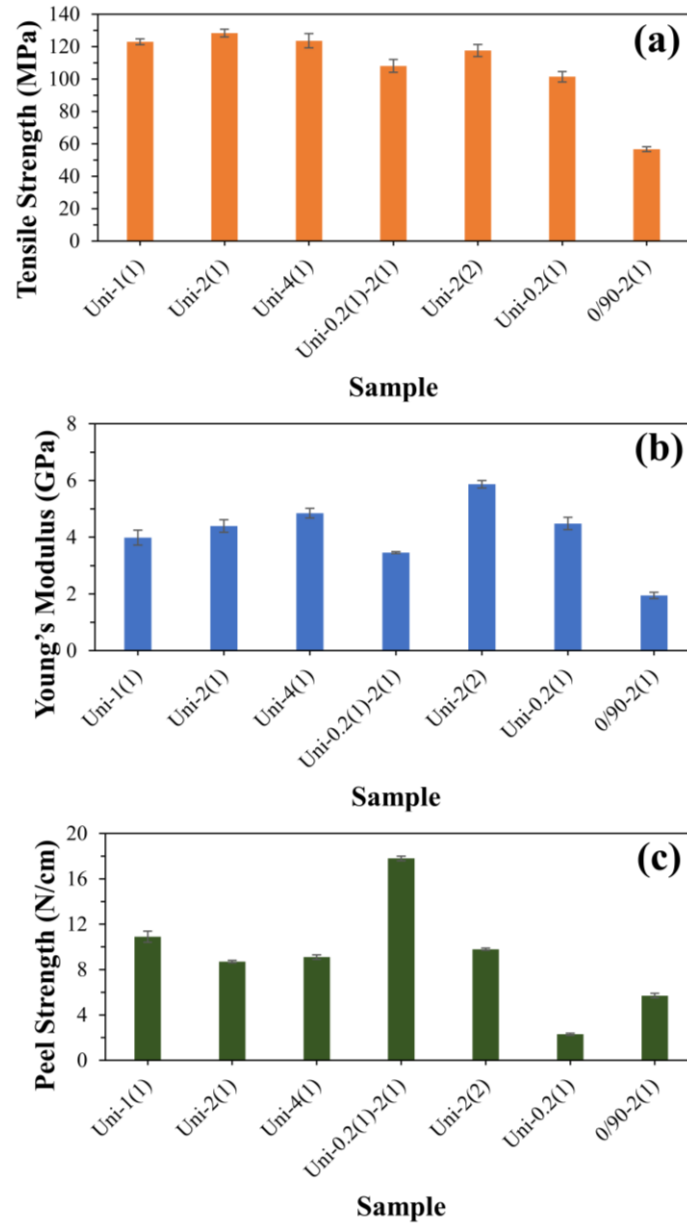


Figure 6.6 Mechanical properties of ACCs, including (a) tensile strength, (b) Young's modulus and (c) peel strength, see Table 6.1 for nomenclature

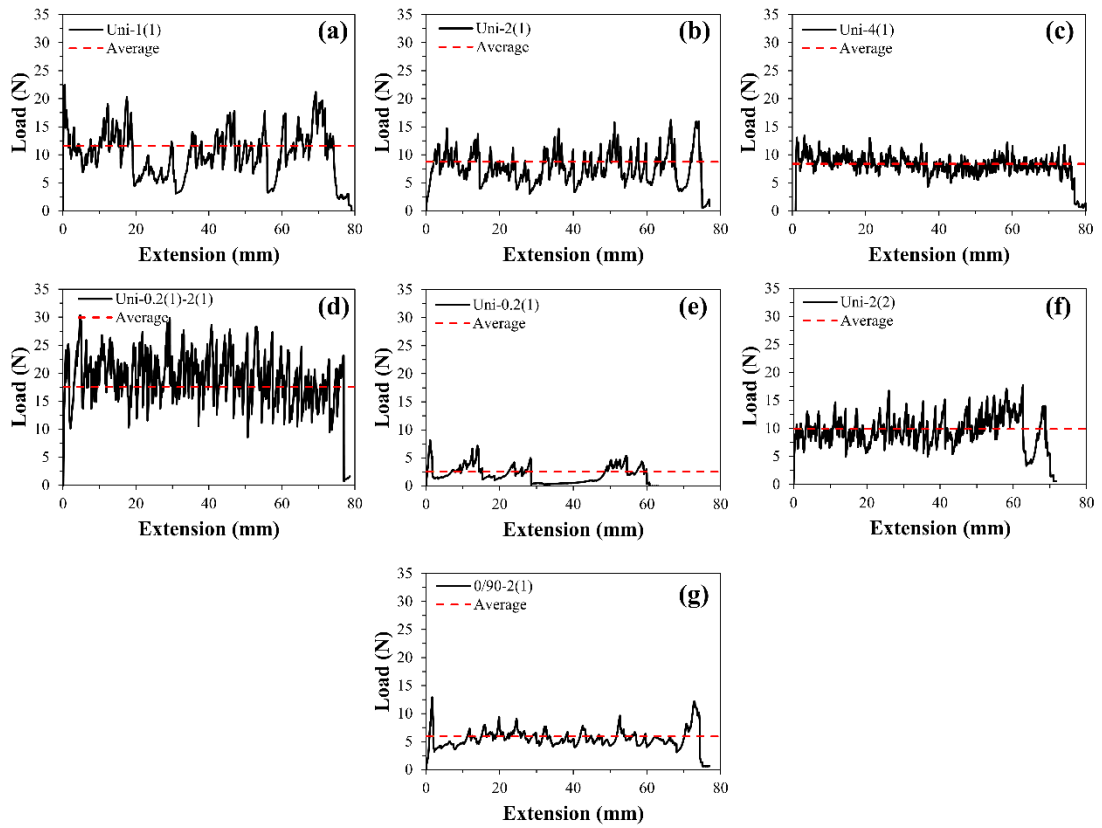


Figure 6.7 Peel test curves of load as a function of extension of ACCs, where the average load is denoted with the red dash line and recall Table 6.1 for nomenclature

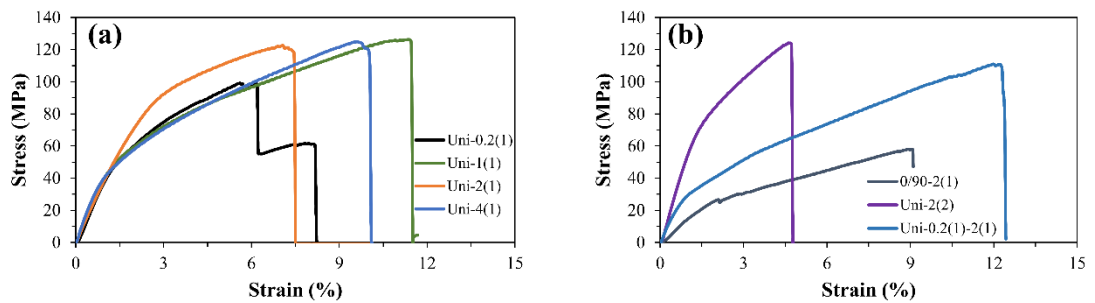


Figure 6.8 Stress-strain curves of different ACCs from tensile test along the weft direction

Figure 6.6 shows that, compared with the sample with 0/90 alignment between the two MCYF, those with unidirectional alignment possess higher tensile strength, Young's modulus, and peel strength, apart from the peel strength of

Uni-0.2(1). For 0/90-2(1), 50% axes of the wefts are perpendicular to the stretching force direction, which decreased its tensile strength and Young's modulus to be about half of those of Uni-2(1), see Figure 6.6(a) and (b) and Figure 6.8. As to the peel strength of Uni-0.2(1) shown in Figure 6.7 (e), the average load during the testing reached almost zero newtons, indicating that the bonding between the two layers of MCYF was extremely low. This could be because the pressure (0.2 MPa) and/or time (1 min) were not sufficient to disperse the dissolved cellulose into the space between the undissolved fibres and into the interface between the two layers. The stress-strain curve of Uni-0.2(1) shows several breaking steps, also suggesting the weak interaction between adjacent MCY caused by the lack of effective matrix material.

After a comparison among Uni-1(1), Uni-2(1) and Uni-4(1), the tensile strength shows independence on processing pressure, but an upward tendency of Young's modulus is found on processing pressure, see Figure 6.6(a) and (b); In terms of peel strength shown in Figure 6.6(c), Uni-2(1) and Uni-4(1) are very similar at 8.7 ± 0.1 N/cm and 9.1 ± 0.2 N/cm, respectively, which are slightly lower than that of Uni-1(1) at 10.9 ± 0.5 N/cm, while in combination with the analysis on the peel test curves in Figure 6.7(a)-(c), Uni-2(1) and Uni-4(1) show more uniform peel test curves than Uni-1(1), suggesting a better bonding interaction between the two layers in Uni-2(1) and Uni-4(1). This is consistent with the optical microscopy results shown in Figure 6.5, where air bubbles were observed on the microscopic image of Uni-1(1) (Figure 6.5(b)).

As to the effect of processing time, the Young's modulus of Uni-2(2), at 5.9 ± 0.1 GPa, is higher than that of Uni-2(1), at 4.4 ± 0.2 GPa, see Figure 6.6(b). This indicates a low effective matrix volume fraction in Uni-2(2) according to

the rule of mixture, where cellulose II and amorphous cellulose - the main contents in matrix - have lower Young's modulus than cellulose I mainly existing in the undissolved fibres [17, 31], recall section 4.3.2. This could be because the pressing with longer time squeezed more dissolved cellulose off the sample which decreased the effective matrix volume fraction, also giving a lower flexibility of Uni-2(2) than that of Uni-2(1), see Figure 6.8. The peel strength is increased upon a longer-time process, see Figure 6.7(b) and (f), where the peel strength was increased from 8.7 ± 0.1 N/cm to 9.8 ± 0.1 N/cm after the processing time was increased from 1 min to 2 min under the same pressure of 2 MPa. Furthermore, the consistency on the interface between the two layers was also improved, shown by the less peak-to-peak distance found on Uni-2(2) in Figure 6.7(f) than that on Uni-2(1) in Figure 6.7(b).

In terms of the effect of number of pressing stage, one stage and two stages, on the mechanical properties, although the tensile strength and Young's modulus of Uni-0.2(1)-2(1) are lower than those of Uni-2(1), the peel strength of Uni-0.2(1)-2(1), at 17.8 ± 0.2 N/cm, is two times as large as that of Uni-2(1). The decrease in Young's modulus indicates higher effective matrix volume fraction and the increase in peel strength denotes better bonding interaction among the interface of the two layers of MCYF. It is likely due to that the low pressure, 0.2 MPa, in the first stage helped the dissolved cellulose to be constrained in the sample rather than being squeezed out by high pressure such as 2 MPa. Further, due to the shear-thinning characteristic of cellulose/[C2mim][OAc] solution, it dispersed more evenly into different MCY and filaments composing the MCY [236], leading to a high effective matrix volume fraction. Whereas the interaction between the two layers of MCYF still

remained low. But this is overcome by the following second pressing stage at 2 MPa which increased the interaction between the two layers and simultaneously further facilitated the dispersion of dissolved cellulose, due to a decreased viscosity by a higher shear rate/pressure. During this two-stage pressing, more effective matrix and/or less dissolved cellulose being squeezed out than the one-stage pressing under pressing time of both 1 min and 2 min. This is because ACC is a self-reinforced composite where no compatibility issues need to be considered, and once the dissolved cellulose is dispersed into the reinforcement phase by the first low-pressure pressing, it is difficult to relatively difficult to remove the dispersed cellulose by pressing.

6.3.4 Comparison between a patented batch method and a proposed continuous process

The method in this chapter compares with the patented method [235], where a interleaf layer of second cellulose-based materials such as cellulose films is needed, in order to provide enough matrix phase to bond the first cellulose-based materials such as fabrics, and no extra interleaf layer is required in the method reported in this chapter, and the fabrication is processed under a relatively low temperature at 40 °C rather than 100 °C reported in the patent.

Furthermore, the mechanical properties including tensile strength, Young's modulus and peel strength of the unidirectional ACCs fabricated in this chapter are in the range of 101.4 MPa to 128.4 MPa, 3.5 GPa to 5.9 GPa and 2.3 N/cm to 17.8 N/cm, respectively, which compares to the ACCs invented in the patent, ranging from 52 MPa to 120 MPa, 2.8 GPa to 7.1 GPa and 0.4 N/cm to 4 N/cm.

The obtained mechanical properties also compare with those found in literature. The Young's modulus and tensile strength up to 22 MPa and 0.134 GPa respectively were seen on a cotton twill weave-based all cellulose composite, which was fabricated with a similar fabrication process, but using [C4mim]Cl as the solvent and 150 ° C as the processing temperature [139].

Apart from the patent, a recently published paper in our group also introduced a batch method with extra interleaf - a cellulose film – to increase the bonding between two fabric layers. The process comparison results are shown in Table 6.2, suggesting that the dissolution time of batch method reported by Ashley et al. [163] is shorter at 10 min than that of the current research at 1 h. This is because the addition of DMSO reduces the viscosity of solvents, and the interleaf contributes to the matrix portion, which make the matrix fraction to the required amount faster. But the temperature used in the current research is lower (40 °C against 100 °C), which in combination with the relatively long processing time, could make the dissolution process easier to control.

Table 6.2 Comparison results of ACCs processing conditions between current research method and a batch method

Dissolution time	Dissolution Temperature (°C)	Solvent system	Cellulose to solvent weight ratio	Ref.
10 min	100	[C2mim][OA]+ DMSO	1:3	[163]
1 h	40	[C2mim][OA]	<<1:4	This research

Here, the reported partial-dissolving process is implemented in a separate solvent bath from the pressing process, which brings it the potential to be a continuous process. This resolves the limits found in the hot-pressing method, where the sample size is limited by the size of hot-press mould-brings it

difficulty to be a continuous manufacturing process [163]. Herein, a continuous fabricating process of ACCs is proposed and shown in Figure 6.9.

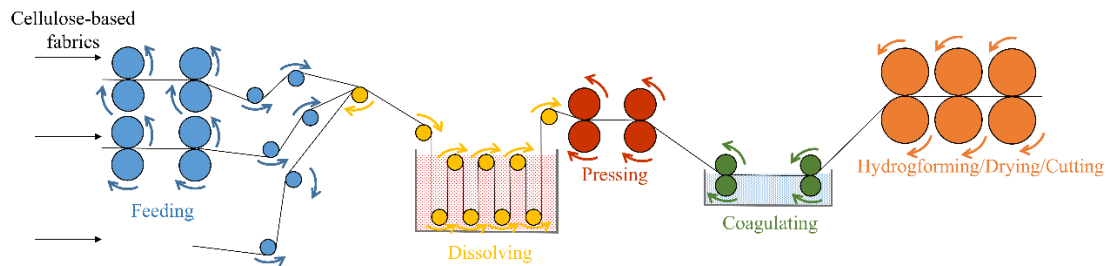


Figure 6.9 Schematic flow chart of the proposed continuous manufacturing process, where the feeding section, dissolving section, pressing section, coagulating section and forming/drying section are in blue, yellow, red, green and orange, respectively; the circles, red-shaded area and blue-shaded area denote rollers, solvent, e.g. ionic liquids, and coagulant, e.g. water, respectively

The proposed industrial-fabricating process is composed of several sections, including fabrics feeding section, dissolving with solvents section, pressing (low- and high-pressure rollers) section, coagulating with coagulant section (including recycling system for the solvents), and forming and drying section, see Figure 6.9. Among them, there could be several layers of fabrics feeding into the system from the beginning, and for the dissolving section, the container with solvents should be placed in a low water content circumstance for those easily water-absorb solvents, i.e. [C2mim][OAc] systems. As for the coagulating section, the water liquids can be collected for further recycling process.

6.4 Conclusions

ACCs are successfully fabricated from the two layers of plain woven of mercerized cotton yarn that possess lower dissolution activation and higher thermal stability than the natural cotton yarn, via a potential continuous process. Optical microscopy, tensile test and peel test are applied to explore the effect of pressing pressure, number of pressing stages, alignment of the two layers and pressing time on the outcomes of ACCs. OM images show that different pressure and number of pressing stages affect the bonding interactions between the two layers, where a strong bonding interaction was seen on the Uni-0.2(1)-2(1) sample.

As to the mechanical properties, including tensile strength, Young's modulus and peel strength are found in the range from 101.4 MPa to 128.4 MPa, 3.5 GPa to 5.9 GPa and 2.3 N/cm to 17.8 N/cm, respectively. The ACCs with 0/90 alignment show higher comprehensive mechanical properties than those with unidirectional alignment. Within the tested pressure range, the pressing pressure rarely affects the tensile strength but determines the Young's modulus and peel strength. As to the number of pressing stages, the two-pressing stage with 0.2 MPa as the low pressure and subsequently a 2 MPa as the high-pressure stage shows significant improvement on the peel strength with minor influence on the tensile strength, compared with the single pressing stage. The reason is considered to be that the first-stage low pressure stage facilitates the dispersity of dissolved cellulose into gaps in the fabrics, yarns, and interface between the two layers, and the following 2 MPa stage contributes to increase the bonding between two layers, leading to a higher effective matrix fraction in the final ACCs.

The current fabrication method compares favourably with the reported method, showing a higher potential to be scaled up to make large samples, and as a result, an industrial-fabricating process is proposed. The findings in this chapter could provide instructive information to researchers fabricating ACCs and related industries.

Chapter 7 Conclusion and prospective

7.1 Outcomes and conclusions

In this thesis, the dissolution in [C2mim][OAc] and the pyrolysis behaviour under non-isothermal conditions of two cellulose-based materials, the natural cotton yarn and the mercerized cotton yarn, have been explored; and ACCs are successfully made out of a basket plain weave of the mercerized cotton yarn with a one-step partially dissolving approach using [C2mim][OAc]. It has huge potential to be scaled up into a continuous fabricating process. The results of the research on the dissolution and pyrolysis kinetics of the two cotton samples are summarized in Table 7.1, in conjunction with the other comparative properties.

Table 7.1 Summary of the dissolution and pyrolysis properties of the natural cotton and mercerized cotton in this thesis, with their carbohydrate composition and molecular weight

Property	NY-raw	MCY-raw
Dissolution E_a (kJ/mol)	95 ± 2	74 ± 2
Pyrolysis E_a (kJ/mol)	153 ± 2	191 ± 7
Intrinsic T_m (°C)	317 ± 6	346 ± 3
Lignin content of dry samples (mg/g)	12.90	10.40
Arabinose (mg/g)	3.94	null
Rhamnose (mg/g)	1.23	null
Xylose (mg/g)	2.08	null
Galacturonic acid (mg/g)	6.73	null
Mannose (mg/g)	null	null
Galactose (mg/g)	2.72	null
Glucose (mg/g)	156.69	142.95
M_n (kDa)	653 ± 18	252 ± 5
M_w (kDa)	1069 ± 19	385 ± 4
Polydispersity [M_w/M_n]	1.64 ± 0.07	1.53 ± 0.02
Reg (µmol/g)	1.53 ± 0.04	3.98 ± 0.09
Crystalline structure	cellulose I amorphous region	cellulose I cellulose II amorphous region

For the dissolution of the natural cotton yarn in excess amount of [C2mim][OAc] [179], three sample arrangements were applied, and optical microscopy and X-ray diffraction were used to examine their changes in the coagulation fraction of the resultant samples in association with the morphology and crystalline structure, respectively. A time-temperature equivalence was found upon the examination of the coagulation fraction as a function of time for different processing temperatures. The time-temperature

superposition method was then successfully applied to analyse the dissolution behaviour which turns out to follow the Arrhenius behaviour. This gives activation energies to be calculated for different arrangements, at 96 ± 8 kJ/mol, 97 ± 3 kJ/mol and 91 ± 11 kJ/mol for cotton single yarn, cotton array and cotton bundle, respectively. These activation energies interestingly agree with each other within the range of their errors, resulting an average dissolution activation energy of 95 ± 2 kJ/mol. As for the dissolution kinetics of the mercerized cotton yarn in [C2mim][OAc], optical microscopy and X-ray diffraction were again used to characterize the micromorphology and crystalline structure of the resultant samples. Subsequently, four quantifying methods were implemented with different quantification parameters, including CF_{OM} , CF_{XRD} , CF_{OM-H} and T_H . Further, similar to the natural cotton, the time-temperature superposition method was again successfully applied to explore the dissolution behaviour of the mercerized cotton yarn hydrogel and the dried mercerized cotton yarn, upon the dissolving process under different combinations of time and temperature. The Arrhenius behaviour was again seen on dissolution of the mercerized cotton yarn. This allows activation energies with aspect to CF_{OM} , CF_{XRD} , CF_{OM-H} and T_H to be found as 69 ± 5 kJ/mol, 78 ± 10 kJ/mol, 78 ± 4 kJ/mol and 71 ± 4 kJ/mol, respectively. An independence of these activation energies on the quantifying method is found, giving an average value of 74 ± 2 kJ/mol. This agreement confirms the universality of the TTS analysis on both natural and mercerized cotton cellulose, and it also suggests the advance of the measurement of the mercerized cotton yarn hydrogel with optical microscopy as it dramatically saves time on experiment. Additionally, a facile and novel method to examine

the regional water volume fraction and swelling ratio of the cellulose hydrogel was reported for the first time as of writing.

The pyrolysis kinetics of the natural cotton yarn and the mercerized cotton yarn is investigated via TGA under different heating rates. A modified first order global model was reported to effectively describe the pyrolysis behaviour, where the integration temperature range is gradually narrowing to zero at which the discrepancy from the mathematical approximations is the smallest. Consequently, the pyrolysis activation energies of the natural cotton and the mercerized cotton are confirmed to be 153 ± 2 kJ/mol and 191 ± 7 kJ/mol, respectively. In addition, the decomposition temperature was found dependent on heating rate, and an exponential equation was used to adequately fit the tendency. From that, an intrinsic decomposition temperature, i.e. the decomposition temperature at heating rate of zero, can be obtained, at 317 ± 3 °C and 346 ± 6 °C for the natural and mercerized cotton respectively. The above results indicate that the mercerized cotton sample is more thermally stable than the natural cotton sample.

In order to explain the difference in the dissolution kinetics and pyrolysis behaviour between the two cotton samples, carbohydrate composition analysis, molecular weight and crystalline structure were measured and analysed, see Table 7.1. The reasons for the difference in the dissolution activation energy are likely to be caused by the difference in either the molecular weight [222] and/or the carbohydrate composition. While for the difference in the pyrolysis behaviour, it is hypothesized that the carbohydrate composition and/or the crystalline structure dominate the pyrolysis behaviour, where the existence of lignin and hemicellulose with lower thermal stability

than cellulose shifted the pyrolysis activation energy and decomposition temperature to lower values; and the cellulose II with higher thermal stability than cellulose I in the mercerized cotton sample also increases the two values.

ACCs were successfully fabricated with a selective-surficial dissolution process, i.e. one-step method, using excess amount of [C2mim][OAc], where the dissolving process and pressing process are separated, differentiating from the methods reported in literature [146, 157, 235]. A potential continuous fabricating process is then proposed in this thesis, which has huge potential to be scaled up into industrial size for large-scale fabrication of ACCs.

7.2 Prospective and future plans

The hypothesis for the difference in kinetics of dissolution and pyrolysis between the two samples needs further verification. Therefore, for the difference in dissolution kinetics, the reasons have been postulated to be the difference in carbohydrate composition or/and the molecular weight between the two samples, and this could be further verified by mercerizing the natural cotton in a relatively mild condition where the hemicellulose is significantly removed with the molecular weight being minor influenced; as to the difference in pyrolysis behaviour, the hypothesized reasons could also be verified by mercerizing the natural cotton sample. Besides, the proposed continuous fabricating ACCs process needs to be scaled up to a lab scale in the first instance before it can be finally industrialized in a large scale.

The findings in the thesis can also be informative to researchers doing studies in dissolution and pyrolysis of cellulose-based materials, and fabrication of all cellulose composites.

References

- [1] Moon, R.J., Martini, A., Nairn, J., Simonsen, J. and Youngblood, J. Cellulose nanomaterials review: structure, properties and nanocomposites. *Chemical Society Reviews*. 2011, **40**(7), pp.3941-3994.
- [2] Ihnat, V., Lübke, H., Balbercak, J. and Kuna, V. Size reduction downcycling of waste wood. Review. *Wood Res*. 2020, **65**, pp.205-220.
- [3] Baghaei, B., Johansson, B., Skrifvars, M. and Kadi, N. All-Cellulose Composites Properties from Pre-and Post-Consumer Denim Wastes: Comparative Study. *Journal of Composites Science*. 2022, **6**(5), p.130.
- [4] Nishino, T., Matsuda, I. and Hirao, K. All-Cellulose Composite. *Macromolecules*. 2004, **37**(20), pp.7683-7687.
- [5] Olsson, C., Idström, A., Nordstierna, L. and Westman, G. Influence of water on swelling and dissolution of cellulose in 1-ethyl-3-methylimidazolium acetate. *Carbohydrate Polymers*. 2014, **99**, pp.438-446.
- [6] Liebert, T. Cellulose solvents—remarkable history, bright future. In: Liebert, T., Heinze, T. and Edgar, K. eds. *Cellulose solvents: for analysis, shaping and chemical modification*. Washington, DC: ACS Publications, 2010, pp.3-54.
- [7] Swatloski, R.P., Spear, S.K., Holbrey, J.D. and Rogers, R.D. Dissolution of cellulose with ionic liquids. *Journal of the American Chemical Society*. 2002, **124**(18), pp.4974-4975.
- [8] Boonmahitthisud, A., Soykeabkaew, N., Ongthip, L. and Tanpichai, S. Review of the recent developments in all-cellulose nanocomposites: Properties and applications. *Carbohydrate Polymers*. 2022, p.119192.
- [9] Kostag, M., Jedvert, K. and El Seoud, O.A. Engineering of sustainable biomaterial composites from cellulose and silk fibroin: Fundamentals and applications. *International Journal of Biological Macromolecules*. 2021, **167**, pp.687-718.
- [10] Baghaei, B. and Skrifvars, M. All-Cellulose Composites: A Review of Recent Studies on Structure, Properties and Applications. *Molecules*. 2020, **25**(12).
- [11] Huber, T., Mussig, J., Curnow, O., Pang, S.S., Bickerton, S. and Staiger, M.P. A critical review of all-cellulose composites. *Journal of Materials Science*. 2012, **47**(3), pp.1171-1186.
- [12] Soykeabkaew, N., Nishino, T. and Peijs, T. All-cellulose composites of regenerated cellulose fibres by surface selective dissolution. *Composites Part A: Applied Science and Manufacturing*. 2009, **40**(4), pp.321-328.

- [13] Green, S.M., Ries, M.E., Moffat, J. and Budtova, T. NMR and rheological study of anion size influence on the properties of two imidazolium-based ionic liquids. *Scientific Reports*. 2017, **7**(1), pp.1-12.
- [14] Sescousse, R., Le, K.A., Ries, M.E. and Budtova, T. Viscosity of cellulose– imidazolium-based ionic liquid solutions. *The Journal of Physical Chemistry B*. 2010, **114**(21), pp.7222-7228.
- [15] Lovell, C.S., Walker, A., Damion, R.A., Radhi, A., Tanner, S.F., Budtova, T. and Ries, M.E. Influence of cellulose on ion diffusivity in 1-ethyl-3-methyl-imidazolium acetate cellulose solutions. *Biomacromolecules*. 2010, **11**(11), pp.2927-2935.
- [16] Rosenau, T., Potthast, A., Sixta, H. and Kosma, P. The chemistry of side reactions and byproduct formation in the system NMMO/cellulose (Lyocell process). *Progress in Polymer Science*. 2001, **26**(9), pp.1763-1837.
- [17] Nishino, T., Takano, K. and Nakamae, K. Elastic modulus of the crystalline regions of cellulose polymorphs. *Journal of Polymer Science Part B: Polymer Physics*. 1995, **33**(11), pp.1647-1651.
- [18] Šturcová, A., Davies, G.R. and Eichhorn, S.J. Elastic Modulus and Stress-Transfer Properties of Tunicate Cellulose Whiskers. *Biomacromolecules*. 2005, **6**(2), pp.1055-1061.
- [19] Matsuo, M., Sawatari, C., Iwai, Y. and Ozaki, F. Effect of orientation distribution and crystallinity on the measurement by X-ray diffraction of the crystal lattice moduli of cellulose I and II. *Macromolecules*. 1990, **23**(13), pp.3266-3275.
- [20] Sundarraj, A.A. and Ranganathan, T.V. A review on cellulose and its utilization from agro-industrial waste. *Drug Invention Today*. 2018, **10**(1), pp.89-94.
- [21] O'sullivan, A.C. Cellulose: the structure slowly unravels. *Cellulose*. 1997, **4**(3), pp.173-207.
- [22] Wertz, J.L., Bédué, O. and Mercier, J.P. *Cellulose science and technology*. First edition ed. Lausanne, Switzerland: EPFL press, 2010.
- [23] Clibbens, D.A. XII.—THE MERCERISATION OF COTTON: A Review of the Literature. *Journal of the Textile Institute Transactions*. 1923, **14**(8), pp.T217-T249.
- [24] Sakurada, I., Nukushina, Y. and Ito, T. Experimental determination of the elastic modulus of crystalline regions in oriented polymers. *Journal of Polymer Science*. 1962, **57**(165), pp.651-660.
- [25] Wu, X., Moon, R.J. and Martini, A. Crystalline cellulose elastic modulus predicted by atomistic models of uniform deformation and nanoscale indentation. *Cellulose*. 2013, **20**(1), pp.43-55.

- [26] Santiago Cintrón, M., Johnson, G.P. and French, A.D. Young's modulus calculations for cellulose I β by MM3 and quantum mechanics. *Cellulose*. 2011, **18**(3), pp.505-516.
- [27] Cael, J., Gardner, K., Koenig, J. and Blackwell, J. Infrared and Raman spectroscopy of carbohydrates. Paper V. Normal coordinate analysis of cellulose I. *The Journal of Chemical Physics*. 1975, **62**(3), pp.1145-1153.
- [28] Lyons, W.J. Theoretical value of the dynamic stretch modulus of cellulose. *Journal of Applied Physics*. 1959, **30**(5), pp.796-797.
- [29] Tashiro, K. and Kobayashi, M. Theoretical evaluation of three-dimensional elastic constants of native and regenerated celluloses: role of hydrogen bonds. *Polymer*. 1991, **32**(8), pp.1516-1526.
- [30] Eichhorn, S.J., Young, R.J. and Davies, G.R. Modeling Crystal and Molecular Deformation in Regenerated Cellulose Fibers. *Biomacromolecules*. 2005, **6**(1), pp.507-513.
- [31] Zhang, X., Tschopp, M.A., Horstemeyer, M.F., Shi, S.Q. and Cao, J. Mechanical properties of amorphous cellulose using molecular dynamics simulations with a reactive force field. *International Journal of Modelling, Identification and Control*. 2013, **18**(3), pp.211-217.
- [32] Chen, W., Lickfield, G.C. and Yang, C.Q. Molecular modeling of cellulose in amorphous state. Part I: model building and plastic deformation study. *Polymer*. 2004, **45**(3), pp.1063-1071.
- [33] Zhu, M.Z., Chen, Y.F., Zhu, W.B., Du, X.M., Zhou, J.B., Gu, C. and Liao, R.J. Mechanical property of hydrous amorphous cellulose studied by molecular dynamics. *Russian Journal of Physical Chemistry B*. 2016, **10**(3), pp.524-530.
- [34] Ottesen, V., Larsson, P.T., Chinga-Carrasco, G., Syverud, K. and Gregersen, Ø.W. Mechanical properties of cellulose nanofibril films: effects of crystallinity and its modification by treatment with liquid anhydrous ammonia. *Cellulose*. 2019, **26**(11), pp.6615-6627.
- [35] Lindman, B., Karlström, G. and Stigsson, L. On the mechanism of dissolution of cellulose. *Journal of Molecular Liquids*. 2010, **156**(1), pp.76-81.
- [36] Turbak, A.F., Hammer, R.B., Davies, R.E. and Hergert, H.L. CELLULOSE SOLVENTS. *ChemTech*. 1980, **10**, p.51.
- [37] Liebert, T. Cellulose Solvents – Remarkable History, Bright Future. In: *Cellulose Solvents: For Analysis, Shaping and Chemical Modification*. American Chemical Society, 2010, pp.3-54.
- [38] Sen, S., Martin, J.D. and Argyropoulos, D.S. Review of Cellulose Non-Derivatizing Solvent Interactions with Emphasis on Activity in Inorganic

Molten Salt Hydrates. *ACS Sustainable Chemistry & Engineering*. 2013, **1**(8), pp.858-870.

- [39] Tanyolaç, D. and Özdural, A.R. Preparation of low-cost magnetic nitrocellulose microbeads. *Reactive and Functional Polymers*. 2000, **45**(3), pp.235-242.
- [40] Naderizadeh, B., Moghimi, A. and Shahi, M. Electrospun nitrocellulose and composite nanofibers. *Journal of Nanostructures*. 2012, **2**(3), pp.287-293.
- [41] Takenaka, H. The interaction parameter for solutions of nitrocellulose in acetone. *Journal of Polymer Science*. 1957, **24**(107), pp.321-332.
- [42] Benhammada, A. and Trache, D. Green synthesis of CuO nanoparticles using *Malva sylvestris* leaf extract with different copper precursors and their effect on nitrocellulose thermal behavior. *Journal of Thermal Analysis and Calorimetry*. 2022, **147**(2), pp.1-16.
- [43] Ratanakamnuan, U., Atong, D. and Aht-Ong, D. Cellulose esters from waste cotton fabric via conventional and microwave heating. *Carbohydrate Polymers*. 2012, **87**(1), pp.84-94.
- [44] Fox, S.C., Li, B., Xu, D. and Edgar, K.J. Regioselective esterification and etherification of cellulose: a review. *Biomacromolecules*. 2011, **12**(6), pp.1956-1972.
- [45] Polyuto, A., Kleiner, Y.Y., Irklej, V. and Gal'braikh, L. Study of the possibility of processing cotton cellulose in bulk for fabrication of viscose fibre. *Fibre Chemistry*. 2000, **32**(5), pp.353-355.
- [46] Zhang, J.M., Wu, J., Yu, J., Zhang, X.Y., He, J.S. and Zhang, J. Application of ionic liquids for dissolving cellulose and fabricating cellulose-based materials: state of the art and future trends. *Materials Chemistry Frontiers*. 2017, **1**(7), pp.1273-1290.
- [47] Clotworthy, H. The manufacture of artificial silk with special reference to viscose. *Journal of the Society of Chemical Industry*. 1928, **47**(2), pp.24-30.
- [48] Johnson, D.L. *Method of preparing polymers from a mixture of cyclic amine oxides and polymers*. US3508941A. 1970.
- [49] Johnson, D.L. *Compounds dissolved in cyclic amine oxides*. US3447939A. 1969.
- [50] Rosenau, T., Potthast, A., Adorjan, I., Hofinger, A., Sixta, H., Firgo, H. and Kosma, P. Cellulose solutions in N-methylmorpholine-N-oxide (NMMO)–degradation processes and stabilizers. *Cellulose*. 2002, **9**(3-4), pp.283-291.
- [51] Isik, M., Sardon, H. and Mecerreyes, D. Ionic liquids and cellulose: dissolution, chemical modification and preparation of new cellulosic

materials. *International journal of molecular sciences*. 2014, **15**(7), pp.11922-11940.

- [52] McCormick, C.L. *Novel cellulose solutions*. US4278790A. 1981.
- [53] Zhang, C., Liu, R., Xiang, J., Kang, H., Liu, Z. and Huang, Y. Dissolution Mechanism of Cellulose in N,N-Dimethylacetamide/Lithium Chloride: Revisiting through Molecular Interactions. *The Journal of Physical Chemistry B*. 2014, **118**(31), pp.9507-9514.
- [54] Isogai, A. and Atalla, R.H. *Alkaline method for dissolving cellulose*. US4302252. 1995.
- [55] Potthast, A., Rosenau, T., Buchner, R., Röder, T., Ebner, G., Bruglachner, H., Sixta, H. and Kosma, P. The cellulose solvent system N,N-dimethylacetamide/lithium chloride revisited: the effect of water on physicochemical properties and chemical stability. *Cellulose*. 2002, **9**(1), pp.41-53.
- [56] Davidson, G. 12—The Dissolution of Chemically Modified Cotton Cellulose in Alkaline Solutions. Part I—in Solutions of Sodium Hydroxide, Particularly at Temperatures Below the Normal. *Journal of the Textile Institute Transactions*. 1934, **25**(5), pp.T174-T196.
- [57] Davidson, G. 10—THE DISSOLUTION OF CHEMICALLY MODIFIED COTTON CELLULOSE IN ALKALINE SOLUTIONS. PART II.—A COMPARISON OF THE SOLVENT ACTION OF SOLUTIONS OF LITHIUM, SODIUM, POTASSIUM, AND TETRAMETHYLAMMONIUM HYDROXIDES. *Journal of the Textile Institute Transactions*. 1936, **27**(4), pp.T112-T130.
- [58] Budtova, T. and Navard, P. Cellulose in NaOH–water based solvents: a review. *Cellulose*. 2016, **23**(1), pp.5-55.
- [59] Laszkiewicz, B. and Wcislo, P. Sodium cellulose formation by activation process. *Journal of Applied Polymer Science*. 1990, **39**(2), pp.415-425.
- [60] Cai, J. and Zhang, L. Rapid dissolution of cellulose in LiOH/urea and NaOH/urea aqueous solutions. *Macromolecular Bioscience*. 2005, **5**(6), pp.539-548.
- [61] Walden, P. Ueber die Molekulargrösse und elektrische Leitfähigkeit einiger geschmolzenen Salze. *Известия Российской академии наук. Серия математическая*. 1914, **8**(6), pp.405-422.
- [62] Graenacher, C. *Cellulose solution*. US1943176A. 1934.
- [63] Hedlund, A., Köhnke, T., Hagman, J., Olsson, U. and Theliander, H. Microstructures of cellulose coagulated in water and alcohols from 1-ethyl-3-methylimidazolium acetate: contrasting coagulation mechanisms. *Cellulose*. 2019, **26**(3), pp.1545-1563.

- [64] Yang, Y.P., Zhang, Y., Dawelbeit, A., Deng, Y., Lang, Y.X. and Yu, M.H. Structure and properties of regenerated cellulose fibers from aqueous NaOH/thiourea/urea solution. *Cellulose*. 2017, **24**(10), pp.4123-4137.
- [65] Zhang, H., Wu, J., Zhang, J. and He, J.S. 1-Allyl-3-methylimidazolium chloride room temperature ionic liquid: A new and powerful nonderivatizing solvent for cellulose. *Macromolecules*. 2005, **38**(20), pp.8272-8277.
- [66] Le, K.A., Sescousse, R. and Budtova, T. Influence of water on cellulose-EMIMAc solution properties: a viscometric study. *Cellulose*. 2012, **19**(1), pp.45-54.
- [67] Hedlund, A., Köhnke, T. and Theliander, H. Coagulation of EmimAc-cellulose solutions: dissolution-precipitation disparity and effects of non-solvents and cosolvent. *Nordic Pulp & Paper Research Journal*. 2015, **30**(1), pp.32-42.
- [68] Geng, H., Yuan, Z., Fan, Q., Dai, X., Zhao, Y., Wang, Z. and Qin, M. Characterisation of cellulose films regenerated from acetone/water coagulants. *Carbohydrate Polymers*. 2014, **102**, pp.438-444.
- [69] Duchemin, B.J.C., Newman, R.H. and Staiger, M.P. Structure–property relationship of all-cellulose composites. *Composites Science and Technology*. 2009, **69**(7), pp.1225-1230.
- [70] Hauru, L.K., Hummel, M., King, A.W., Kilpeläinen, I. and Sixta, H. Role of solvent parameters in the regeneration of cellulose from ionic liquid solutions. *Biomacromolecules*. 2012, **13**(9), pp.2896-2905.
- [71] Wawro, D., Hummel, M., Michud, A. and Sixta, H. Strong cellulosic film cast from ionic liquid solutions. *Fibres & Textiles in Eastern Europe*. 2014, **3**(105), pp.35-42.
- [72] Bang, Y.H., Lee, S., Park, J.B. and Cho, H.H. Effect of coagulation conditions on fine structure of regenerated cellulosic films made from cellulose/N - methylmorpholine - N - oxide/H₂O systems. *Journal of Applied Polymer Science*. 1999, **73**(13), pp.2681-2690.
- [73] Hedlund, A., Theliander, H. and Köhnke, T. Mass transport during coagulation of cellulose-ionic liquid solutions in different non-solvents. *Cellulose*. 2019, **26**(16), pp.8525-8541.
- [74] Hedlund, A., Köhnke, T. and Theliander, H. Diffusion in Ionic Liquid–Cellulose Solutions during Coagulation in Water: Mass Transport and Coagulation Rate Measurements. *Macromolecules*. 2017, **50**(21), pp.8707-8719.
- [75] Gupta, K.M., Hu, Z. and Jiang, J. Molecular insight into cellulose regeneration from a cellulose/ionic liquid mixture: effects of water concentration and temperature. *RSC Advances*. 2013, **3**(13), pp.4425-4433.

- [76] Hunter, L. The variation with temperature of the principal elastic moduli of NaCl near the melting point. *Physical Review*. 1942, **61**(1-2), p.84.
- [77] Shamshina, J.L. and Abidi, N. Cellulose nanocrystals from ionic liquids: a critical review. *Green Chemistry*. 2021, **23**(17), pp.6205-6222.
- [78] Meksi, N. and Moussa, A. A review of progress in the ecological application of ionic liquids in textile processes. *Journal of Cleaner Production*. 2017, **161**, pp.105-126.
- [79] Keskin, S., Kayrak-Talay, D., Akman, U. and Hortaçsu, Ö. A review of ionic liquids towards supercritical fluid applications. *The Journal of Supercritical Fluids*. 2007, **43**(1), pp.150-180.
- [80] Welton, T. Room-Temperature Ionic Liquids. Solvents for Synthesis and Catalysis. *Chemical Reviews*. 1999, **99**(8), pp.2071-2084.
- [81] Heinze, T., Schwikal, K. and Barthel, S. Ionic liquids as reaction medium in cellulose functionalization. *Macromolecular Bioscience*. 2005, **5**(6), pp.520-525.
- [82] Kaufmann, D.E., Nouroozian, M. and Henze, H. Molten salts as an efficient medium for palladium catalyzed CC coupling reactions. *Synlett*. 1996, **1996**(11), pp.1091-1092.
- [83] Kumar, A. and Pawar, S.S. Converting exo-Selective Diels–Alder Reaction to endo-Selective in Chloroaluminate Ionic Liquids. *The Journal of Organic Chemistry*. 2004, **69**(4), pp.1419-1420.
- [84] Greaves, T.L. and Drummond, C.J. Protic ionic liquids: properties and applications. *Chemical reviews*. 2008, **108**(1), pp.206-237.
- [85] Javed, F., Ullah, F., Zakaria, M.R. and Akil, H.M. An approach to classification and hi-tech applications of room-temperature ionic liquids (RTILs): A review. *Journal of Molecular Liquids*. 2018, **271**, pp.403-420.
- [86] McDaniel, J.G. and Verma, A. On the Miscibility and Immiscibility of Ionic Liquids and Water. *The Journal of Physical Chemistry B*. 2019, **123**(25), pp.5343-5356.
- [87] Klähn, M. and Seduraman, A. What Determines CO₂ Solubility in Ionic Liquids? A Molecular Simulation Study. *The Journal of Physical Chemistry B*. 2015, **119**(31), pp.10066-10078.
- [88] Pereira, J.F., Flores, L.A., Wang, H. and Rogers, R.D. Benzene solubility in ionic liquids: working toward an understanding of liquid clathrate formation. *Chemistry–A European Journal*. 2014, **20**(47), pp.15482-15492.
- [89] Liang, Y., Hawkins, J.E., Ries, M.E. and Hine, P.J. Dissolution of cotton by 1-ethyl-3-methylimidazolium acetate studied with time–temperature superposition for three different fibre arrangements. *Cellulose*. 2021, **28**(2), pp.715-727.

- [90] Abbott, A.P., Frisch, G., Hartley, J., Karim, W.O. and Ryder, K.S. Anodic dissolution of metals in ionic liquids. *Progress in Natural Science: Materials International*. 2015, **25**(6), pp.595-602.
- [91] Dyson, P.J. Transition metal chemistry in ionic liquids. *Transition Metal Chemistry*. 2002, **27**(4), pp.353-358.
- [92] Yang, J., Li, W., Liu, Q. and Liu, H. Dissolution of antibiotics mycelium in ionic liquids: Performance and mechanism. *Chinese Journal of Chemical Engineering*. 2018, **26**(2), pp.252-258.
- [93] Schindl, A., Hagen, M.L., Muzammal, S., Gunasekera, H.A. and Croft, A.K. Proteins in ionic liquids: Reactions, applications, and futures. *Frontiers in Chemistry*. 2019, **7**, p.347.
- [94] Franklin, M.S., Larm, N.E., Baker, G.A. and Zhao, H. Functionalized ionic liquids for lignite dissolution and treatment. *Journal of Chemical Technology & Biotechnology*. 2021, **96**(12), pp.3273-3281.
- [95] Winterton, N. Solubilization of polymers by ionic liquids. *Journal of Materials Chemistry*. 2006, **16**(44), pp.4281-4293.
- [96] Renner, R. Ionic liquids: an industrial cleanup solution. *Environmental Science & Technology*. 2001, **35**(19), pp.410A-413A.
- [97] Gordon, C.M. New developments in catalysis using ionic liquids. *Applied Catalysis A: General*. 2001, **222**(1-2), pp.101-117.
- [98] Nowicki, J., Muszyński, M. and Gryglewicz, S. Novel basic ionic liquids from cyclic guanidines and amidines—new catalysts for transesterification of oleochemicals. *Journal of Chemical Technology & Biotechnology*. 2014, **89**(1), pp.48-55.
- [99] Keithellakpam, S. and Laitonjam, W.S. A simple, efficient and green procedure for Michael addition catalyzed by [C4dabco] OH ionic liquid. *Chinese Chemical Letters*. 2014, **25**(5), pp.767-770.
- [100] Singh, S.K. and Savoy, A.W. Ionic liquids synthesis and applications: An overview. *Journal of Molecular Liquids*. 2020, **297**, p.112038.
- [101] Niedermeyer, H., Hallett, J.P., Villar-Garcia, I.J., Hunt, P.A. and Welton, T. Mixtures of ionic liquids. *Chemical Society Reviews*. 2012, **41**(23), pp.7780-7802.
- [102] Spörl, J.M., Batti, F., Vocht, M.P., Raab, R., Müller, A., Hermanutz, F. and Buchmeiser, M.R. Ionic Liquid Approach Toward Manufacture and Full Recycling of All - Cellulose Composites. *Macromolecular Materials and Engineering*. 2018, **303**(1), p.1700335.
- [103] Liu, Y., Meyer, A.S., Nie, Y., Zhang, S. and Thomsen, K. Low energy recycling of ionic liquids via freeze crystallization during cellulose spinning. *Green chemistry*. 2018, **20**(2), pp.493-501.

- [104] Chauvin, Y., Mussmann, L. and Olivier, H. A novel class of versatile solvents for two - phase catalysis: hydrogenation, isomerization, and hydroformylation of alkenes catalyzed by rhodium complexes in liquid 1, 3 - dialkylimidazolium salts. *Angewandte Chemie International Edition in English*. 1996, **34**(23 - 24), pp.2698-2700.
- [105] Dyson, P.J., Ellis, D.J., Welton, T. and Parker, D.G. Arene hydrogenation in a room-temperature ionic liquid using a ruthenium cluster catalyst. *Chemical Communications*. 1999, (1), pp.25-26.
- [106] Mizushima, E., Hayashi, T. and Tanaka, M. Palladium-catalysed carbonylation of aryl halides in ionic liquid media: high catalyst stability and significant rate-enhancement in alkoxy carbonylation. *Green Chemistry*. 2001, **3**(2), pp.76-79.
- [107] Consultancy, H.K. Ionic liquids 2030—ionic liquid technologies, markets, applications, companies and developments worldwide 2008 to 2020 and 2030. Tübingen, Germany. *Tübingen, Germany. Tübingen*. 2012.
- [108] Andanson, J.-M., Bordes, E., Devémy, J., Leroux, F., Pádua, A.A. and Gomes, M.F.C.J.G.C. Understanding the role of co-solvents in the dissolution of cellulose in ionic liquids. *Green Chemistry*. 2014, **16**(5), pp.2528-2538.
- [109] Schubert, T.J.S. Current and Future Ionic Liquid Markets. In: Shiflett, M. and Scurto, A. eds. *Ionic Liquids: Current State and Future Directions*. Washington, DC: American Chemical Society, 2017, pp.35-65.
- [110] Chen, J., Chen, X., Su, M., Ye, J., Hong, J. and Yang, Z. Direct production of all-wood plastics by kneading in ionic liquids/DMSO. *Chemical Engineering Journal*. 2015, **279**, pp.136-142.
- [111] Patuszyński, K. and Domańska, U. Viscosity of Ionic Liquids: An Extensive Database and a New Group Contribution Model Based on a Feed-Forward Artificial Neural Network. *Journal of Chemical Information and Modeling*. 2014, **54**(5), pp.1311-1324.
- [112] Chen, J.Q., Chen, X., Su, M., Ye, J.D., Hong, J.G. and Yang, Z. Direct production of all-wood plastics by kneading in ionic liquids/DMSO. *Chemical Engineering Journal*. 2015, **279**, pp.136-142.
- [113] Wang, H., Gurau, G. and Rogers, R.D. Ionic liquid processing of cellulose. *Chemical Society Reviews*. 2012, **41**(4), pp.1519-1537.
- [114] Xu, A., Wang, J. and Wang, H. Effects of anionic structure and lithium salts addition on the dissolution of cellulose in 1-butyl-3-methylimidazolium-based ionic liquid solvent systems. *Green Chemistry*. 2010, **12**(2), pp.268-275.
- [115] Remsing, R.C., Hernandez, G., Swatloski, R.P., Masefski, W.W., Rogers, R.D. and Moyna, G. Solvation of carbohydrates in N, N' - dialkylimidazolium ionic liquids: A multinuclear NMR spectroscopy

study. *The Journal of Physical Chemistry B*. 2008, **112**(35), pp.11071-11078.

- [116] Youngs, T.G., Holbrey, J.D., Deetlefs, M., Nieuwenhuyzen, M., Costa Gomes, M.F. and Hardacre, C. A molecular dynamics study of glucose solvation in the ionic liquid 1, 3 - dimethylimidazolium chloride. *ChemPhysChem*. 2006, **7**(11), pp.2279-2281.
- [117] Roselli, A., Hummel, M., Vartiainen, J., Nieminen, K. and Sixta, H. Understanding the role of water in the interaction of ionic liquids with wood polymers. *Carbohydrate Polymers*. 2017, **168**, pp.121-128.
- [118] Chang, H.-C., Zhang, R.-L. and Hsu, D.-T. The effect of pressure on cation–cellulose interactions in cellulose/ionic liquid mixtures. *Physical Chemistry Chemical Physics*. 2015, **17**(41), pp.27573-27578.
- [119] Cho, H.M., Gross, A.S. and Chu, J.W. Dissecting force interactions in cellulose deconstruction reveals the required solvent versatility for overcoming biomass recalcitrance. *Journal of the American Chemical Society*. 2011, **133**(35), pp.14033-14041.
- [120] Lu, B., Xu, A. and Wang, J. Cation does matter: how cationic structure affects the dissolution of cellulose in ionic liquids. *Green Chemistry*. 2014, **16**(3), pp.1326-1335.
- [121] Budtova, T. and Navard, P. Viscosity-temperature dependence and activation energy of cellulose solutions. *Nordic Pulp & Paper Research Journal*. 2015, **30**(1), pp.99-104.
- [122] Chen, F., Sawada, D., Hummel, M., Sixta, H. and Budtova, T. Swelling and dissolution kinetics of natural and man-made cellulose fibers in solvent power tuned ionic liquid. *Cellulose*. 2020, **27**(13), pp.7399-7415.
- [123] Gericke, M., Schluffer, K., Liebert, T., Heinze, T. and Budtova, T. Rheological properties of cellulose/ionic liquid solutions: from dilute to concentrated states. *Biomacromolecules*. 2009, **10**(5), pp.1188-1194.
- [124] Nazari, B., Utomo, N.W. and Colby, R.H. The Effect of Water on Rheology of Native Cellulose/Ionic Liquids Solutions. *Biomacromolecules*. 2017, **18**(9), pp.2849-2857.
- [125] Hawkins, J.E., Liang, Y., Ries, M.E. and Hine, P.J. Time temperature superposition of the dissolution of cellulose fibres by the ionic liquid 1-ethyl-3-methylimidazolium acetate with cosolvent dimethyl sulfoxide. *Carbohydrate Polymer Technologies and Applications*. 2021, **2**, p.100021.
- [126] Liang, Y., Ries, M.E. and Hine, P.J. Three methods to measure the dissolution activation energy of cellulosic fibres using time-temperature superposition. *Carbohydrate Polymers*. 2022, **291**, p.119541.

- [127] Cuissinat, C. and Navard, P. Swelling and Dissolution of Cellulose Part 1: Free Floating Cotton and Wood Fibres in N - Methylmorpholine - N - oxide - Water Mixtures. *Macromolecular Symposia*. 2006, **244**(1), pp.1-18.
- [128] Cuissinat, C. and Navard, P. Swelling and dissolution of cellulose, Part III: plant fibres in aqueous systems. *Cellulose*. 2008, **15**(1), pp.67-74.
- [129] Cuissinat, C., Navard, P. and Heinze, T. Swelling and dissolution of cellulose, Part V: Cellulose derivatives fibres in aqueous systems and ionic liquids. *Cellulose*. 2008, **15**(1), pp.75-80.
- [130] Cuissinat, C. and Navard, P. Swelling and dissolution of cellulose part II: Free floating cotton and wood fibres in NaOH–water–additives systems. *Macromolecular Symposia*. 2006, **244**(1), pp.19-30.
- [131] Cuissinat, C., Navard, P. and Heinze, T. Swelling and dissolution of cellulose. Part IV: Free floating cotton and wood fibres in ionic liquids. *Carbohydrate Polymers*. 2008, **72**(4), pp.590-596.
- [132] Rattanasom, N., Saowapark, T. and Deeprasertkul, C. Reinforcement of natural rubber with silica/carbon black hybrid filler. *Polymer Testing*. 2007, **26**(3), pp.369-377.
- [133] Pullawan, T., Wilkinson, A.N., Zhang, L.N. and Eichhorn, S.J. Deformation micromechanics of all-cellulose nanocomposites: Comparing matrix and reinforcing components. *Carbohydrate Polymers*. 2014, **100**, pp.31-39.
- [134] Kumar, T.S.M., Rajini, N., Reddy, K.O., Rajulu, A.V., Siengchin, S. and Ayrilmis, N. All-cellulose composite films with cellulose matrix and Napier grass cellulose fibril fillers. *International journal of biological macromolecules*. 2018, **112**, pp.1310-1315.
- [135] Duchemin, B.J.C., Mathew, A.P. and Oksman, K. All-cellulose composites by partial dissolution in the ionic liquid 1-butyl-3-methylimidazolium chloride. *Composites Part A: Applied Science and Manufacturing*. 2009, **40**(12), pp.2031-2037.
- [136] Shakeri, A., Mathew, A.P. and Oksman, K. Self-reinforced nanocomposite by partial dissolution of cellulose microfibrils in ionic liquid. *Journal of Composite Materials*. 2012, **46**(11), pp.1305-1311.
- [137] Ma, H., Zhou, B., Li, H.-S., Li, Y.-Q. and Ou, S.-Y. Green composite films composed of nanocrystalline cellulose and a cellulose matrix regenerated from functionalized ionic liquid solution. *Carbohydrate Polymers*. 2011, **84**(1), pp.383-389.
- [138] Henderson, D., Zhang, X., Mao, Y., Hu, L., Briber, R.M. and Wang, H. Cellulose Nanocomposites of Cellulose Nanofibers and Molecular Coils. *Journal of Composites Science*. 2021, **5**(8), p.200.

- [139] Shibata, M., Teramoto, N., Nakamura, T. and Saitoh, Y. All-cellulose and all-wood composites by partial dissolution of cotton fabric and wood in ionic liquid. *Carbohydrate Polymers*. 2013, **98**(2), pp.1532-1539.
- [140] Gindl-Altmutter, W., Keckes, J., Plackner, J., Liebner, F., Englund, K. and Laborie, M.P. All-cellulose composites prepared from flax and lyocell fibres compared to epoxy-matrix composites. *Composites Science and Technology*. 2012, **72**(11), pp.1304-1309.
- [141] Adak, B. and Mukhopadhyay, S. Jute based all-cellulose composite laminates. *Indian Journal of Fibre & Textile Research*. 2016, **41**(4), pp.380-384.
- [142] Shibata, M., Yamazoe, K., Kuribayashi, M. and Okuyama, Y. All-wood biocomposites by partial dissolution of wood flour in 1-butyl-3-methylimidazolium chloride. *Journal of Applied Polymer Science*. 2013, **127**(6), pp.4802-4808.
- [143] Ou, R.X., Xie, Y.J., Shen, X.P., Yuan, F.P., Wang, H.G. and Wang, Q.W. Solid biopolymer electrolytes based on all-cellulose composites prepared by partially dissolving cellulosic fibers in the ionic liquid 1-butyl-3-methylimidazolium chloride. *Journal of Materials Science*. 2012, **47**(16), pp.5978-5986.
- [144] Haverhals, L.M., Sulpizio, H.M., Fayos, Z.A., Trulove, M.A., Reichert, W.M., Foley, M.P., De Long, H.C. and Trulove, P.C. Process variables that control natural fiber welding: time, temperature, and amount of ionic liquid. *Cellulose*. 2012, **19**(1), pp.13-22.
- [145] Charlet, K., Eve, S., Jernot, J., Gomina, M. and Breard, J. Tensile deformation of a flax fiber. *Procedia Engineering*. 2009, **1**(1), pp.233-236.
- [146] Huber, T., Pang, S.S. and Staiger, M.P. All-cellulose composite laminates. *Composites Part A: Applied Science and Manufacturing*. 2012, **43**(10), pp.1738-1745.
- [147] Chen, F., Sawada, D., Hummel, M., Sixta, H. and Budtova, T. Unidirectional All-Cellulose Composites from Flax via Controlled Impregnation with Ionic Liquid. *Polymers*. 2020, **12**(5), p.1010.
- [148] Chen, K., Xu, W., Ding, Y., Xue, P., Sheng, P., Qiao, H., Wang, S. and Yu, Y. Mechanical and thermal properties of all-wood biocomposites through controllable dissolution of cellulose with ionic liquid. *Polymers*. 2020, **12**(2), p.361.
- [149] Khakalo, A., Tanaka, A., Korpela, A., Hauru, L.K.J. and Orelma, H. All-Wood Composite Material by Partial Fiber Surface Dissolution with an Ionic Liquid. *ACS Sustainable Chemistry & Engineering*. 2019, **7**(3), pp.3195-3202.
- [150] Spörl, J.M., Batti, F., Vocht, M.P., Raab, R., Müller, A., Hermanutz, F. and Buchmeiser, M.R. Ionic Liquid Approach Toward Manufacture and

Full Recycling of All-Cellulose Composites. *Macromolecular Materials and Engineering*. 2018, **303**(1).

- [151] Adak, B. and Mukhopadhyay, S. All-cellulose composite laminates with low moisture and water sensitivity. *Polymer*. 2018, **141**, pp.79-85.
- [152] Salleh, M.M., Magniez, K., Pang, S., Dormanns, J.W. and Staiger, M.P. Parametric optimization of the processing of all-cellulose composite laminae. *Advanced Manufacturing-Polymer & Composites Science*. 2017, **3**(2), pp.73-79.
- [153] Adak, B. and Mukhopadhyay, S. A comparative study on lyocell-fabric based all-cellulose composite laminates produced by different processes. *Cellulose*. 2017, **24**(2), pp.835-849.
- [154] Zhao, Q., Yam, R.C.M., Zhang, B., Yang, Y., Cheng, X. and Li, R.K.Y. Novel all-cellulose eco-composites prepared in ionic liquids. *Cellulose*. 2009, **16**(2), pp.217-226.
- [155] Yousefi, H., Nishino, T., Faezipour, M., Ebrahimi, G. and Shakeri, A. Direct Fabrication of All-Cellulose Nanocomposite from Cellulose Microfibers Using Ionic Liquid-Based Nanowelding. *Biomacromolecules*. 2011, **12**(11), pp.4080-4085.
- [156] Kröling, H., Duchemin, B., Dormanns, J., Schabel, S. and Staiger, M.P. Mechanical anisotropy of paper-based all-cellulose composites. *Composites Part A: Applied Science and Manufacturing*. 2018, **113**, pp.150-157.
- [157] Huber, T., Bickerton, S., Mussig, J., Pang, S.S. and Staiger, M.P. Solvent infusion processing of all-cellulose composite materials. *Carbohydrate Polymers*. 2012, **90**(1), pp.730-733.
- [158] Adak, B. and Mukhopadhyay, S. Effect of pressure on structure and properties of lyocell fabric-based all-cellulose composite laminates. *Journal of the Textile Institute*. 2017, **108**(6), pp.1010-1017.
- [159] Chen, K., Xu, W.X., Ding, Y., Xue, P., Sheng, P.H., Qiao, H. and He, J.M. Hemp-based all-cellulose composites through ionic liquid promoted controllable dissolution and structural control. *Carbohydrate Polymers*. 2020, **235**.
- [160] Baghaei, B., Compieg, S. and Skrifvars, M. Mechanical properties of all-cellulose composites from end-of-life textiles. *Journal of Polymer Research*. 2020, **27**(9), pp.1-9.
- [161] Chen, F., Bouvard, J.L., Sawada, D., Pradille, C., Hummel, M., Sixta, H. and Budtova, T. Exploring digital image correlation technique for the analysis of the tensile properties of all-cellulose composites. *Cellulose*. 2021, **28**(7), pp.4165-4178.

- [162] Li, J.Y., Nawaz, H., Wu, J., Zhang, J.M., Wan, J.Q., Mi, Q.Y., Yu, J. and Zhang, J. All-cellulose composites based on the self-reinforced effect. *Composites Communications*. 2018, **9**, pp.42-53.
- [163] Victoria, A., Ries, M.E. and Hine, P.J. Use of interleaved films to enhance the properties of all-cellulose composites. *Composites Part A: Applied Science and Manufacturing*. 2022, p.107062.
- [164] Liu, H., Cheng, G., Kent, M., Stavila, V., Simmons, B.A., Sale, K.L. and Singh, S. Simulations reveal conformational changes of methylhydroxyl groups during dissolution of cellulose I β in ionic liquid 1-ethyl-3-methylimidazolium acetate. *The Journal of Physical Chemistry B*. 2012, **116**(28), pp.8131-8138.
- [165] De, C., Giannini, Lassandro, Scattarella, Sibillano, Matricciani and Fanti. X-Ray Dating of Ancient Linen Fabrics. *Heritage*. 2019, **2**(4), pp.2763-2783.
- [166] Amutha, K. Environmental impacts of denim. In: Muthu, S.S. ed. *Sustainability in Denim*. First edition ed. United Kingdom: Woodhead Publishing, 2017, pp.27-48.
- [167] Kidwai, N.H., Singh, H. and Chatterjee, A. ALL-CELLULOSE COMPOSITE FROM COTTON FABRIC AND CELLULOSE SOLUTION. *Cellulose Chemistry and Technology*. 2020, **54**(7-8), pp.757-764.
- [168] De Silva, R., Wang, X.A. and Byrne, N. Recycling textiles: the use of ionic liquids in the separation of cotton polyester blends. *RSC Advances*. 2014, **4**(55), pp.29094-29098.
- [169] Liu, Z., Wang, H., Li, Z., Lu, X., Zhang, X., Zhang, S. and Zhou, K. Characterization of the regenerated cellulose films in ionic liquids and rheological properties of the solutions. *Materials Chemistry and Physics*. 2011, **128**(1-2), pp.220-227.
- [170] Kosan, B., Michels, C. and Meister, F. Dissolution and forming of cellulose with ionic liquids. *Cellulose*. 2008, **15**(1), pp.59-66.
- [171] Bazbouz, M.B., Taylor, M., Baker, D., Ries, M.E. and Goswami, P. Dry-jet wet electrospinning of native cellulose microfibers with macroporous structures from ionic liquids. *Journal of Applied Polymer Science*. 2019, **136**(10), p.15.
- [172] Sun, N., Rahman, M., Qin, Y., Maxim, M.L., Rodriguez, H. and Rogers, R.D. Complete dissolution and partial delignification of wood in the ionic liquid 1-ethyl-3-methylimidazolium acetate. *Green Chemistry*. 2009, **11**(5), pp.646-655.
- [173] Liu, H., Sale, K.L., Holmes, B.M., Simmons, B.A. and Singh, S. Understanding the Interactions of Cellulose with Ionic Liquids: A Molecular Dynamics Study. *The Journal of Physical Chemistry B*. 2010, **114**(12), pp.4293-4301.

- [174] Zhang, J., Zhang, H., Wu, J., Zhang, J., He, J. and Xiang, J. NMR spectroscopic studies of cellobiose solvation in EmimAc aimed to understand the dissolution mechanism of cellulose in ionic liquids. *Physical Chemistry Chemical Physics*. 2010, **12**(8), pp.1941-1947.
- [175] Sescousse, R., Gavillon, R. and Budtova, T. Aerocellulose from cellulose–ionic liquid solutions: Preparation, properties and comparison with cellulose–NaOH and cellulose–NMMO routes. *Carbohydrate Polymers*. 2011, **83**(4), pp.1766-1774.
- [176] Li, W., Sun, N., Stoner, B., Jiang, X., Lu, X. and Rogers, R.D. Rapid dissolution of lignocellulosic biomass in ionic liquids using temperatures above the glass transition of lignin. *Green Chemistry*. 2011, **13**(8), pp.2038-2047.
- [177] Heinze, T., Dorn, S., Schöbitz, M., Liebert, T., Köhler, S. and Meister, F. Interactions of ionic liquids with polysaccharides–2: Cellulose. *Macromolecular Symposia*. 2008, **262**(1), pp.8-22.
- [178] Köhler, S., Liebert, T., Schöbitz, M., Schaller, J., Meister, F., Günther, W. and Heinze, T. Interactions of Ionic Liquids with Polysaccharides 1. Unexpected Acetylation of Cellulose with 1 - Ethyl - 3 - methylimidazolium Acetate. *Macromolecular Rapid Communications*. 2007, **28**(24), pp.2311-2317.
- [179] Le, K.A., Rudaz, C. and Budtova, T. Phase diagram, solubility limit and hydrodynamic properties of cellulose in binary solvents with ionic liquid. *Carbohydrate Polymers*. 2014, **105**, pp.237-243.
- [180] Druel, L., Niemeyer, P., Milow, B. and Budtova, T. Rheology of cellulose-[DBNH][CO 2 Et] solutions and shaping into aerogel beads. *Green Chemistry*. 2018, **20**(17), pp.3993-4002.
- [181] Gong, J., Li, J., Xu, J., Xiang, Z. and Mo, L. Research on cellulose nanocrystals produced from cellulose sources with various polymorphs. *RSC Advances*. 2017, **7**(53), pp.33486-33493.
- [182] Kafle, K., Greeson, K., Lee, C. and Kim, S.H. Cellulose polymorphs and physical properties of cotton fabrics processed with commercial textile mills for mercerization and liquid ammonia treatments. *Textile Research Journal*. 2014, **84**(16), pp.1692-1699.
- [183] Heines, S.V. John Mercer and mercerization, 1844. *Journal of Chemical Education*. 1944, **21**(9), p.430.
- [184] Ramos, L.A., Morgado, D.L., Gessner, F., Frollini, E. and El Seoud, O.A. A physical organic chemistry approach to dissolution of cellulose: effects of cellulose mercerization on its properties and on the kinetics of its decrystallization. *Arkivoc*. 2011, pp.416-425.
- [185] Rippon, J.A. and Evans, D.J. Improving the properties of natural fibres by chemical treatments. In: Kozłowski, R.M. ed. *Handbook of Natural*

Fibres. First edition ed. Cambridge: Woodhead Publishing, 2012, pp.63-140.

- [186] Jähn, A., Schröder, M.W., Fütting, M., Schenzel, K. and Diepenbrock, W. Characterization of alkali treated flax fibres by means of FT Raman spectroscopy and environmental scanning electron microscopy. *Spectrochimica Acta Part A: Molecular and Biomolecular Spectroscopy*. 2002, **58**(10), pp.2271-2279.
- [187] Yue, Y.Y., Han, G.P. and Wu, Q.L. Transitional Properties of Cotton Fibers from Cellulose I to Cellulose II Structure. *Bioresources*. 2013, **8**(4), pp.6460-6471.
- [188] Yue, Y., Zhou, C., French, A.D., Xia, G., Han, G., Wang, Q. and Wu, Q. Comparative properties of cellulose nano-crystals from native and mercerized cotton fibers. *Cellulose*. 2012, **19**(4), pp.1173-1187.
- [189] Holme, I. Coloration of technical textiles. In: Horrocks, A.R. and Anand, S.C. eds. *Handbook of Technical Textiles (SECOND EDITION)*. Second edition ed. Cambridge: Woodhead Publishing, 2016, p.257.
- [190] Yu, J.W., Choi, Y.-M., Kim, S.M., Lee, J.-K., You, N.-H. and Goh, M. Synthesis of twisted ribbon-like carbon, carbon microtubes and carbon rod from mercerized cotton fiber. *Synthetic Metals*. 2015, **206**, pp.115-119.
- [191] Saito, H., Sakurai, A., Sakakibara, M. and Saga, H. Preparation and properties of transparent cellulose hydrogels. *Journal of Applied Polymer Science*. 2003, **90**(11), pp.3020-3025.
- [192] Chang, C., Duan, B., Cai, J. and Zhang, L. Superabsorbent hydrogels based on cellulose for smart swelling and controllable delivery. *European Polymer Journal*. 2010, **46**(1), pp.92-100.
- [193] Bartos, A., Anggono, J., Farkas, Á.E., Kun, D., Soetaredjo, F.E., Móczó, J., Antoni, Purwaningsih, H. and Pukánszky, B. Alkali treatment of lignocellulosic fibers extracted from sugarcane bagasse: Composition, structure, properties. *Polymer Testing*. 2020, **88**, p.106549.
- [194] Stamm, A.J. Thermal Degradation of Wood and Cellulose. *Industrial & Engineering Chemistry*. 1956, **48**(3), pp.413-417.
- [195] Şerbănescu, C. Kinetic analysis of cellulose pyrolysis: a short review. *Chemical Papers*. 2014, **68**(7), pp.847-860.
- [196] Broido, A. A simple, sensitive graphical method of treating thermogravimetric analysis data. *Journal of Polymer Science Part A-2: Polymer Physics*. 1969, **7**(10), pp.1761-1773.
- [197] Wang, S.R., Dai, G.X., Yang, H.P. and Luo, Z.Y. Lignocellulosic biomass pyrolysis mechanism: A state-of-the-art review. *Progress in Energy and Combustion Science*. 2017, **62**, pp.33-86.

- [198] Ward, S.M. and Braslaw, J. Experimental weight loss kinetics of wood pyrolysis under vacuum. *Combustion and Flame*. 1985, **61**, pp.261-269.
- [199] Conesa, J.A., Caballero, J., Marcilla, A. and Font, R. Analysis of different kinetic models in the dynamic pyrolysis of cellulose. *Thermochimica Acta*. 1995, **254**, pp.175-192.
- [200] Banyasz, J.L., Li, S., Lyons-Hart, J.L. and Shafer, K.H. Cellulose pyrolysis: the kinetics of hydroxyacetaldehyde evolution. *Journal of Analytical and Applied Pyrolysis*. 2001, **57**(2), pp.223-248.
- [201] Garcia-Perez, M. and Metcalf, J. *The formation of polyaromatic hydrocarbons and dioxins during pyrolysis : a review of the literature with descriptions of biomass composition, fast pyrolysis technologies and thermochemical reactions*. Pullman, Washington: Washington State University., 2008.
- [202] Zhu, G., Zhu, X., Xiao, Z. and Yi, F. Study of cellulose pyrolysis using an in situ visualization technique and thermogravimetric analyzer. *Journal of Analytical and Applied Pyrolysis*. 2012, **94**, pp.126-130.
- [203] Friedman, H.L. Kinetics of thermal degradation of char-forming plastics from thermogravimetry. Application to a phenolic plastic. *Journal of Polymer Science Part C: Polymer Symposia*. 1964, **6**(1), pp.183-195.
- [204] Fan, Y., Cai, Y., Li, X., Jiao, L., Xia, J. and Deng, X. Effects of the cellulose, xylan and lignin constituents on biomass pyrolysis characteristics and bio-oil composition using the Simplex Lattice Mixture Design method. *Energy Conversion and Management*. 2017, **138**, pp.106-118.
- [205] Özsın, G. Assessing thermal behaviours of cellulose and poly (methyl methacrylate) during co-pyrolysis based on an unified thermoanalytical study. *Bioresource technology*. 2020, **300**, p.122700.
- [206] Mamleev, V., Bourbigot, S. and Yvon, J. Kinetic analysis of the thermal decomposition of cellulose: the main step of mass loss. *Journal of Analytical and Applied Pyrolysis*. 2007, **80**(1), pp.151-165.
- [207] Luo, L., Guo, X., Zhang, Z., Chai, M., Rahman, M.M., Zhang, X. and Cai, J. Insight into pyrolysis kinetics of lignocellulosic biomass: isoconversional kinetic analysis by the modified friedman method. *Energy & Fuels*. 2020, **34**(4), pp.4874-4881.
- [208] Cao, W., Li, J., Martí-Rosselló, T. and Zhang, X. Experimental study on the ignition characteristics of cellulose, hemicellulose, lignin and their mixtures. *Journal of the Energy Institute*. 2019, **92**(5), pp.1303-1312.
- [209] Yeo, J.Y., Chin, B.L.F., Tan, J.K. and Loh, Y.S. Comparative studies on the pyrolysis of cellulose, hemicellulose, and lignin based on combined kinetics. *Journal of the Energy Institute*. 2019, **92**(1), pp.27-37.

- [210] Morgado, D.L. and Frollini, E. Thermal decomposition of mercerized linter cellulose and its acetates obtained from a homogeneous reaction. *Polímeros*. 2011, **21**(2), pp.111-117.
- [211] Zhu, L. and Zhong, Z. Effects of cellulose, hemicellulose and lignin on biomass pyrolysis kinetics. *Korean Journal of Chemical Engineering*. 2020, **37**(10), pp.1660-1668.
- [212] Thanatawee, P., Rukthong, W., Sunphorka, S., Piumsomboon, P. and Chalermssinsuwan, B. Effect of biomass compositions on combustion kinetic parameters using response surface methodology. *International Journal of Chemical Reactor Engineering*. 2016, **14**(1), pp.517-526.
- [213] Moriana, R., Zhang, Y., Mischnick, P., Li, J. and Ek, M. Thermal degradation behavior and kinetic analysis of spruce glucomannan and its methylated derivatives. *Carbohydrate Polymers*. 2014, **106**, pp.60-70.
- [214] Ding, Y., Huang, B., Li, K., Du, W., Lu, K. and Zhang, Y. Thermal interaction analysis of isolated hemicellulose and cellulose by kinetic parameters during biomass pyrolysis. *Energy*. 2020, **195**, p.117010.
- [215] Dussan, K., Dooley, S. and Monaghan, R.F. A model of the chemical composition and pyrolysis kinetics of lignin. *Proceedings of the Combustion Institute*. 2019, **37**(3), pp.2697-2704.
- [216] Yang, H., Yan, R., Chen, H., Lee, D.H. and Zheng, C. Characteristics of hemicellulose, cellulose and lignin pyrolysis. *Fuel*. 2007, **86**(12), pp.1781-1788.
- [217] Lv, D., Xu, M., Liu, X., Zhan, Z., Li, Z. and Yao, H. Effect of cellulose, lignin, alkali and alkaline earth metallic species on biomass pyrolysis and gasification. *Fuel Processing Technology*. 2010, **91**(8), pp.903-909.
- [218] Poletto, M., Zattera, A.J., Forte, M.M.C. and Santana, R.M.C. Thermal decomposition of wood: Influence of wood components and cellulose crystallite size. *Bioresource Technology*. 2012, **109**, pp.148-153.
- [219] Kim, U.-J., Eom, S.H. and Wada, M. Thermal decomposition of native cellulose: Influence on crystallite size. *Polymer Degradation and Stability*. 2010, **95**(5), pp.778-781.
- [220] Ramiah, M. Thermogravimetric and differential thermal analysis of cellulose, hemicellulose, and lignin. *Journal of Applied Polymer Science*. 1970, **14**(5), pp.1323-1337.
- [221] Vanderfleet, O.M., Reid, M.S., Bras, J., Heux, L., Godoy-Vargas, J., Panga, M.K.R. and Cranston, E.D. Insight into thermal stability of cellulose nanocrystals from new hydrolysis methods with acid blends. *Cellulose*. 2019, **26**(1), pp.507-528.

- [222] Qi, H., Chang, C. and Zhang, L. Effects of temperature and molecular weight on dissolution of cellulose in NaOH/urea aqueous solution. *Cellulose*. 2008, **15**(6), pp.779-787.
- [223] Andersson, M., Wittgren, B. and Wahlund, K.-G. Accuracy in Multiangle Light Scattering Measurements for Molar Mass and Radius Estimations. Model Calculations and Experiments. *Analytical Chemistry*. 2003, **75**(16), pp.4279-4291.
- [224] Yokoyama, W., Renner-Nantz, J.J. and Shoemaker, C.F. Starch Molecular Mass and Size by Size-Exclusion Chromatography in DMSO-LiBr Coupled with Multiple Angle Laser Light Scattering. *Cereal Chemistry*. 1998, **75**(4), pp.530-535.
- [225] Iiyama, K. and Wallis, A.F.A. An improved acetyl bromide procedure for determining lignin in woods and wood pulps. *Wood Science and Technology*. 1988, **22**(3), pp.271-280.
- [226] Hatfield, R.D., Grabber, J., Ralph, J. and Brei, K. Using the acetyl bromide assay to determine lignin concentrations in herbaceous plants: some cautionary notes. *Journal of Agricultural and Food Chemistry*. 1999, **47**(2), pp.628-632.
- [227] Sundheq, A., Sundberg, K., Lillandt, C. and Holmhom, B. Determination of hemicelluloses and pectins in wood and pulp fibres by acid methanolysis and gas chromatography. *Nordic Pulp & Paper Research Journal*. 1996, **11**(4), pp.216-219.
- [228] Parviainen, H., Parviainen, A., Virtanen, T., Kilpeläinen, I., Ahvenainen, P., Serimaa, R., Grönqvist, S., Maloney, T. and Maunu, S.L. Dissolution enthalpies of cellulose in ionic liquids. *Carbohydrate Polymers*. 2014, **113**, pp.67-76.
- [229] Ghasemi, M., Tsianou, M. and Alexandridis, P. Assessment of solvents for cellulose dissolution. *Bioresource Technology*. 2017, **228**, pp.330-338.
- [230] Cortés, A.M. and Bridgwater, A.V. Kinetic study of the pyrolysis of miscanthus and its acid hydrolysis residue by thermogravimetric analysis. *Fuel Processing Technology*. 2015, **138**, pp.184-193.
- [231] Waters, C.L., Janupala, R.R., Mallinson, R.G. and Lobban, L.L. Staged thermal fractionation for segregation of lignin and cellulose pyrolysis products: An experimental study of residence time and temperature effects. *Journal of Analytical and Applied Pyrolysis*. 2017, **126**, pp.380-389.
- [232] Singh, P., Duarte, H., Alves, L., Antunes, F., Le Moigne, N., Dormanns, J., Duchemin, B., Staiger, M.P. and Medronho, B. From cellulose dissolution and regeneration to added value applications—synergism between molecular understanding and material development. In: *Cellulose-Fundamental Aspects and Current Trends*. InTech, 2015.

- [233] Nishino, T. and Arimoto, N. All-cellulose composite prepared by selective dissolving of fiber surface. *Biomacromolecules*. 2007, **8**(9), pp.2712-2716.
- [234] Soykeabkaew, N., Sian, C., Gea, S., Nishino, T. and Peijs, T. All-cellulose nanocomposites by surface selective dissolution of bacterial cellulose. *Cellulose*. 2009, **16**(3), pp.435-444.
- [235] Hine, P.J. and Ries, M.E. *Composite materials*. GB1811808.3. 2020.
- [236] Haward, S.J., Sharma, V., Butts, C.P., McKinley, G.H. and Rahatekar, S.S. Shear and Extensional Rheology of Cellulose/Ionic Liquid Solutions. *Biomacromolecules*. 2012, **13**(5), pp.1688-1699.